LBL-24382 c.2

# Lawrence Berkeley Laboratory
UNIVERSITY OF CALIFORNIA

## Materials & Chemical Sciences Division

RECEIVED
LAWRENCE
BERKELEY LABORATORY

FEB 1 1988

LIBRARY AND
DOCUMENTS SECTION

# The Reaction of Silicon with Atomic Hydrogen by Modulated Molecular Beam Mass Spectrometry

J. Abrefah
(Ph.D. Thesis)

November 1987

TWO-WEEK LOAN COPY
This is a Library Circulating Copy which may be borrowed for two weeks.

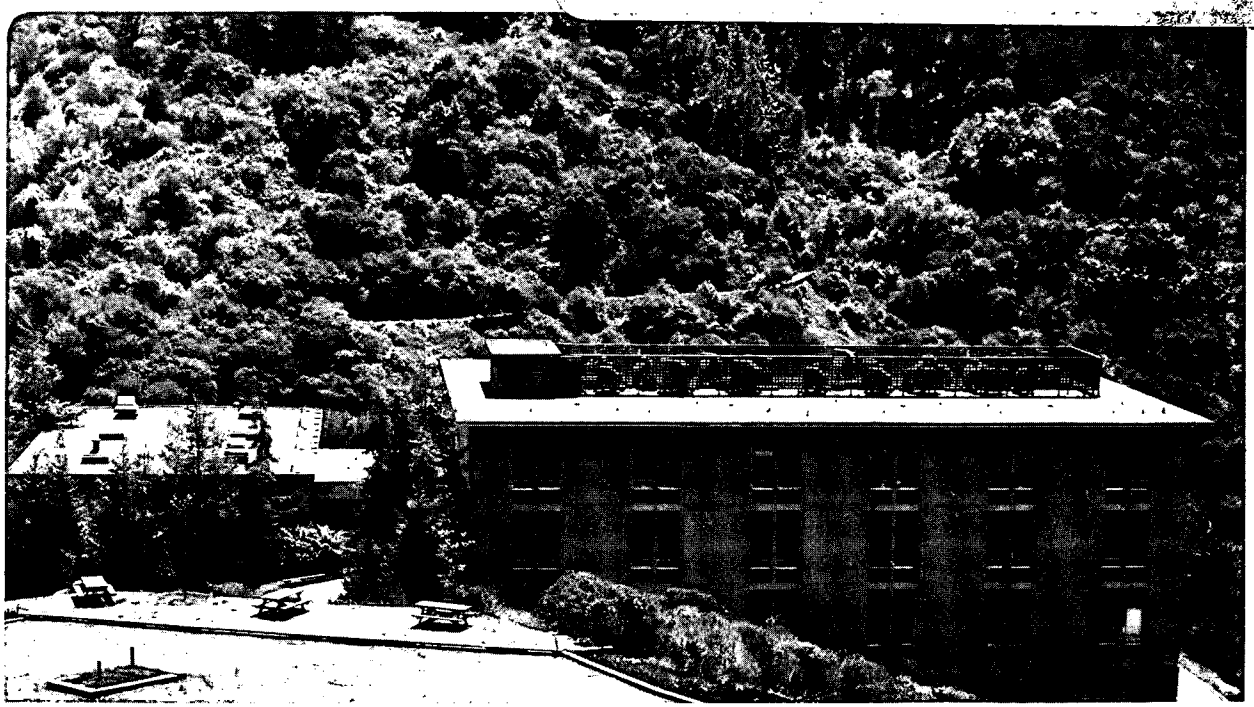

LBL-24382 c.2

Prepared for the U.S. Department of Energy under Contract DE-AC03-76SF00098

## DISCLAIMER

This document was prepared as an account of work sponsored by the United States Government. While this document is believed to contain correct information, neither the United States Government nor any agency thereof, nor the Regents of the University of California, nor any of their employees, makes any warranty, express or implied, or assumes any legal responsibility for the accuracy, completeness, or usefulness of any information, apparatus, product, or process disclosed, or represents that its use would not infringe privately owned rights. Reference herein to any specific commercial product, process, or service by its trade name, trademark, manufacturer, or otherwise, does not necessarily constitute or imply its endorsement, recommendation, or favoring by the United States Government or any agency thereof, or the Regents of the University of California. The views and opinions of authors expressed herein do not necessarily state or reflect those of the United States Government or any agency thereof or the Regents of the University of California.

# THE REACTION OF SILICON WITH ATOMIC HYDROGEN BY MODULATED MOLECULAR BEAM MASS SPECTROMETRY

John Abrefah

(Ph.D. Thesis)

Materials and Chemical Sciences Division, Lawrence Berkeley Laboratory
and Department of Nuclear Engineering, College of Engineering;
University of California, Berkeley, California 94720.

This work was supported by the Director, Office of Energy Research, Office of Basic Energy Sciences, Materials Sciences Division of the U.S. Department of Energy under contract No DE-AC03-76SF00098.

# THE REACTION OF SILICON WITH ATOMIC HYDROGEN BY MODULATED MOLECULAR BEAM MASS SPECTROMETRY

## Table of Contents


I. Abstract. ..... v

1. Introduction ..... 1

1.1. Statement of the Problem ..... 1

1.2. Silicon ..... 3

1.3. Silane ..... 5

1.4. Other Studies of the Silicon-Hydrogen System ..... 6

2. Modulated Molecular Beam Technique. ..... 11

2.1. General Features and History ..... 11

2.2. Advantages and Limitations ..... 14

2.3. Application and Analysis ..... 16

3. Description of Apparatus. ..... 18

3.1. General Characteristics ..... 18

3.2. Vacuum System ..... 18

3.2.1. The Source Chamber ..... 18

3.2.2. The Target Chamber ..... 20

3.2.3. The Detection Chamber ..... 21

3.3. Gas Inlet System ..... 22

3.3.1. Gas Handling System ..... 22

3.3.2. The Reactant Beam Source ..... 22

3.4. Beam Properties ..... 24

3.5. The Modulation System ..... 30

3.6. Temperature Measurements ..... 32

3.7. The Detection System ..... 35

4. Experimental Results. ..... 37

4.1. Target Surface Characteristics ..... 37

4.2. Reaction Product Measurements ..... 39

4.2.1 Silane Production ..... 39

4.2.2. Molecular Hydrogen Reaction Product ..... 45

4.3. Ion Enhancement ..... 48

4.4. Molecular Hydrogen Effect ..... 49

4.5. Hydrogen Solubility in Silicon ..... 50

5. Reaction Mechanism ..... 68

5.1. General Features ..... 68

5.1.1. Responses of $\varepsilon$ and $\Phi$ to Temperature Changes ..... 68

5.1.2. Small Phase Lags ..... 68

5.1.3. Reaction Order ..... 72

5.2. Reaction Model ..... 72

5.2.1 Saturation of Dangling Bonds ..... 72

5.2.2. Bulk Solution-Diffusion ..... 74

5.2.3. Surface Recombination ..... 75

5.2.4. Silane Production ..... 75

5.2.5. Model ..... 78

5.2.6. Analysis of the Reaction Model ..... 79

6. Discussion ..... 90

6.1. Saturation of Strongly-Bound Hydrogen ..... 90

6.2. Rate Constants ..... 93

6.3. Structural Sensitivity ..... 96

6.4. Etching Rate ..... 97

7. Conclusion ..... 98

Acknowledgements ..... 99

Appendix I ..... 100

Appendix II ..... 106

References ..... 114

# THE REACTION OF SILICON WITH ATOMIC HYDROGEN BY MODULATED MOLECULAR BEAM MASS SPECTROMETRY

John Abrefah

Materials and Chemical Sciences Division, Lawrence Berkeley Laboratory
and Department of Nuclear Engineering, College of Engineering;
University of California, Berkeley, California.

## Abstract

The kinetics and mechanism of the gas-solid reaction of single crystal silicon, Si(111), and atomic hydrogen were studied by the modulated molecular beam mass spectrometric method. The experiment was carried out in an ultra-high vacuum chamber with an atomic hydrogen beam produced by thermally dissociating molecular hydrogen in a tungsten oven at 2500 K. Silicon was not etched by molecular hydrogen but interacted very strongly with atomic hydrogen to produce the volatile silicon tetrahydride, $SiH_4$, and molecular hydrogen by recombination of surface-adsorbed H atoms. The silicon surface was characterized by in situ Auger electron spectroscopy (AES). The target surface temperature, beam intensity, and chopping frequency were the experimental variables. The temperature was varied from 300 K – 1000 K in most of the tests. However, some of the data were taken at temperatures above 1000 K. The equivalent beam intensity at the target ranged between $10^{15}$ – $10^{17}$ atoms $cm^{-2}$ $sec^{-1}$, and the frequency was varied from 20 Hz to 900 Hz. The apparent reaction probabilities and the phase lags of the $SiH_4$ and $H_2$ products were measured as functions of these experimental variables. Approximately 50% of the incident H atoms recombined on the surface and were re-emitted as molecular hydrogen. The $SiH_4$ reaction probability was highest at room temperature (≈ 3%), and decreased with increasing temperature up to about 1000 K. At 1100 K, where Si(111) changes surface structure from Si(111)-7x7 to Si(111)-1x1, the production of $SiH_4$ was a minimum, and increased with further increase in

temperature. No reaction was observed with an oxidized silicon surface, and oxygen surface concentrations above 1% had a significant effect on reducing the strength of the reaction. The proposed reaction model is based on the molecular beam data in conjunction with thermal desorption spectroscopy (TDS) and electron energy loss spectroscopy (EELS) results obtained by other workers. The mechanism involves saturation of the surface dangling bonds by atomic hydrogen, formation of SiH and $SiH_2$ surface complexes, and reaction with a weakly-bound overlayer of hydrogen. The weakly bound hydrogen is mobile. It diffuses into the bulk and reacts with the $SiH_2$ complex to form $SiH_4$. Rate constants characterizing the elementary steps of the mechanism were determined by fitting the model to the data.

# 1. INTRODUCTION

## 1.1. Statement of the Problem

In the design of the Control Thermonuclear Reactor (CTR) a low-Z material such as SiC is considered as a desirable compound to be used as a protective barrier for the first wall, limiters and divertors[1-2]. The impetus to use low-Z materials rather than other well-characterized engineering materials is due to the following benefits:

- Reduction of the effective atomic weight of plasma species and the corresponding increase in the core temperature; this reduces energy loss through bremsstrahlung in the plasma[3].
- Neutron interactions with such materials produce small amounts of long- and short-half life radionuclides. This reduces the amount of radioactive waste and the concommitant disposal problems, and provides easy access for maintenance purposes.
- The enhancement of strength at high temperatures for most of the ceramics becomes an additional plus in this application.

However, these surfaces will be exposed to energetic hydrogen neutrals and ions, electrons and 14 MeV neutrons. Sputtering and chemical etching of these materials needs to be understood for a comprehensive design analysis of the lifetime of the wall and its effect with the plasma. A complete understanding of such a complex interaction between the plasma and the wall has to be studied in steps that provide the necessary details. The analysis of this plasma-wall interaction is most important for the overall hydrogen inventory, which is necessary for a break-even plasma condition.

Sputtering of carbon substrates by hydrogen atoms[4-8] and by energetic hydro-

gen ions[9-13] has been extensively studied at various experimental conditions. To increase the understanding of the compound SiC interaction with the plasma, similar studies have to be done on elemental Si.

In the semiconductor industry, where silicon is the preferred substrate, plasma etching and ion-enhanced reactions of single-crystal semiconductors by reactive gases have recently become an increasingly important processing technique. Mostly the halogens and their compounds have been used as the reactive gases, but others are considering hydrogen as an alternative reactant[14]. Veprek and co-workers have utilized the equilibrium reaction

$$Si(s) + xH = SiH_x(g) \tag{1.1}$$

for preparing thin films of microcrystalline silicon by chemical transport in a low-pressure plasma[15]. Rational design of such processes requires quantitative models of the kinetics of the surface reactions by which substrate atoms are removed as volatile species. Because of the complexity of plasma etching, single-effect experiments, in which only the chemistry of the surface reactions are investigated, can provide very useful information. An important feature of such experiments is the capability of separating the effects of the gaseous reactant on one hand and to laser or ion beams on the other. Studies of the thermal reaction which lead to an understanding of the basic mechanisms of the surface chemistry then permit subsequent investigation of the ion- or laser-beam-enhanced reaction to be better understood.

The saturation of surface and bulk dangling bonds of silicon by atomic hydrogen has been exploited in a number of useful applications (discussed in section 4.5). At the same time, the following issues remain unresolved:

a) Stability of the hydrogen-silicon alloy upon long exposure to the processing environment.

b) The mechanisms for the introduction of hydrogen into silicon lattice during

processing.

c) The amount of hydrogen present in processed and as-received silicon wafers.

d) Effect of substitutional impurities and defect structure of silicon on hydrogen solubility and low-temperature diffusion coefficient of hydrogen in silicon.

e) The lattice sites of molecular and atomic hydrogen in pure and defective silicon.

For these reasons, theoreticians and experimenters have sought to understand the Si-H system since the early 1970's. The relevant studies of this system to this work is the subject of the discussions in section 1.4.

## 1.2. Silicon

Silicon was first isolated in a more or less pure state by Gay-Lussac and Thenard in 1811, who reduced $SiF_4$ with metallic potassium. Its properties were first described by Berzeluis in 1823. Silicon naturally exists in three stable isotopic forms; Si-28 (92.9%), Si-28 (4.7%) and Si-30 (3.1%).

Silicon is a tetravalent nonmetallic element which belongs to group IV in the periodic table. It is not freely available in nature but in its combined form, $SiO_2$, it is the most abundant element (next to oxygen) in the earth's crust; spectral analysis of the outer regions of the sun shows silicon to be the sixth most abundant element, following hydrogen, helium, oxygen, carbon and nitrogen; chemical analysis of meteorites reveal silicon to be the third in abundance, after oxygen and iron; and estimates of its cosmic abundance rank it seventh, following hydrogen, helium, oxygen, neon, nitrogen and carbon. Clearly, silicon is an important element in the earth-moon system, the solar system as well as in the cosmos.

The most common minerals of silicon are the silicates (quartz, tridymite, cristobalite, the hydrous silica mineral opal, vitreous silica, melanophlogite, coesite, keatite and stishovite) which are all compounds of silicon and oxygen. Silicon is

produced as a brittle, hard, lustrous gray crystal with a diamond structure (lattice parameter = 5.43A and Si-Si bond energy of 47 kcal/mol), as a glistening black graphite form, or as a dark brown powder produced by reduction of silica with carbon. The pure monocrystalline silicon that has found increasingly important technical application in the semiconductor industry is produced from $SiHCl_3$ by reduction with $H_2$, or through thermal decomposition of $SiH_4$.

Silicon is the most common semiconductor material used today in the industry, due to its energy band gap of 1.1 eV, which makes it superior to germanium (0.7 eV band-gap) for high temperature applications. Other commercial uses of silicon are as alloys (as ferrosilicon), in combination with ceramic materials, in cements and in the form of silicones (organosilicon oxide polymers).

A freshly-cleaved Si (111) plane in a vacuum has a metastable Si(111)-2x1 reconstructed surface structure. This structure transforms to a stable, reconstructed Si(111)-7x7 structure when heated to 973K. The structure of the latter has been the subject of several publications[75-90] and a number of structural models have been discussed. A summary of these models are the following:

i) Vacancy model suggested by Lander et al.[75]; the model consists of 13 vacancies in the 7x7 unit cell, one at each corner of the unit cell and 2x6 arranged locally in the 2x2 structure in the two triangular subcells of the 7x7 unit cell.

ii) A 13 adatom model instead of vacancies was proposed by Harrison[76].

iii) A rippled surface model that explain LEED patterns which shows intensity distribution with three-fold symmetry was suggested by Lavine et al.[77]; another rippled structure of ring-like arrangement of raised or lowered atoms in each triangular subcell was suggested by Miller et al, Monch and Chadi[78-80].

iv) "12 adatom model" based on surface relief image of STM showing a deep dip at the corner and 12 hills inside the unit cell was discussed by Binning et al.[81].

v) Cardillo[87] suggested a trough model from his helium atom diffraction results which indicated an absence of the top double layer over a large fraction of the unit mesh.

vi) Bennet et al.[82] suggested a model containing stacking faults (wurtzite stacking) using the constant momentum transfer averaged (CTMA), LEED results and RBS data of [0 0 1] incidence.

vii) A milk-stool model was proposed by Snyder et al.[85,86]; in the model 12 pyramidal clusters are located on top of the "filled" sites of the unreconstructed Si(111) layer to have a wurtzite stacking.

viii) DAS model suggested by Takayanagi et al.[90] is a three dimensional structural model which consists of 9 atom pairs (dimers) on the sides of the triangular subcells, 12 adatoms locally arranged in the 2x2 structure and a layer with different stacking in the two subcells; this model was based on transmission electron diffraction (TED) patterns and it has 19 dangling bonds per unit cell.

All the models which were based on LEED and RHEED results were inconclusive due to the large unit cell that had to be analyzed and the complication effect of dynamical scattering of the electron beam. The model suggested by Takayanagi et al., which incorporates the TED technique with the other results, seems to be the conclusive structure of Si(111)-7x7.

### 1.3. Silane

Silane, $SiH_4$, which is the main product of the atomic hydrogen reaction with Si was first prepared in 1857 by Wöhler using an aluminum-silicon alloy and hydrochloric acid. However, the properties of $SiH_4$ and the other saturated silicon hydrides up to $Si_4H_{10}$ were not investigated thoroughly until 1916 by Stock[16] who proposed the name "silane" for them. Silane has also been prepared by the action of

hydrochloric acid on magnesium silicide, but it is produced by the Finholt[17,18] process:

$$SiCl_4 + LiAlH_4 = SiH_4 + LiCl + AlCl_3 \tag{1.2}$$

$SiH_4$ has a boiling point of 161 K and a freezing point of of 88 K. The Si-H bond energy is 75 kcal/mole and the heat of formation, $\Delta H_f^0(SiH_4)$ at 293 K is 7.3 kcal/mole[19–21]. Thus it is expected that Si will be etched by atomic hydrogen if the rate of reaction is large enough. Silane reacts very strongly with oxygen.

### 1.4. Other Studies of Silicon-Hydrogen System

Studies using different surface techniques are the subject of several papers, but only those that attempt to measure the mechanism and kinetics of the reaction of hydrogen with silicon are discussed here.

Chang et al.[14] used a hydrogen plasma to study the etching rate of silicon and its oxide. The experiment was carried out in quartz or pyrex discharge tubes and the etch rates were determined by measuring the thickness of the substrate material consumed in the unmasked regions by SEM and scanning ellipsometry. The former technique was also used to study the surface morphology of the etched substrate. For an rf power of 400W and a pressure of 0.2 torr etching rates of $SiO_2$ and Si of $1.5 \times 10^{-3}$ $\mu$m/min. and 0.025 - 0.05 $\mu$m/min, respectively were determined. A polysilicon specimen, however, showed an etch rate of 0.07 $\mu$m/min. The etched surface exhibited a rough morphology after 15 min. of etching.

Webb and Veprek[22] studied the reactivity of a hydrogen plasma with silicon in a temperature range of 283 K to 813 K, at discharge currents up to 420 mA and a pressure of 0.1 torr. The etching rate was measured by continuously monitoring the weight loss of the silicon sample using a microbalance. The rate of the reaction

$$Si(s) + xH \longrightarrow SiH_x(g) \tag{1.3}$$

was found to increase with increasing discharge current, and at a constant discharge current and varying temperature, it displays a maximum around 323 K – 353 K, decreasing with increasing temperature. Etching rates up to 0.09 $\mu$m/min. were reported under conditions of high hydrogen flow rates. They suggested the following two competing reactions to explain the decrease in etch rate with increasing temperature:

the production of $SiH_x$ gaseous products;

$$Si(s) + H(g) \longrightarrow Si\text{–}H$$

$$Si\text{–}H + H(g) \longrightarrow SiH_2 \ldots \longrightarrow SiH_4 \tag{1.4}$$

and the heterogeneous recombination to produce $H_2$;

$$SiH_x + H(g) \longrightarrow SiH_{x-1} + H_2(g) \tag{1.5}$$

They stated that the increasing rate of the recombination reaction (Eq. 1.5) with increasing temperature causes a diminished concentration of chemisorbed hydrogen on the surface and consequently reduces the etch rate.

Veprek and Sarrott[23], using the same equipment discussed in the previous paragraph, studied the electron-induced chemical reaction of silicon with a hydrogen plasma. Single-crystal Si chips in the (111) orientation and high purity hydrogen at a flow rate of $\approx 30 - 300$ mbar cm$^3$/sec. were used. The samples were etched for a period of several hours and the etching rate was calculated from the weight decrease. They reported the following results:

-- A fairly linear increase of the etching rate with the electron current density that indicates constant cross section for the electron-impact-induced process.

-- An Arrhenius dependence with a negative activation energy of about - 4.2 kcal/mole and a pre-exponential factor of about $1.6 \times 10^{-5}$.

-- A linear dependence of the etch rate on total pressure.

-- The morphology of the etched surface shows a rough pattern with fairly well developed singular crystallographic planes, which is indicative of mobility of the adsorbed species.

-- The pronounced anisotropy of the electron-impact-induced etching provides strong evidence that the initial step is the electron-impact-induced dissociation of the surface-adsorbed molecular hydrogen. The non-zero etch rate for zero electron flux, indicates that gas phase atomic hydrogen reaction with Si contributes to the total etching rate.

The fact that atomic hydrogen reacts with silicon at room temperature forming silane signifies a low-activation energy for the process

$$Si(s) + H(g) \longrightarrow SiH(ads) \longrightarrow \ldots \longrightarrow SiH_4(g) \qquad (1.6)$$

Veprek and Sarrott suggested the following simplified reaction mechanism to explain their results:

$$\tfrac{1}{2}H_2(g) = \tfrac{1}{2}H_2(ads) = H(ads) \longrightarrow \ldots \longrightarrow SiH_x(g) \qquad x=3,4 \qquad (1.7)$$

Using a surface mass balance equation for H(ads) and assuming that the recombination rate is much faster than the successive addition of H atoms to form silane, the etching rate is given by;

$$r = k_r[H(ads)]^m = k_r\left\{k_2\left[H_2(g)\right]\frac{k_1}{k'_1k'_2}\right\}^{m/n} \qquad (1.8)$$

where $k_r$ is the rate constant for silane production; $k_2 = \sigma_{el}i_{el}$ is the dissociative adsorption rate constant; $k_1$ the rate constant of molecular hydrogen adsorption; and $k'_1$ and $k'_2$ are the corresponding reverse reactions of the latter two processes. The pressure dependence gives m/n = 1, which reduces the above equation to:

$$r = Ae^{\left(-\frac{E}{RT}\right)} \qquad (1.9)$$

where

$$E = -4.2\,\text{kcal./mole} = E_1 + E_r - E'_1 - E'_2$$

From the estimates of $E_1$, $E'_1$ and $E'_2$, they arrived at a value of about $10-11$ kcal/mole for $E_r$.

Even though previous authors attempted to developed a reaction mechanism for the Si-H system, the results were not conclusive due to the limited information derived from their experimental technique and the complex effect of the electrons on the surface reaction. The modulated molecular beam method, which offers detailed mechanistic and kinetic information on the surface reaction, is utilized in this work to elucidate the complex chemical reaction of atomic hydrogen with crystalline silicon. Furthermore in the process of deriving the mechanism, concepts obtained from other surface techniques such as TDS, EELS and IRS, are used.

The ability of atomic hydrogen to bond to and passivate electrically-active deep level centers such as transition-metal impurities or lattice defects in Si has been observed[55–58]. This is a direct proof of atomic hydrogen dissolution in Si. Such interaction of H atoms with Si has led to a number of possible applications in the semiconductor industry, namely:

i) Hydrogenation of surface dangling bonds is known to reduce the surface leakage current in p-n junctions[59]; thus deposition of amorphous hydrogenated silicon, a-Si(H), onto the junction is found to lower the surface leakage contribution more than $SiO_2$ passivation over the same junction[60]; the surfaces of large-volume Si and Ge diodes used as nuclear radiation detectors are routinely coated with a-Si(H).

ii) Process-induced defects are neutralized by exposure of the finished devices to a low-pressure hydrogen plasma at low moderate temperatures (< 670 K); this improves carrier mobility.

iii) Performance of photovoltaic devices fabricated from bulk polycrystalline sili-

con and electrical characteristics of polycrystalline thin films used for resistors and interconnects in integrated circuits are limited by grain boundaries which act as recombination centers[97]; annealing in atomic hydrogen has been shown to improve the electrical characteristics in bulk and thin-film polycrystalline silicon[61–62].

A literature survey shows that the only related data on the solubility of hydrogen in silicon is the work done by A. van Wieringen et al.[63]. In section 4.5, an experimental technique that measures hydrogen (deuterium) solubility as well as determination of possible lattice sites of hydrogen in the bulk of crystalline silicon is discussed.

# 2. MODULATED MOLECULAR BEAM TECHNIQUE

## 2.1. General Features & History

The modulated molecular beam technique was first demonstrated by Foner and Hudson[24] in 1953, and was first applied by Smith and Fite[25,26] in 1962 to study gas-solid reactions. The broad utility of the technique has been a subject of several review papers[27–34], and dozens of heterogeneous gas-solid reactions have been studied using this technique. Modulation of the beam has the important advantages of:

1) Providing a measure of the reaction residence time on the target surface, and

2) Improving the signal-to-noise ratio of the detection system.

The reaction residence time is derived from the phase lag measurement between the first Fourier component of an output signal from the reaction product and that from the reflected reactant which did not undergo surface reaction. Such a direct measurement of surface residence time provides a particularly sensitive test of proposed reaction mechanisms.

The general features of a typical modulated molecular beam system for a gas-solid reaction are shown in fig. 2.1. The technique uses a mass spectrometer detection system, a collisionless molecular beam, and is carried out in an ultra-high vacuum environment. Reactant gas effusing from a source tube is modulated by a rotating slotted disc, and travels through a collimating orifice to the target (i.e. solilid reactant) surface.

The reflected reactant and the desorbed products issuing from the surface are collimated into the detection chamber, which houses a quadrupole mass spectrometer. A fraction of the species is ionized and filtered through the mass analyzer onto an electron multiplier. The signal from the multiplier combined with a reference signal derived from the chopper motor is analyzed by a phase-lock detector.

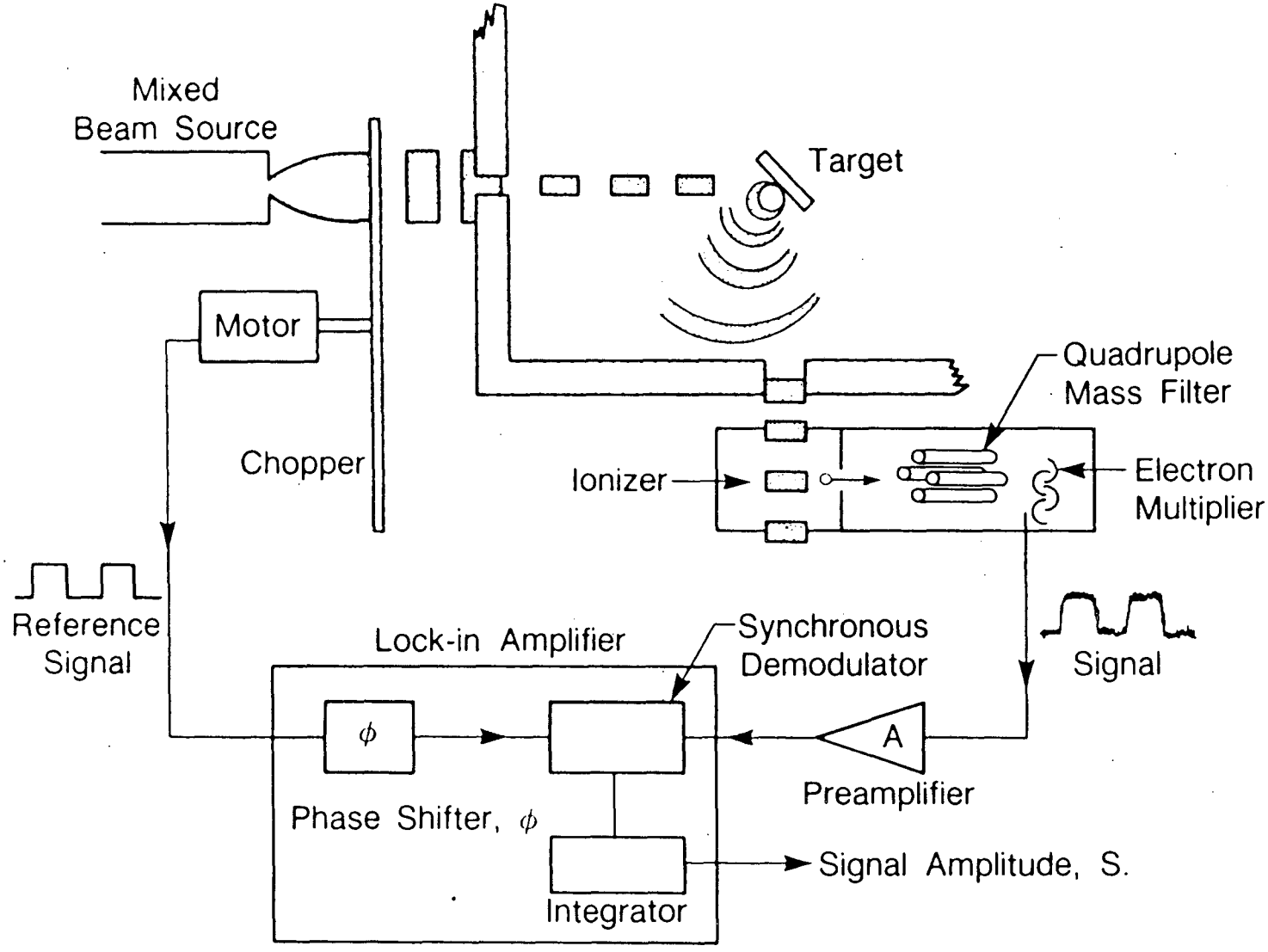


Fig. 2.1. Schematic of modulated beam experimental apparatus.

XBL 877-10245

Different phase-sensitive detection systems are available but only the lock-in amplifier used in this study is discussed.

A lock-in amplifier passes the input signal through a narrow band amplifier and then rectifies the signal in a synchronous demodulator which operates at the same frequency as the input signal. A sine-wave generator produces a sinusoidal signal with the same frequency and phase as the reference signal. The phase of the sine-wave is adjusted by a variable phase shifter and multiplied by the amplified detector signal in the synchronous demodulator. An integrator averages the output of the demodulator to give the fundamental Fourier coefficient, S, of the input waveform with respect to $\sin(\omega t + \Phi)$. The measured phase lag, $\Phi$, relative to the reference signal is adjusted to maximize the amplitude, S , of the input signal.

Alternatively, the sine wave and the amplified detector signal are fed into a two-phase accessory which analyzes these input signals to give two signals, one in-phase, $S_0$, and the other quadrature, $S_{90}$. The two component signals are recorded by a dual-chart recorder. These are later used to calculate the amplitude and phase lag using the following equations:

$$S = \sqrt{S_0^2 + S_{90}^2} \tag{2.1}$$

$$\Phi = \tan^{-1}(S_{90} / S_0) \tag{2.2}$$

In addition to the synchronous modulation/lock-in amplifier detection, the entire waveforms of the reflected reactant and desorbed products can be obtained by pulse-counting techniques combined with data accumulation in a multi-channel analyzer. The pulse-counting method can achieve any level of signal-to-noise ratio in the output signal by using sufficiently long counting times. Complete waveforms of the output signals of both the reactant and the product provide additional information for analysis of very complicated surface mechanisms.

## 2.2. Advantages and Limitations

The most important features and drawbacks of the modulated molecular beam method for studying surface chemical kinetics are discussed below. The positive points of the technique include;

i) The high-vacuum environment in which the experiments are conducted provides a well-cleaned and -characterized surface; different crystallographic orientations can be studied.

ii) A low-background gas pressure in the apparatus makes gas phase reactions unlikely; only pure heterogeneous gas-surface processes take place.

iii) Reactions with walls of the apparatus or in sampling lines are avoided by the direct-flight mass-spectrometric detection method; molecules which make several collisions with walls are out of phase and not detected by the AC detection method.

iv) Reverse reactions are absent because the reaction products are pumped away before they can return to the reacting surface.

v) Mass spectrometric detection makes product identification unambiguous (except for difficulties in interpreting mass spectra).

vi) In addition to providing kinetic information on the surface processes, modulation of the beam coupled with phase-sensitive detection improves the signal-to-noise ratio of the detection system by at least a factor of 1000 relative to DC detection; it also permits velocities of the species emitted from the surface to be measured.

vii) The phase lag and the reaction probability obtained from the experimental data provide the information needed for detailed, quantitative modeling.

viii) The collimated nature of the incident reactant beam provides a means of exploiting isotope exchange as a technique for unraveling surface processes.

On the other hand, the molecular beam method has a number of disadvantages when compared to conventional techniques for investigating surface reactions. These includes:

i) The sensitivity is low because only the consequences of single molecular collisions with the surface are detectable; in practice, reactions which occur with probability less than $\approx 10^{-4}$ per collision cannot be measured.

ii) The reaction product must be volatile for it to be detected by the mass spectrometer; this eliminates certain reactions like the corrosion of metals with non-volatile products from investigation by the technique.

iii) Very fast reactions (reaction times less than $\approx 10\mu s$) are detectable but all kinetic information on the reactions is lost; this limitation arises from the effects of time-spreading during transit of the molecular beams between the surface and the detector.

iv) The low pressure (i.e., incident fluxes equivalent to gas pressures $P_{eq} \leq 10^{-4}$ torr) at which the reactions are conducted makes it difficult to relate the results of molecular beam experiments to those obtained for the same reaction conducted at atmospheric pressure by conventional methods.

v) The angular distributions of the scattered reactant molecules or the emitted reaction products are usually not measured; moreover, with a fixed angle of detection (usually specular), interpretation of the data relies on the assumption of a cosine distribution of all molecules leaving the surface.

vi) Modeling of the reactions is complex and uniqueness of the models deduced from molecular beam data is not assured.

Despite these shortcomings, the modulated molecular beam method can provide kinetic and mechanistic information on surface chemical reactions unattainable by other techniques. And reaction modeling based on such data is greatly enhanced if

complementary techniques, such as temperature-ramp thermal desorption spectroscopy, surface spectroscopy or gravimetric rate experiments, can be brought to bear on the same reaction.

## 2.3. Application and Analysis

In a molecular beam experiment the data consist of apparent reaction probabilities and phase lags as functions of incident reactant beam intensity, $I_0$, substrate surface temperature, T, and modulation frequency, f. The apparent reaction probability is the ratio of the amplitudes of the output signals from the reaction product and that from the portion of the reactant which simply reflected from the surface. For low reaction probabilities ($\leq 10^{-2}$), the reflected reactant signal is an accurate measure of the incident flux. In the case of a linear reaction the above definition is applicable for high reaction probabilities if the scattered reactant signal is corrected for consumption to give product. For a complex surface reaction, various mass balance equations have to be solved to extract the apparent reaction probability.

The name "apparent" is used because it differs from the "true" reaction probability, which is the fraction of the incident reactant beam that reacted with the substrate to give a product. Because of demodulation, this measure of apparent reaction probability is always less than the true value, and the two are only equal in the limit of zero frequency. The phase lag is that of the product signal relative to the scattered reactant. The measured phase lags are corrected for all parasitic effects (see pg. 91-93 of Ref. 35).

Based on these experimental results, a model of the surface reaction is deduced. Such reaction models are combinations of elementary steps such as the sticking of the gaseous reactants, surface reaction of the Langmuir-Hinshelwood or Eley-Rideal types, product desorption, and surface and/or bulk diffusion of reaction intermediates. Surface mass balance equations for these elementary steps, which

usually contain several unknown parameters, are solved to give the reaction product vector equation. A general form of the reaction product vector equation is,

$$\varepsilon e^{-i\Phi} = F(f, T, I_0, \eta, k_1, k_2, \ldots) \tag{2.3}$$

where $\eta$ is the sticking probability, $k_1$, $k_2$ are rate constants of the elementary steps which make up the process, and f, $I_0$, and T are the experimental defined variables. The reaction product vector equation is solved for $\varepsilon$ and $\Phi$ using rate constants which best fit the corresponding experimental values by the least squares approximation or other curve-fitting techniques. In practice several of these theoretical models are tested to arrive at the one which best fits the experimental data with least number of rate constants.

# 3. DESCRIPTION OF APPARATUS

## 3.1. General Characteristics

The details of the apparatus (Fig.3.1) are discussed in Ref. 36. The main features that enable gas-solid systems with low reaction probabilities to be studied by this equipment are the following:

-- The differential pumping provides ultra-high vacuum (UHV) environment that minimizes the beam/background ratio, avoids substrate surface contamination and reduces noise in the mass spectrometer.

-- A compact arrangement of the beam source-to-target surface-to-detector geometry reduces the inverse square beam-spreading losses and therefore improves the signal-to-noise ratio.

Even though there is provision to rotate the target for different angles of beam incidence, the target is positioned at $45^0$ to the beam direction for in situ mass spectrometer detection.

## 3.2. Vacuum System

The vacuum system consists of three individually pumped chambers which are connected by orifices through which the incident molecular beam and the species leaving the surface move in collisionless flow. The chambers are: (1) the source chamber, (2) the target chamber, and (3) the detection chamber.

### 3.2.1. The Source Chamber

This chamber is fabricated from a 17.8-cm diameter aluminum cross. At the ends of each arm is an 20.3-cm flange. The bottom flange is connected to 5000 l/s oil diffusion pump with a water baffle. A Welch 1397 mechanical pump with dry trap is connected to the diffusion pump as a roughing pump for the three chambers

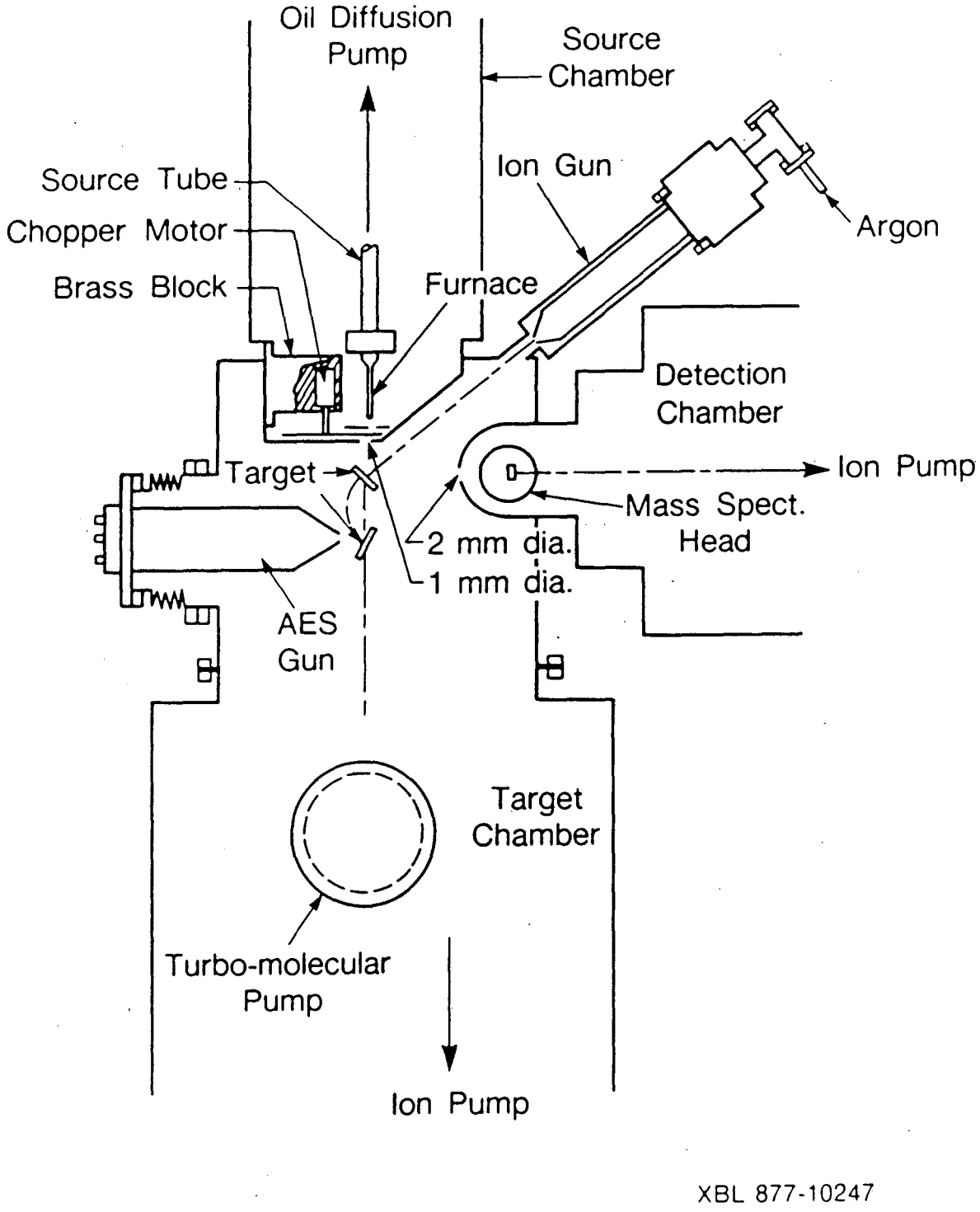


Fig. 3.1. Schematic of Apparatus (Plan View).

and as a backup pump to the diffusion pump. The top arm is covered with a plate which has a pipe connection through a viton 'O' ring valve to the target chamber. This feature is used to supplement the roughing pump of the target chamber through the diffusion pump. One end of the horizontal arm of the cross is covered with a glass plate with three feedthroughs. Two of these are water-cooled copper tubes for the ground electrical connection to the oven. The centered third tube is a 0.95-cm stainless steel tube, which supplies gas to the oven. The details of the oven assembly are discussed later. The opposite end arm of the cross is connected to the target chamber with a 1 mm orifice in the center. The orifice is aligned with another 1 mm hole on the side of the tungsten tube through which the gas effuses into the vacuum. The chamber houses the modulation system that consists of the chopper motor and 6-bladed mechanical chopper. Electrical connections for the motor and oven, and the cooling water for the motor are introduced through "O" ring compression fittings placed around the periphery of the arm containing the beam source tip. The pressure is measured by type RG-75 Bayard-Alpert gauge powered by a Veeco RG 31X ionization gauge controller. A base pressure of $2 \times 10^{-8}$ torr is obtained in this chamber with no load but increases to $5 \times 10^{-4}$ torr at an operating pressure of 6 torr inside the $H_2$ feed gas line.

### 3.2.2. The Target Chamber

The target chamber is made of 304 stainless steel and pumped by an Ultek 1200 l/s ion pump and/or a Balzers TPU 1500 turbo-molecular pump. The target chamber communicates with the source chamber through the 1 mm diameter collimating orifice. The beam effusing through this orifice is incident at $45^0$ on the silicon, Si(111), surface. The Si(111) target is held in place by a Huntington model #PM-600 XYZ TRC target holder with a Varian block assembly. The holder enters the chamber vertically through a 15-cm flange. Alignment of the solid surface in

the incident beam direction is achieved by the six-fold motion of the holder. The target-holder flange has a small port (1.9-cm) through which a secondary gas beam is leaked to the target surface for isotopic exchange experiments. A port at the same elevation as the target serves two purposes. A PHI model 10-155 Cylindrical Analyzer is connected through this port for Auger electron spectroscopy analysis of the target surface. This provides the surface characterization of the Si(111). Alternatively a second mass spectrometer connected at this port can be positioned directly in the incident beam flight path for monitoring the primary beam composition when the target is retracted. A small view port with a sapphire window permits viewing of the Si(111) surface for temperature measurement by an optical or infrared pyrometer. The same port serves as connection for an ion gun. Another view port at the rear end of the ion pump is located on the beam axis and is used for alignment and temperature measurement when the previously-mentioned port is blocked by the ion gun. At the rear end of the ion pump are two Ultek sorption pumps connected through a viton "O" ring sealed valve for clean roughing of the chamber. All flanges in this chamber are sealed with copper gaskets and the ion pump has internal heaters for bake-out. A base pressure of $4 \times 10^{-9}$ torr is attained in this chamber after bake out and increases to $5 \times 10^{-8}$ torr under normal beam load. The pressure is measured by an ionization gauge.

### 3.2.3. The Detection Chamber

The detection chamber houses a quadrupole mass spectrometer for measuring the species in the gas arriving from the solid surface. The mass spectrometer is connected through an adjustable stainless steel bellows to a 15-cm flange at the bottom of a stainless steel pipe chamber. The ionizer of the mass spectrometer is positioned perpendicular to the primary beam so that scattered molecules pass directly through it. The part of beam not ionized travels through a 15-cm long stainless steel bellows into a 270 l/s Varian ion pump. Roughing of this chamber is through a

connecting 2 mm diameter collimating orifice to the target chamber. At the rear end of this chamber is a view port in line with the scattered beam direction for alignment purposes. An external heat shroud around the ion pump and heating tapes wound around the appendages are used for bake-out. Operating pressure measured by an ionization gauge is $2 \times 10^{-10}$ torr at full molecular beam load.

### 3.3. Gas Inlet System

The gas inlet system is made up of a gas handling system (Fig.3.2), and the source oven located inside the source chamber.

#### 3.3.1. Gas Handling System

Molecular deuterium of high purity (research grade) is taken from a gas cylinder and a brass regulator through 0.64-cm stainless steel tubing into a Matheson Hydrogen filter. The filter is a palladium membrane tube which is heated to 500 K during operation and it produces hydrogen of 99.9999% purity. The flow of gas is controlled by a Granville Phillips variable leak valve. The gas pressure is measured either by a thermocouple gauge (below 0.1 torr) or by a Wallace & Tiernan (Serial # FA 160-LL04152) gauge (0.1 - 20 torr) after the leak valve. The gas then travels through 0.64-cm stainless steel tube to a 0.95-cm stainless steel tube which passes through a glass window into the source chamber. In the chamber the stainless steel tube is joined to a copper tube of the same size by a Swagelok union. The copper tube is brazed to a copper block. A 5.6 mm copper tube brazed to the 0.64-cm and the copper block is the supply line of gas to the tungsten oven. The 1 mm diameter orifice at the mid-plane of the tungsten tube is the evacuation channel for the gas system by the roughing pump.

#### 3.3.2. The Reactant Beam Source

A mixed molecular and atomic hydrogen beam is generated in a tungsten

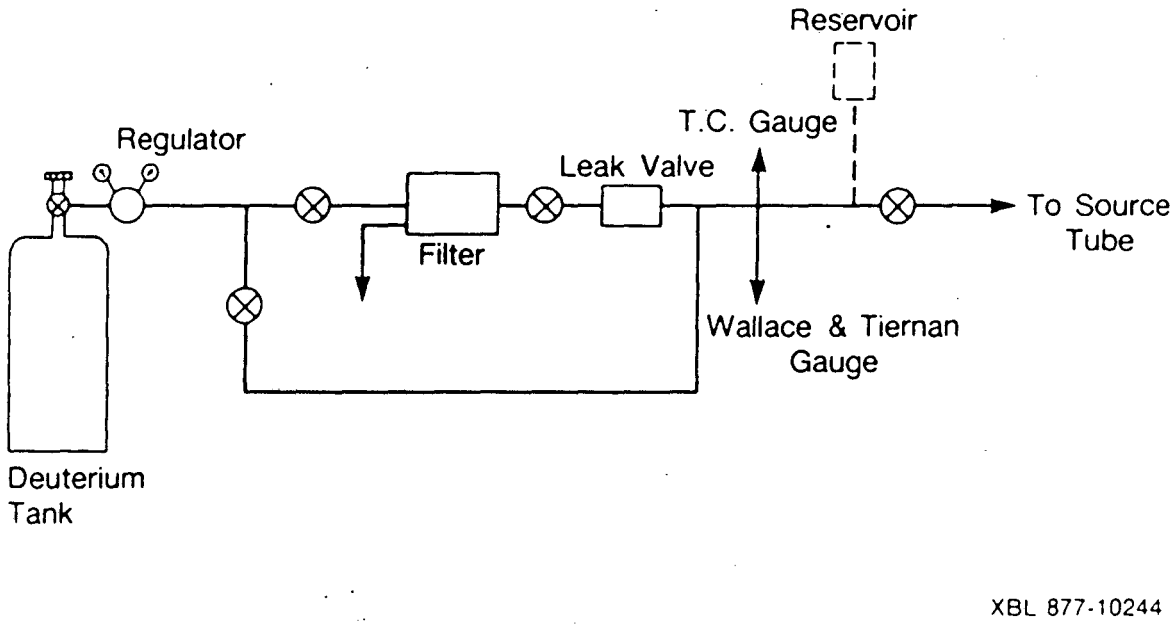


Fig. 3.2. Schematic of gas handling system; The reservoir is connected only during the leak rate experiment.

furnace. The oven is a tungsten tube, closed at one end, and fabricated by chemical vapor deposition. It has a length of 7 cm, an outside diameter of 0.37 cm and a wall thickness of 0.25 mm. A 1 mm diameter orifice is spark cut at the mid-point of the tube. The open end of the tube is press fit into a water-cooled copper block. The gas supply to the oven is through 5.6 mm diameter copper tube which is brazed to the copper block, as shown in fig. 3.3. The oven tube is resistively heated up to its design maximum temperature of 2500 K by passing a current of 150 A through six tungsten (0.76 mm diameter) leads which are spring-loaded to the bottom. This arrangement ensures free axial expansion of the tube thereby avoiding breakage by bending moments. The temperature of the furnace is measured by sighting an optical pyrometer on the mid-plane of the tube through the glass window in the source chamber. The partial pressure of atomic hydrogen in the oven as a function of total beam pressure (measured in the inlet gas supply) is calculated assuming thermodynamic equilibrium in the oven and transition flow in the flow lines. Knowing the atomic hydrogen partial pressure, the beam intensity of H atoms is calculated. The lower and upper limits of beam intensity are dictated by equipment constraints. The upper boundary is mainly controlled by the capacities of the pumps to maintain the required pressures in the three chambers. The lower limit, however, is a function of the strength of the surface chemical reaction. A weak surface reaction requires a certain minimum beam intensity that will produce a detectable reaction-product signal over the background noise.

### 3.4. Beam Properties

The beam pressure in the oven is derived from the measured upstream gauge pressure and the calculated pressure drop along the flow path to the oven. The details of this calculation are given in Appendix I. For a given oven pressure the type of flow through the orifice is deduced using the Liepmann criterion[37].

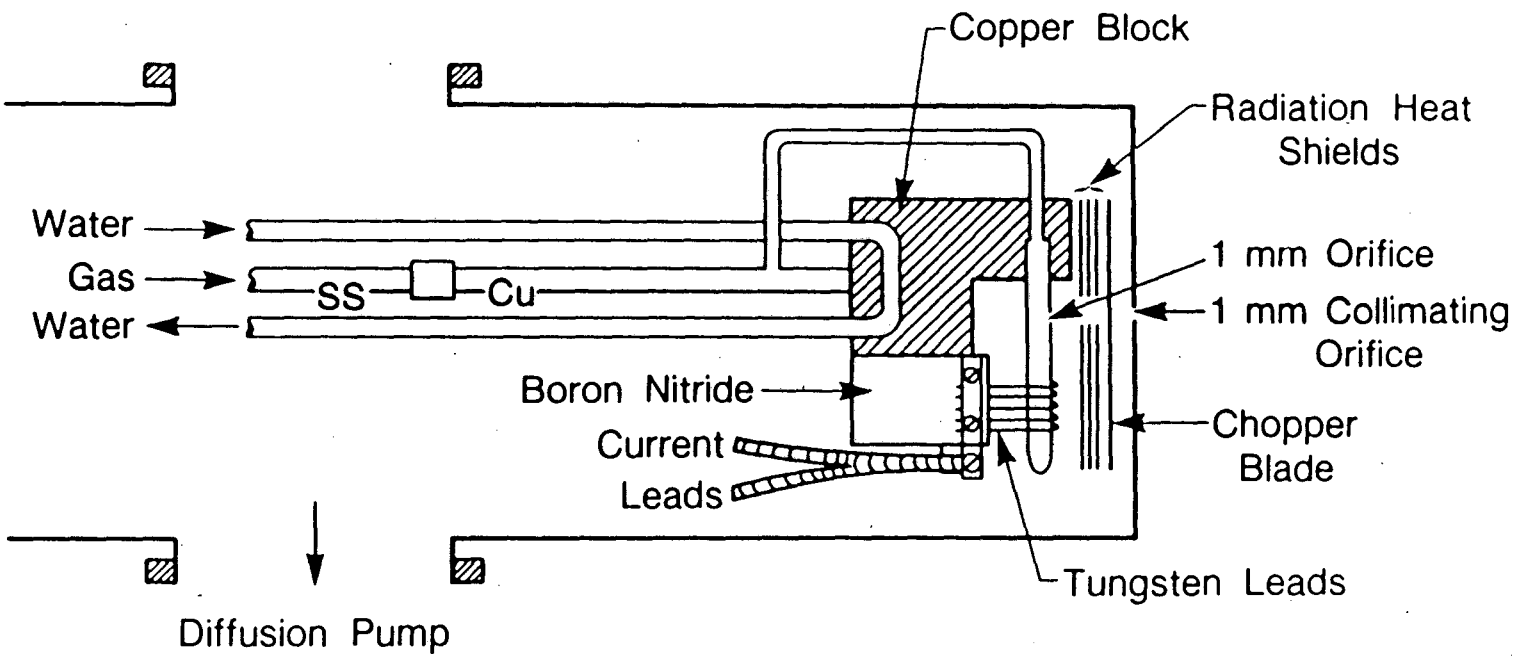


Fig. 3.3. Schematic of Oven Assembly.

In this method a modified Knudsen number, Kn is given by the relation,

$$Kn^{-1} = 2.512\frac{a_0}{\lambda_0} \tag{3.1}$$

where $a_0$ = radius of the orifice; $\lambda_0$ = average mean free path in the atomic and molecular hydrogen, mixture. The flow regimes are defined by:

$Kn < 1.6$, free molecular flow

$1.6 < Kn < 16.6$, transition flow

$Kn > 16.6$, hydrodynamic flow.

An analogous determination of the flow regime along the gas flow path dictates the mass flow rate equation used in computing the pressure drop. The oven pressures corresponding to the measured gauge pressures are then calculated. The atomic and molecular hydrogen leak rates, their intensities and fluxes at the target surface are computed. Results of the computations are shown in Appendix I.

An experimental verification of these theoretical results was performed. In order to avoid the necessity of absolute calibration of the second mass spectrometer used in this test, two experiments were performed. One was a measurement of the total leak rate of hydrogen from the pressure decrease with time in a reservoir of known volume. An empirical equation that fits the pressure decay data is,

$$P = P_0\, e^{-0.0748t} \tag{3.3}$$

where P is the reservoir pressure at time, t, and $P_0$ is the initial pressure in the reservoir. The total leak rate, $l_t$, is related to the reservoir pressure by,

$$l_t = \frac{1}{\chi}\left(-\frac{dP}{dt}\right)_{t=0} \tag{3.4}$$

where $\chi = \frac{kT}{V_T}$; $V_T$ is the total gas volume (620.2 $cm^3$), which includes the

volumes of the reservoir (206.5 $cm^3$), gauge (395.0 $cm^3$) and the tubing (18.7 $cm^3$); and **k** (the Boltzmann constant), is equal to $1.38 \, x \, 10^{-16} gm \; cm^2 \; \sec^{-2} \; K^{-1}$. At $300 \, K$, $\chi = 6.68 \, x \, 10^{-17} gm \; \sec^{-2} cm^{-1}$. These equations and data were used in calculating the leak rates in table 3.1.

| Time (sec) | Reservoir Pressure (torr) | Leak Rate x $10^{-18}$ (*molec.* $\sec^{-1}$) |
|---|---|---|
| 0.0 | 6.0 | 8.94 |
| 2.2 | 5.0 | 7.58 |
| 5.1 | 4.0 | 6.10 |
| 9.6 | 3.0 | 4.37 |
| 15.3 | 2.0 | 2.84 |
| 25.2 | 1.0 | 1.35 |
| 32.6 | 0.5 | 0.80 |
| 45.7 | 0.1 | 0.29 |

Table 3.1. The measured total hydrogen leak rate through the oven 1 *mm* orifice.

The additional experimental results needed to calculate the beam intensities and fluxes at the target are the direct beam measurement of atomic and molecular hydrogen signals. The signals are related to the species densities in the ionizer through the following equations;

$$S_1 = K_{ig} \gamma_1 t_1 \sigma_1 n_1 \tag{3.5a}$$

$$S_2 = K_{ig} \gamma_2 t_2 \sigma_2 n_2 \tag{3.5b}$$

if the cracking contribution of $H_2 \rightarrow H^+$ in the ionizer is ignored. All the symbols in Eq. 3.5a,b are defined in Appendix II. From these equation, with $t_1 = t_2$

$$\xi = \frac{S_1}{S_2} = \frac{\sigma_1 \gamma_1 n_1}{\sigma_2 \gamma_2 n_2} \tag{3.6}$$

For hydrogen; $\frac{\gamma_1}{\gamma_2} = 0.7523$[42]; and $\frac{\sigma_1}{\sigma_2} = 0.7003$.

The ideal gas equation, the above equation and the data lead to the following relation between $\xi$ and the density ratio of atomic and molecular forms of hydrogen in the oven:

$$\frac{n_1}{n_2} = 1.898\xi \tag{3.7}$$

The leak rate ratio is dependent on the type of flow through the oven orifice; For free molecular flow,

$$\frac{l_1}{l_2} = \frac{n_1 v_{a1}}{n_2 v_{a2}} = \sqrt{2}\frac{n_1}{n_2} = 2.685\xi \tag{3.8}$$

where $v$ is the mean speed of the species. For hydrodynamic flow,

$$\frac{l_1}{l_2} = \frac{n_1}{n_2} = 1.898\xi \tag{3.9}$$

The total hydrogen leak rate, $l_t = \frac{1}{2}l_1 + l_2$ from Table 3.1 and the leak rate ratio from Eq. (3.8) or (3.9) give the leak rates for each species for any source pressure. Free molecular flow,

$$l_1 = \frac{2.685 l_T \xi}{1 + 1.3425\xi} \tag{3.10}$$

$$l_2 = \frac{l_T}{1 + 1.3425\xi} \tag{3.11}$$

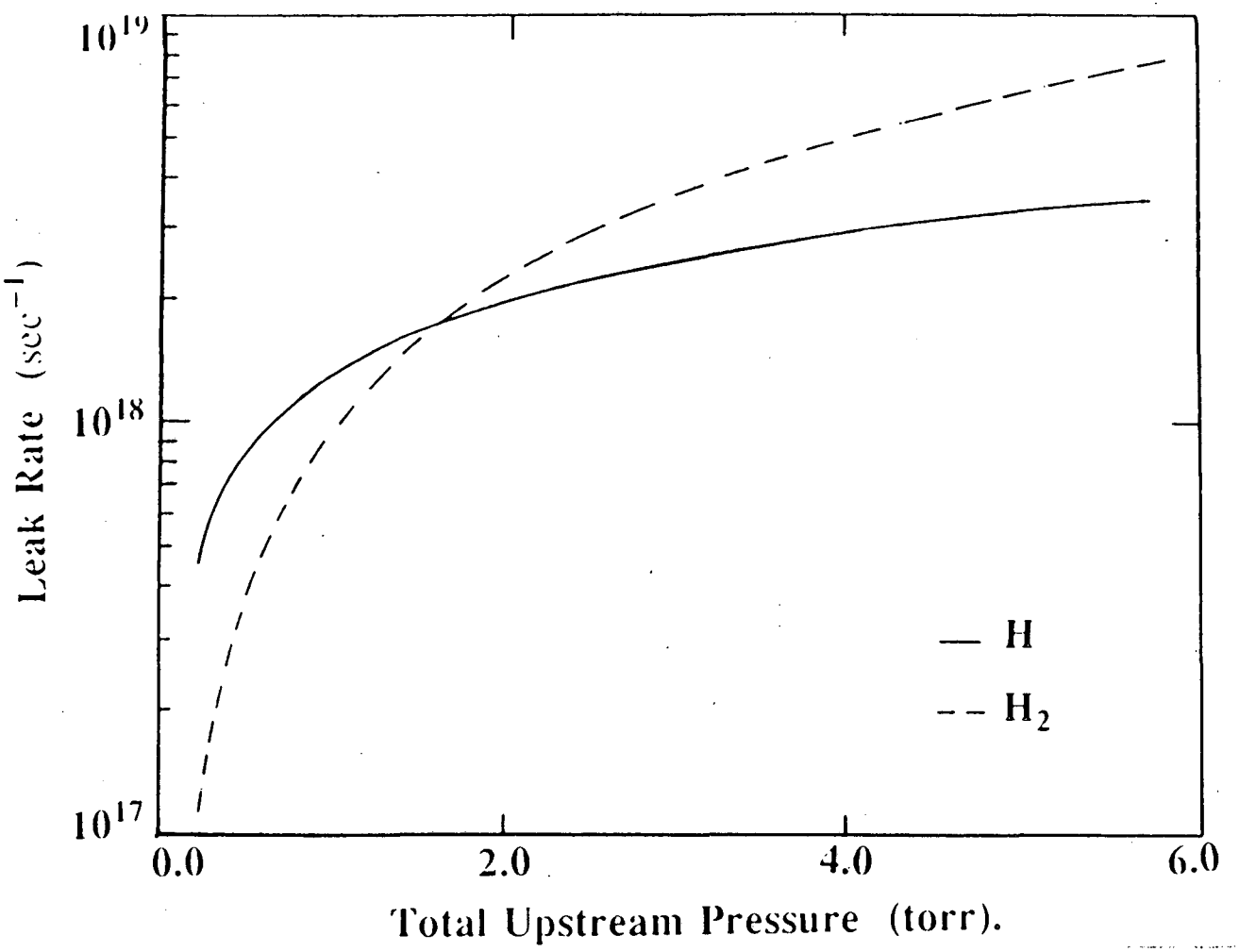


Fig. 3.4. A theoretical plot of molecular (broken line) and atomic hydrogen (continuous line) leak rates through the oven orifice versus upstream gauge pressure.

Hydrodynamic flow,

$$l_1 = \frac{1.898 l_T \xi}{1 + 0.949\xi} \tag{3.12}$$

$$l_2 = \frac{l_T}{1 + 0.949\xi} \tag{3.14}$$

Transition flow,

$$l_1 = (1 - \delta) l_1^f + \delta l_1^h \tag{3.15}$$

$$l_2 = (1 - \delta) l_2^f + \delta l_2^h \tag{3.16}$$

where superscripts *f, h* are the free molecular and the hydrodynamic components respectively; and $\delta$ is the fraction of flow which is hydrodynamic, and defined as;

$$\delta = \frac{\mathrm{Kn} - 1.6}{16.6 - 1.6} \tag{3.17}$$

The results of the theoretical computations and the experimental analysis are shown in figures 3.4 and 3.5.

The corresponding beam intensities of atomic and molecular hydrogen at the Si target surface are calculated by the substitution of appropriate leak rate equation into the following equation:

$$\mathrm{I}_r = \frac{l_r}{\pi \mathrm{d}^2} \quad \mathrm{r} = 1 \text{ or } 2 \tag{3.18}$$

where **d** is the distance between the oven orifice and the target surface.

### 3.5. The Modulation System

The beam effusing through the 1 mm orifice of the oven is mechanically modulated by a rotating slotted disc. The 3-inch diameter disc is driven by a synchronous two-phase motor (Globe #SC-53A 111-2) which is mounted in a water-cooled

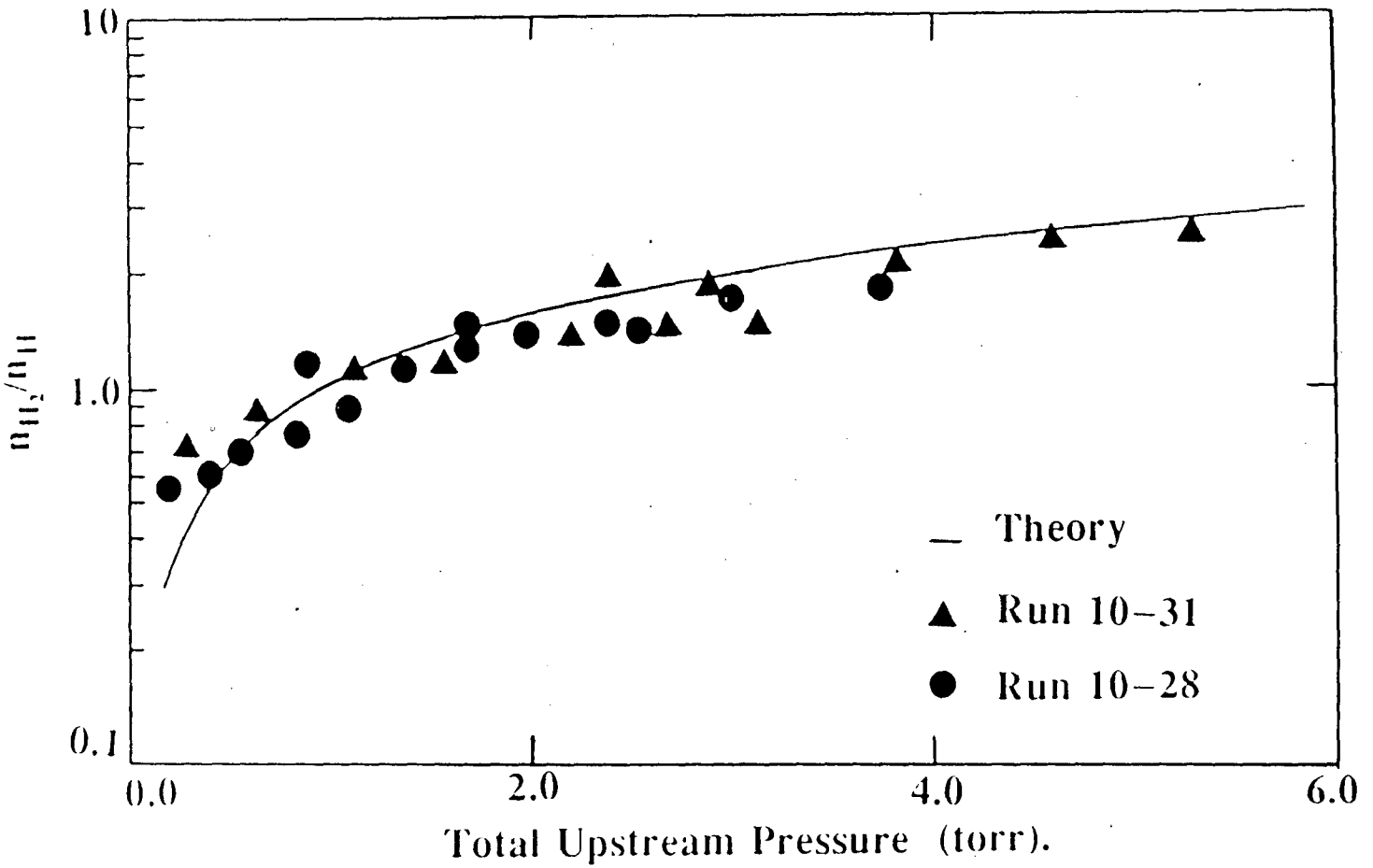


Fig. 3.5. The theoretical and the measured ratios of $H_2$ to H versus total upstream pressure with furnace at 2500 K.

brass block, fig 3.1. A symmetrically cut six-blade chopper provides a beam frequency twice the frequency of the power driving the motor. This frequency multiplication minimizes source interferences from vibrations in the motor.

The motor is powered by two Dynakit Mark III 60 watt amplifiers which are driven by a Hewlett Packard 203A audio oscillator. The oscillator provides two individually attenuated outputs with adjustable phase angle between them. The two phases of power to the motor are obtained by connecting a phasing capacitor in series with one winding.

The compactness of this system precludes the use of light and photocell to provide the reference signal. A technique that utilizes a strobe and the chopper blade position is used. In this method the chopper blade is viewed by a 25 power cathetometer under a synchronized stroboscope flash (General Radio 153-AB). Adjusting the delay of the strobe synchronous signal, the chopper blade is observed at a particular reference "position" coincident with this synchronizing pulse which is then used for the reference signal. A detailed description of the wiring is given in Ref. 35. The strobe is synchronized by a signal from the motor drive oscillator. In order to match the blade frequency the signal from the oscillator is doubled by a full-wave bridge rectifier fed through an audio-frequency isolation transformer from a square-wave output on the model 203A oscillator[38]. This derived chopping rate pulse train synchronizes two series-connected Data Pulse 101 generators which provide the required adjustable delay for the strobe-reference-synchronizing pulse.

### 3.6. Temperature Measurements

The temperature of the Si(111) surface is measured by an optical pyrometer (Leeds & Northrup Disappearing Filament Pyrometer) and/or an infra-red pyrometer (Ircon Radiation Thermometer 300C). The optical pyrometer was used to calibrate the infra-red instrument. Temperatures above 1000 K were measured by the optical

| True Temperature T, (K) | Brightness Temperature T', (K) | Correction $\Delta T$ | Spectral Emissivity $\varepsilon^{(39)}$ |
|---|---|---|---|
| 1572 | 1488 | 84 | 0.488 |
| 1505 | 1433 | 72 | 0.507 |
| 1435 | 1371 | 64 | 0.530 |
| 1357 | 1303 | 54 | 0.554 |
| 1323 | 1273 | 50 | 0.563 |
| 1278 | 1233 | 45 | 0.577 |
| 1233 | 1193 | 40 | 0.592 |

Table 3.2, Target surface temperature, $T_s$ calibration.

| True Temperature T, (K) | Brightness Temperature T', (K) | Correction $\Delta T$ | Spectral Emissivity $\varepsilon^{(40)}$ |
|---|---|---|---|
| 1882 | 1800 | 82 | 0.442 |
| 1994 | 1900 | 94 | 0.440 |
| 2107 | 2000 | 107 | 0.438 |
| 2221 | 2100 | 121 | 0.436 |
| 2336 | 2200 | 136 | 0.434 |
| 2452 | 2300 | 152 | 0.432 |
| 2569 | 2400 | 169 | 0.430 |
| 2688 | 2500 | 188 | 0.428 |

Table 3.3, Tungsten oven temperature calibration.

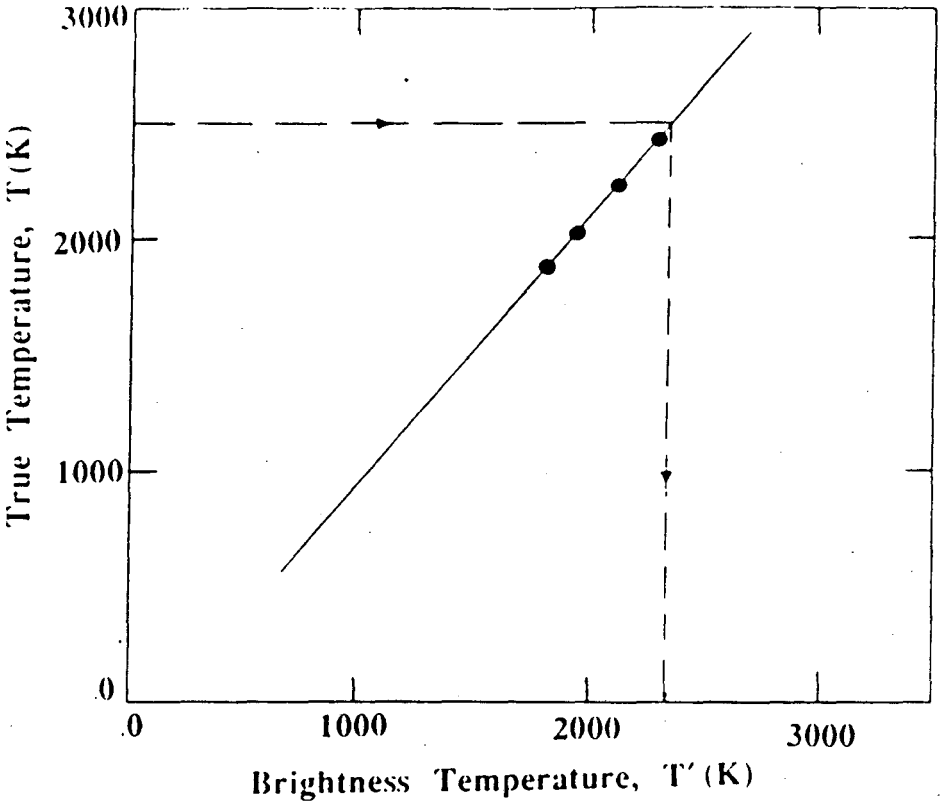


Fig. 3.6. Calibration of tungsten furnace temperature. The broken line indicates the brightness temperature (2350 K) which corresponds to an oven temperature of 2500 K.

pyrometer through a sapphire window. These temperatures were corrected for the window and emissivity using the relation

$$\frac{ch\Delta T}{\lambda kTT'} = -A - \ln\varepsilon(\lambda,T) \tag{3.19}$$

where $\lambda$ = effective wavelength of pyrometer = 0.65 $\mu$m; c, h and k are the velocity of light, Planck's and Boltzmann's constants, respectively; A is the window correction factor = $3.63 \times 10^{-6}$; T = true surface temperature; T' = brightness temperature; and $\Delta T = T - T'$. Table 3.2 shows the measured data.

The tungsten oven temperature (Table 3.3) was measured by the optical pyrometer sighted through a glass window in the source chamber. The true oven temperature was deduced using Eq. (3.19). A plot of true temperature versus the brightness temperature Fig 3.6, shows the brightness temperature that corresponds to the required oven temperature of 2500 K.

### 3.7. The Detection System

The mass spectrometer used to detect the species reflected and desorbed from the target surface has an EAI quadrupole mass filter and ionizer, and a Galileo Channeltron (4800 Series) electron multiplier. The head assembly is positioned in the flight path of the collimated beam desorbing from the target surface. A fraction ($\approx 10^{-4}$) of the neutral particles in the beam is ionized and mass filtered through the quadrupole to the electron multiplier.

The modulated current from the multiplier is dropped across a 0.75 megohm AC resistance of Princeton Applied Research (PAR) type D differential preamplifier. The voltage drop is then processed in analog form by PAR HR-8 lock-in amplifier which provides the first Fourier component of the modulated signal. The output signal from the lock-in amplifier is fed to a PAR 127 two-phase accessory. The two-

component output (in-phase and quadrature) from the accessory are connected to a Heath dual pen chart recorder. Depending on the strength of the signal and the background noise level, the time constant of the two-phase accessory is set to give a reasonable steady trace by the recorder. The reference signal from the strobe and the lock-in amplifier internal frequency signal are monitored and synchronized on a dual beam Tektronix oscilloscope.

The complete waveform of the signal is obtained by feeding the AC current signal from the electron multiplier to a multi-channel analyzer(Tracor Northern TN-1710).

# 4. EXPERIMENTAL RESULTS

## 4.1. Target Surface Characteristics

Surface characterization of the silicon samples is essential for the basic understanding of the kinetics, mechanism and possibly dynamics of the gas-solid reaction. The major difficulties were the achievement of:

i) a clean surface, and

ii) a surface free of roughness other than that caused by the surface reaction with the atomic hydrogen beam.

The epitaxial Si(111) samples had a protective native oxide surface which is easily removed by annealing at 1273 K in vacuum. However, AES analysis of the Si(111) left in the chamber at an ambient pressure $\approx 10^{-8}$ torr shows (fig. 4.1a) a surface that is contaminated with carbon, oxygen and nitrogen. Steps were taken to ensure a cleaner surface prior to each molecular beam experiment. The samples, which were required to fit into a 6-mm diameter holder, were broken off of 5-cm-diameter wafers supplied by Epitaxy Inc. using a sharp-pointed diamond tip. Surface particles from the breakage were blown off by a dry nitrogen gas. This method was used to prevent contamination of the surface of the as-received samples, which normally results from other cutting procedures[41].

With the exception of carbon, concentrations of the other impurities were controlled at levels below the detection limits of the AES analyzer (fig. 4.2b). This was achieved by heating the target at 1273 K with the molecular beam on for a period of one hour and in situ monitoring the surface by the AES. The choice of the 1273 K temperature is discussed later in this section. The surface always had traces of carbon (possibly as SiC) and its effect on the surface reaction could not be accurately characterized.

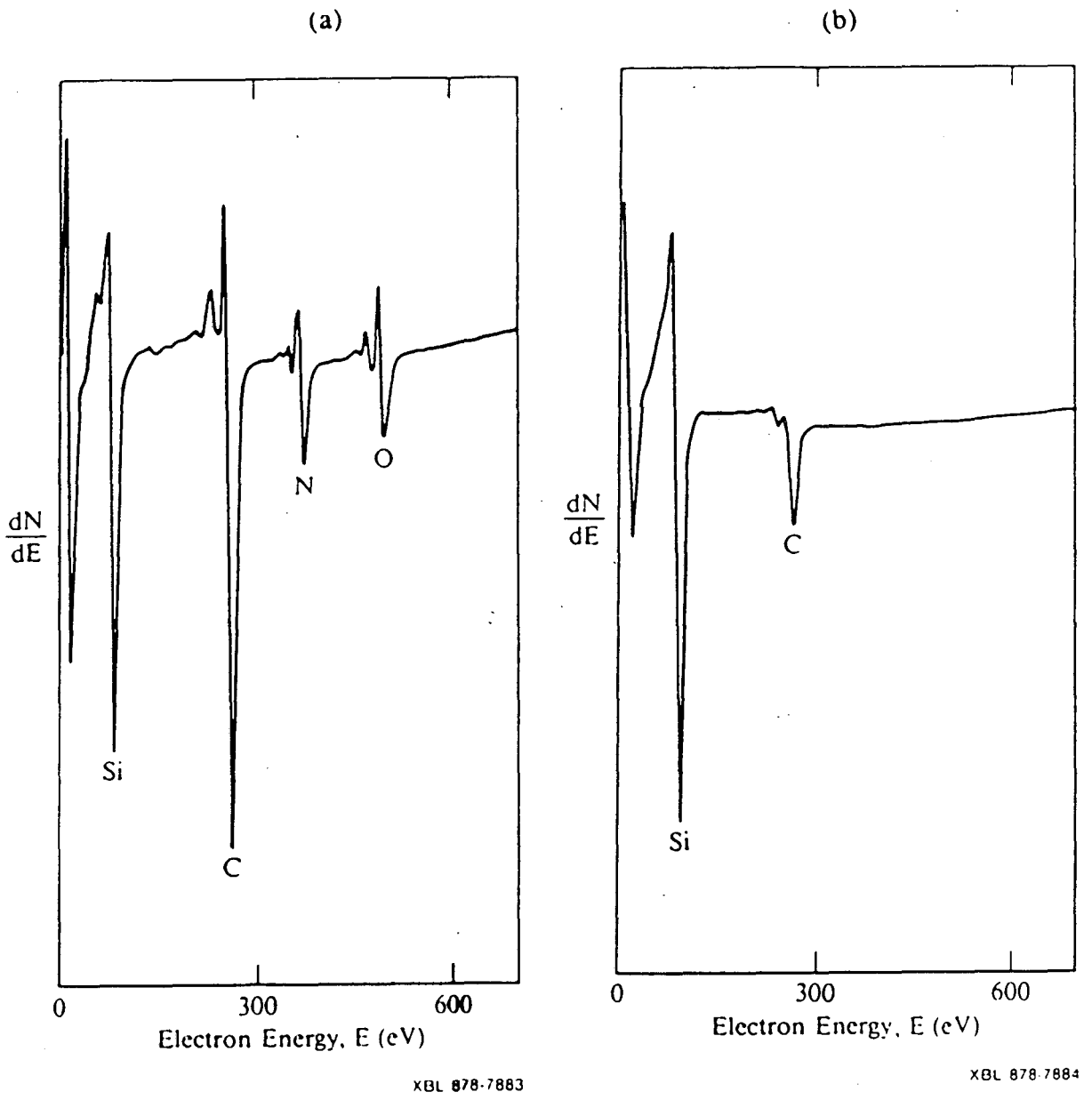


Fig. 4.1. AES spectra of Si(111) surface showing the surface contaminants; (a) the sample is not heated and (b) sample is heated at 1200 K for a period of one hour.

Reacted and unreacted samples taken from the molecular beam system were analyzed with a scanning electron microscope (SEM). Results are shown in figs. 4.2 and 4.3. The SEM revealed formation of triangular pits when heated above 1273 K (fig. 4.2a) However, samples which were heated below 1273 K did not show this feature (figs. 4.2b & 4.2c). Hence an annealing temperature below 1273 K was chosen for all samples. The samples which were exposed to atomic hydrogen beam showed a rougher morphology under the SEM (fig. 4.3), A surface analysis by a profilometer gives a peak-to-peak roughness of about 0.25 $\mu$m for 1.3 $\mu$m depth of etching.

## 4.2. Reaction Product Measurements

Only two reaction products were detected; silicon tetrahydride, $SiH_4$, and recombined $H_2$ from the surface-adsorbed H. The $SiH_4$ product cracks in the mass spectrometer ionizer to major species such as $Si^+$, $SiH^+$, $SiH_2^+$ and $SiH_3^+$ with m/e ratios of 28, 29, 30 and 31 respectively. These fragmentation species arise from the $SiH_4$ product because: (i) they have equal phase lags and (ii) the cracking pattern (Appendix II) calculated from the signals agrees well with a direct measurement of the $SiH_4$ cracking pattern[120].

### 4.2.1. Silane Production

The $SiH_4$ signal was directly measured by the mass spectrometer in the detection chamber as a function of target temperature, atomic hydrogen beam intensity and modulation frequency. During the experiment two of these three variables were fixed while the third was scanned within the accessible range.

The temperature dependences of the apparent reaction probability (fig. 4.4) and the phase lag (fig. 4.5) provide the tool for estimating the activation energies in the rate constants of the proposed reaction mechanisms. The data show that the

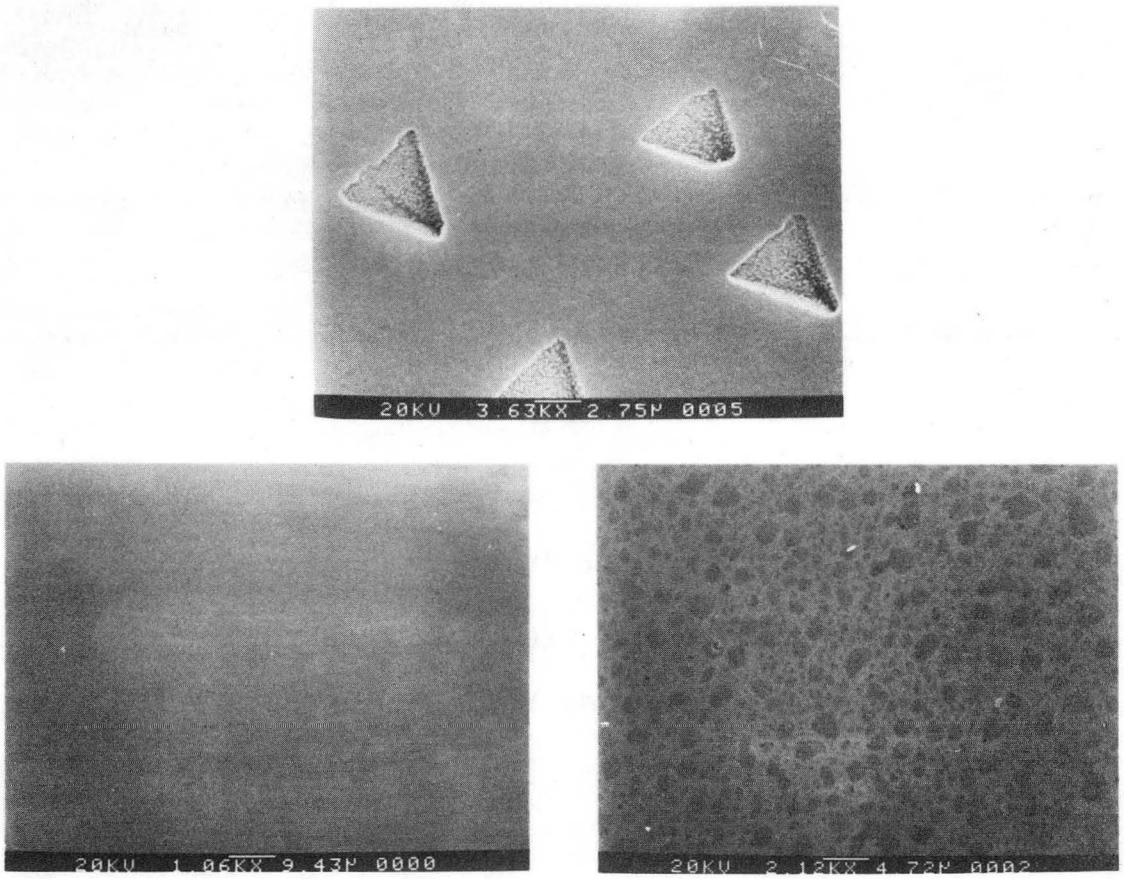


XBB 879-7829A

Fig. 4.2. SEM surface morphology of unreacted Si(111) but annealed at different conditions in UHV. (a) Shows the triangular pits, ≈ 5$\mu$m in sizes formed by heating Si at 1400 K for more than an hour. (b) Si sample was annealed for an hour at 1200 K (c) Sample was heated at 1270 K for more than one hour.

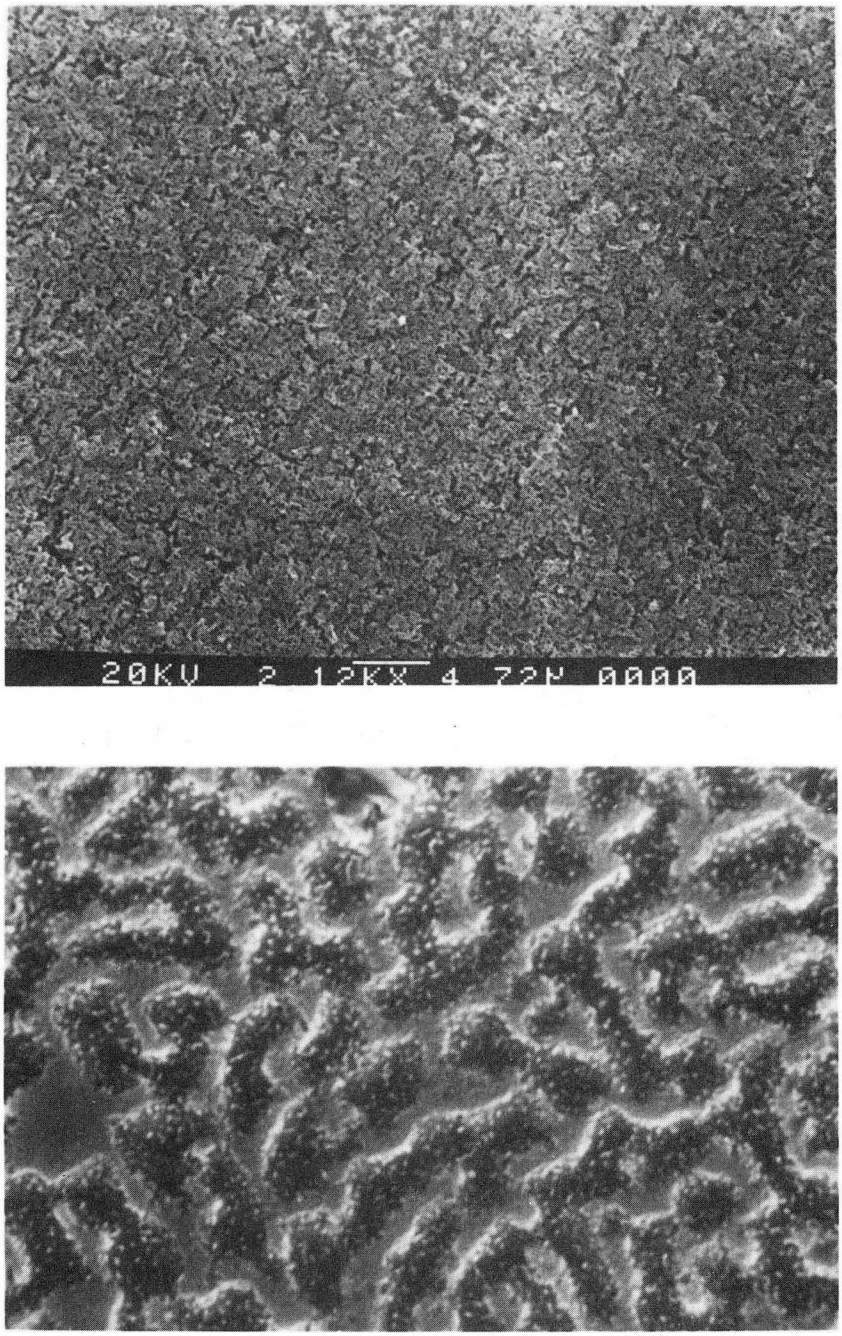


XBB 879-7827A

Fig. 4.3. SEM surface morphology of reacted Si(111) (a) The edge of the molecular beam region on the target surface where the beam intensity is low. (b) The center of beam spot on the Si surface where the intensity and the etching rate is highest.

reaction probability is highest at the lowest temperature and decreases with increasing temperature up to the range where Si is known to undergo a surface structure transformation. The corresponding phase lag is lowest at the ambient temperature and increases with increasing temperature. The behavior of both the apparent reaction probability and phase lag is diametrically opposite from what is usually observed for most gas-surface reactions, the exception being the reaction of hydrogen with the basal plane of graphite[5].

At temperatures above the surface structure transition the responses of the reaction probability and phase lag to increasing temperature are reversed (figs. 4.4 & 4.5) to the usual trends of most gas-surface reaction. Such a discontinuity was observed by Farnaam and Olander[41,43] in the reverse reaction of $SiH_4$ cracking on Si(111) and by Madix et al. in the reaction of chlorine with the same surface[44]. Silicon has a stable low temperature reconstructed surface structure designated as Si(111)-7x7. This structure has been observed using LEED by Lander, Florio et al. and Bennet et al.[45–47] to undergo second-order surface structure transformation to an unreconstructed, disordered Si(111)-1x1 surface structure in the temperature range 1138 K to 1163 K. Thus the temperature response to the reaction probability and the phase lag demonstrates strong structural sensitivity to the surface reaction. Due to the difficulty in obtaining a complete set of molecular beam data above 1273 K, a model was proposed to fit the data only at temperatures below 1000 K.

The reaction probability and phase lag dependence on the atomic hydrogen beam intensity are shown in fig. 4.6 for two modulation frequencies. These measurements provide information pertaining to the order of the reaction. The data show a linear dependence of silane production on the beam intensity.

The frequency dependence of apparent reaction probability and phase lag are shown in fig. 4.7. The apparent reaction probability shows no appreciable change

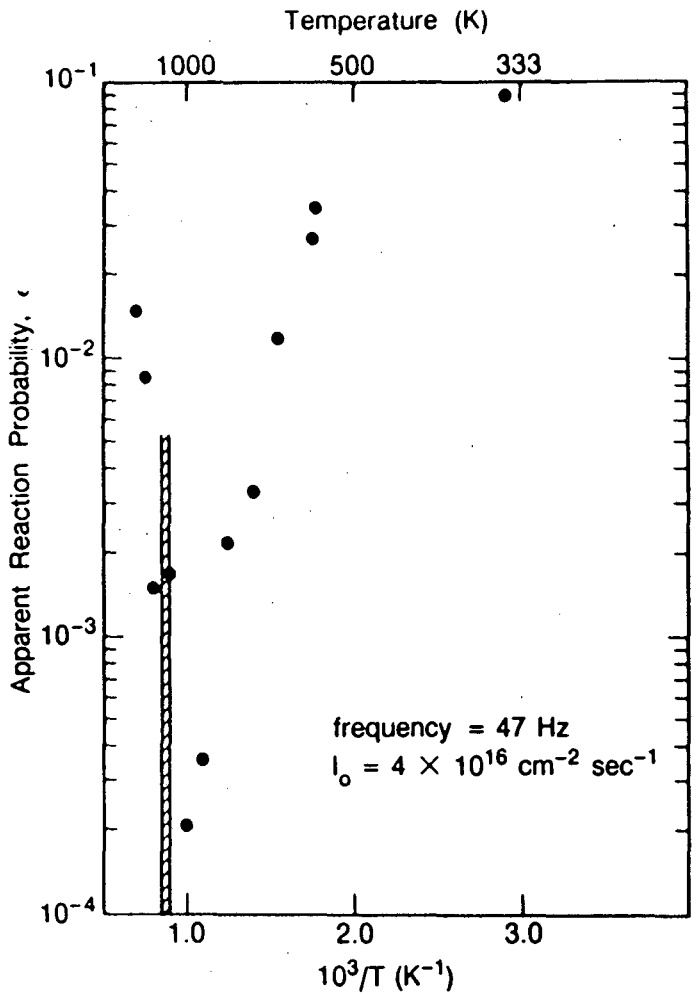


XBL 874-7662

Fig. 4.4. Arrhenius plot of the experimental apparent reaction probability for a frequency of 47 Hz and H beam intensity of $4 \times 10^{16}$ atoms cm$^{-2}$ sec$^{-1}$. The shaded band is the temperature range where Si(111)-7x7 transforms to Si(111)-1x1. The plotted points represents $\varepsilon/(1-\eta)$. So to obtain exact value of $\varepsilon$ the points should be multiplied by $1-\eta$. Note: This is applicable to all the plots of apparent reaction probability.

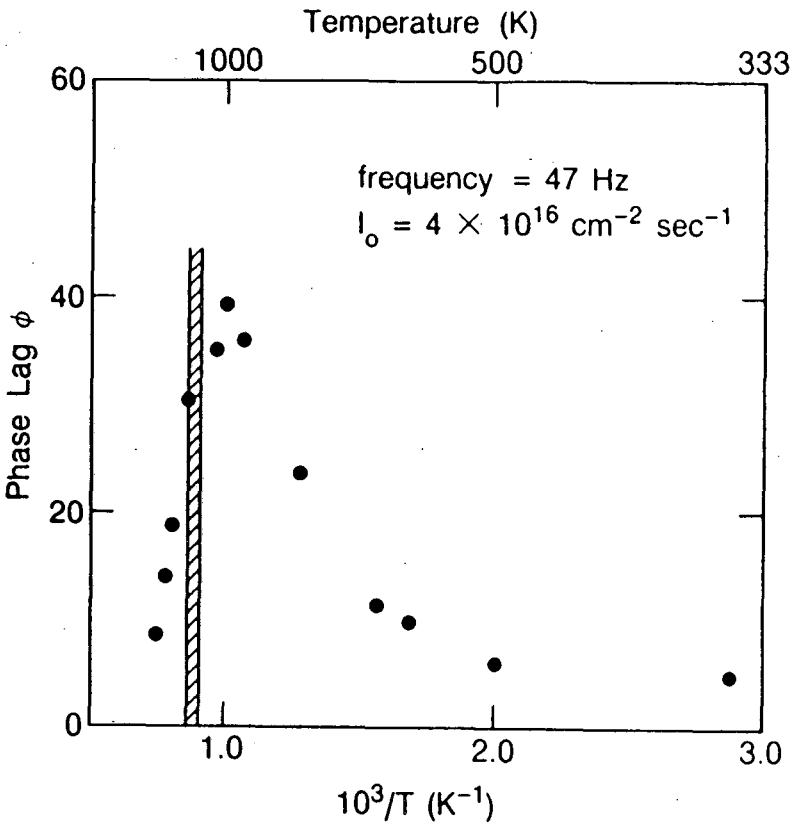


XBL 874-7661

Fig. 4.5. Variation of the measured phase lag with reciprocal temperature at the same experimental conditions as in fig. 4.4.

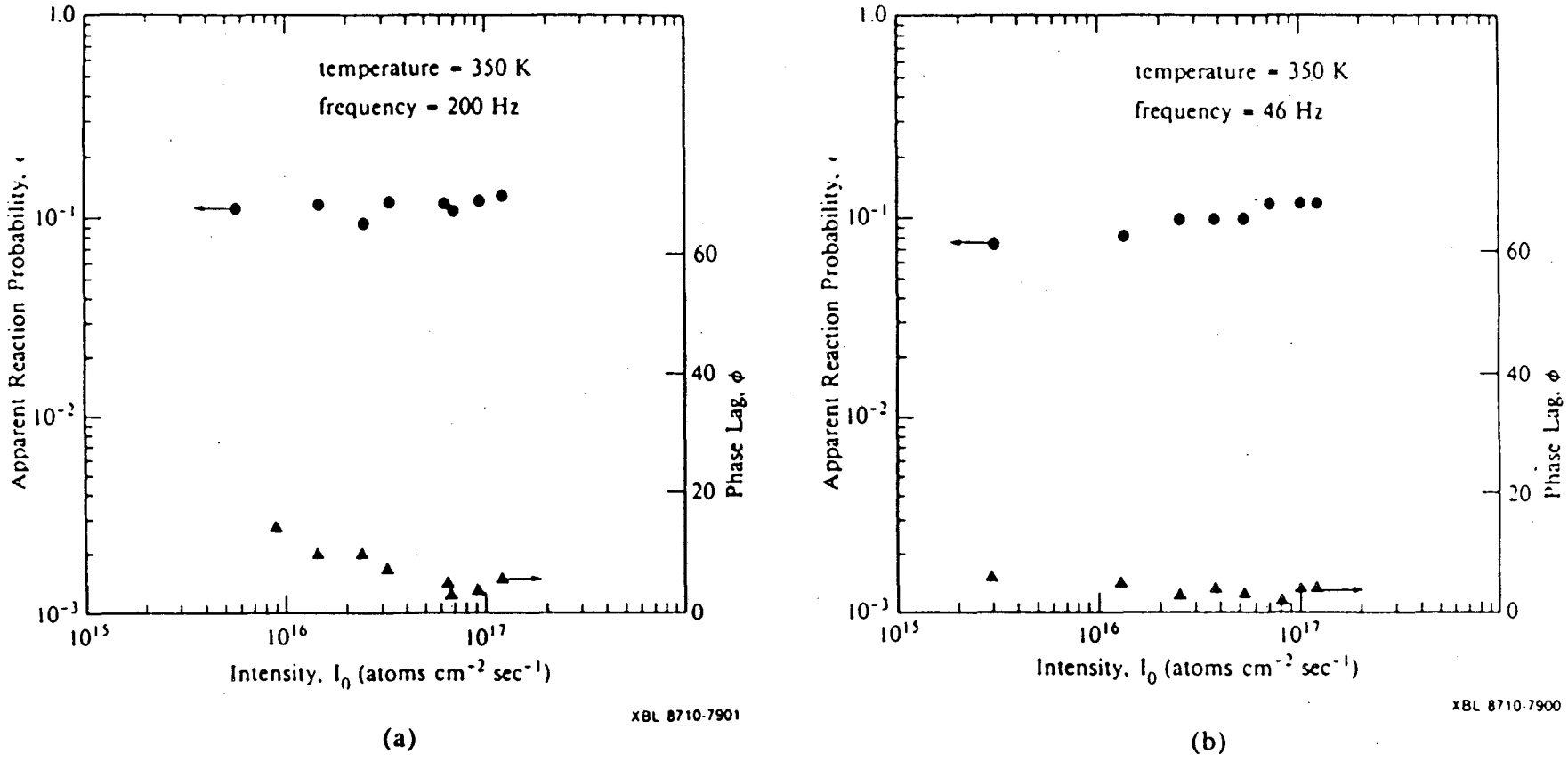


Fig. 4.6. The measured apparent reaction probability and phase lag versus beam intensity at two frequencies: (a) frequency = 200 Hz and (b) frequency = 46 Hz.

with frequency changes. Such a small change in $\varepsilon$ is a signature of a fast surface chemical reaction with respect to the time scale of the beam modulation. The phase lag, which is small at low frequency also changes slowly with increasing frequency. However, at 600 K (fig. 4.7b), there is a pronounced effect of frequency on the phase lag. This enhanced effect at high temperature on the frequency response of phase lag could be due to an effect of bulk-solution diffusion of the surface-adsorbed H atoms.

### 4.2.2. Molecular Hydrogen Reaction Product

The measured $H_2^+$ signal includes the scattered $H_2$ from the undissociated component of reactant beam source and the $H_2$ produced by recombination of surface-adsorbed H. $H_2^+$ produced by cracking of $SiH_4$ is negligible. The $H_2^+$ signal was measured as functions of all the three experimental variables (tables 4.1 - 4.3). The extraction of the recombination product $H_2$ component of this signal had to be determined by a second mass spectrometer measurement of the primary beam signals of $H_2$ and H (second column in tables 4.1 - 4.3). A second mass spectrometer was placed in the beam flight path in the target chamber. The target was retracted for this experiment. An experimental data analysis in Appendix II gives following equation which explicitly relates the $H_2$ apparent reaction probability to various measured quantities:

$$\frac{\varepsilon_2}{1-\eta} = 0.0149\sqrt{T}\left\{\frac{S_2^0}{S_1^0} - \frac{S_2^d}{(1-\eta)S_1^d}\right\} \tag{4.1}$$

where $S_2^0$ and $S_1^0$ are the signal amplitudes of $H_2$ and H, respectively, from the mass spectrometer in the detection chamber with the target in place and $S_2^d$ and $S_1^d$ are the corresponding direct beam signals. The bare surface sticking probability, $\eta$, is one

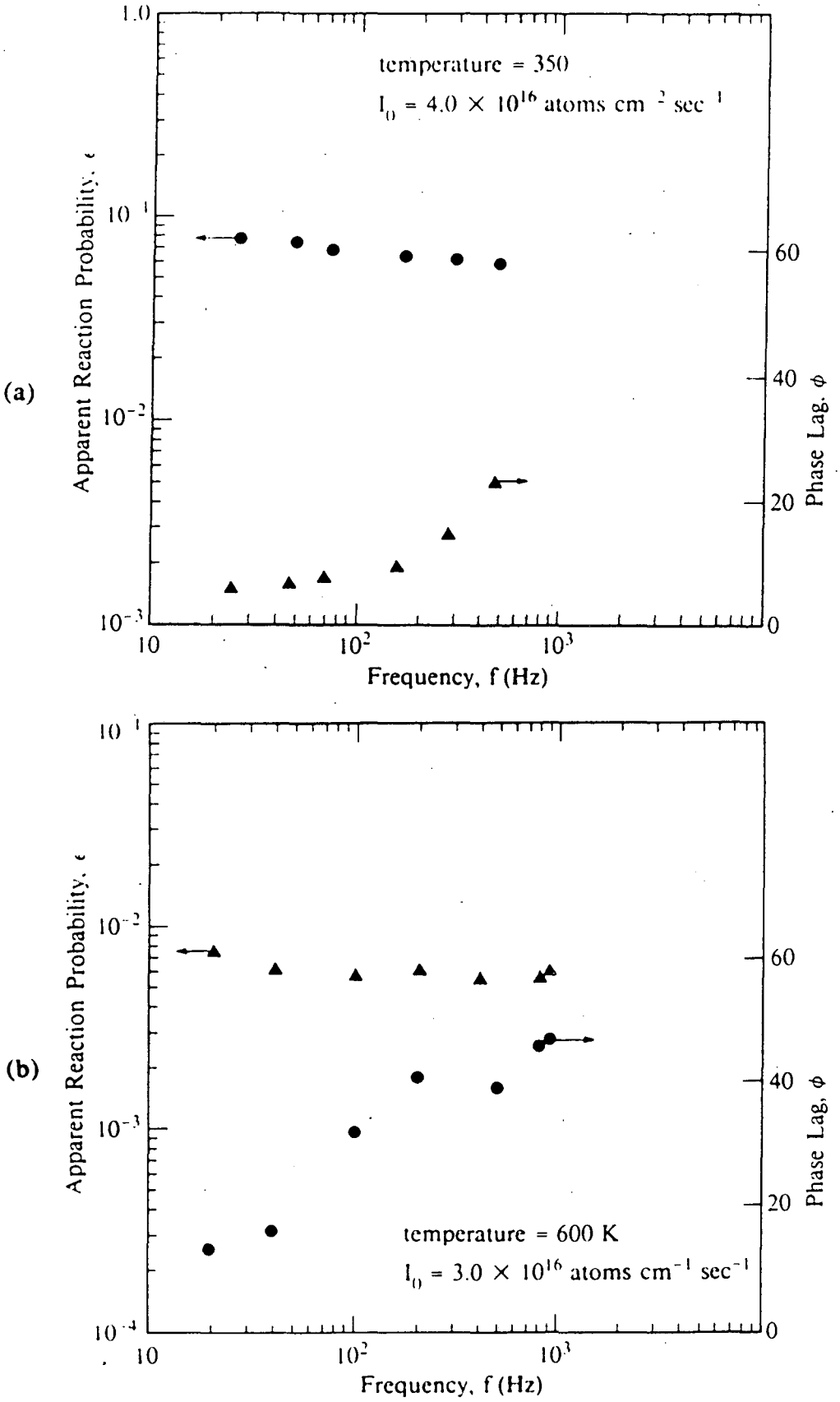


Fig. 4.7. The experimental apparent reaction probability and phase lag versus frequency: (a) temperature = 350 K and $I_0 = 4 \times 10^{16}$ atoms cm$^{-2}$ sec$^{-1}$ and (b) temperature = 600 K and $I_0 = 3 \times 10^{16}$ atoms cm$^{-2}$ sec$^{-1}$

of the fitting parameters of theoretical model and is not directly determined experimentally. Hence the results of this experimental analysis are deferred to the discussion section. However, $\eta$ is chosen to generate $\varepsilon_2$ values that reflect the signal ratios of H and $H_2$ in both measurements.

| Temp. (K) | $R_1$(%) | $R_2$(%) | $\varepsilon_2$ |
|---|---|---|---|
| 350 | 46 | 5.83 | 0.36 |
| 563 | 46 | 5.00 | 0.65 |
| 569 | 46 | 5.30 | 0.57 |
| 643 | 46 | 5.50 | 0.55 |
| 713 | 46 | 5.80 | 0.52 |
| 787 | 46 | 5.10 | 0.68 |
| 883 | 46 | 5.60 | 0.62 |

Table 4.1. Temperature dependence of H and $H_2$ ratios. $R_1 = S_1^d/S_2^d$ is the primary beam measurement and $R_2 = S_1^0/S_2^0$ is that of the reflected beam. f = 47 Hz; $I_0 = 4.4 \times 10^{16}$ atoms $cm^{-2} sec^{-1}$; and $\eta = 0.8$.

| $I_0 x 10^{-16}$(atoms/$cm^2$–sec) | $R_1$(%) | $R_2$(%) | $\varepsilon_2$ |
|---|---|---|---|
| 0.60 | 85 | 15.7 | 0.20 |
| 1.04 | 75 | 13.0 | 0.27 |
| 1.84 | 63 | 11.2 | 0.30 |
| 3.24 | 52 | 9.2 | 0.37 |
| 6.55 | 37 | 7.2 | 0.41 |
| 9.01 | 29 | 6.3 | 0.37 |
| 12.60 | 22 | 4.0 | 0.82 |

Table 4.2. Intensity dependence of H and $H_2$ ratios. $R_1$ and $R_2$ are defined in Table 4.1; f = 24 Hz; T = 350 K; and $\eta = 0.7$.

For example, at 1 torr upstream beam pressure, T = 350 K and frequency of 24 Hz, the primary beam ratio $S_1^d/S_2^d$ is 0.5 whereas the emitted hydrogen signal ratio $S_1^0/S_2^0$ is 0.1. Thus if $\eta = 0.7 \pm 0.1$, $\varepsilon_2 = 0.3$. The estimated sticking probability $\eta$ is the average of all values of $\eta$ similar to those indicated in Tables 4.1-4.3 that satisfy the condition that when it is substituted in Eq. (4.1) it gives an $\varepsilon_2$ which falls within the range: $0 \leq \varepsilon_2 \leq 1$.

Phase lag measurements for recombined $H_2$ product could not be determined because the large portion of the reflected $H_2$ signal was due to the scattered $H_2$ and also because the recombination reaction was fast.

| Frequency (Hz) | $R_1$(%) | $R_1$(%) | $\varepsilon_2$ |
|---|---|---|---|
| 24 | 49 | 14.0 | 0.23 |
| 47 | 49 | 11.3 | 0.42 |
| 70 | 49 | 12.0 | 0.35 |
| 164 | 49 | 12.1 | 0.35 |
| 280 | 49 | 11.3 | 0.42 |
| 470 | 49 | 12.6 | 0.32 |

Table 4.3. Frequency dependence of H and $H_2$ ratios. T = 350 K; $I_0 = 3.7 \times 10^{16}$ atoms $cm^{-2}$ $sec^{-1}$; and $\eta = 0.6$.

### 4.3. Ion Enhancement

There have been several observations in which gas-solid surface reactions have been enhanced by simultaneous irradiation with energetic ions. Ion-enhanced reactions of silicon with $XeF_2$, $F_2$ and $Cl_2$ to form volatile products (e.g. $SiF_4$ and $SiCl_4$) by 2-3 keV, 20 $\mu$A $cm^{-2}$ $Ar^+$ have been reported in the literature[48-54]. Different models have been proposed by these authors for this effect: Winters and

co–workers[53] suggested an increase in the dissociative chemisorption of the reactant gas ($XeF_2$), at the surface; Gerlach–Mayer[50] proposed an excitation of the $SiF_2$ complex on the surface.

In addition to investigation of possible ion effects on the reaction of hydrogen beam with Si(111), the simultaneous bombardment of the Si by ion and molecular beams was performed. The Si surface was exposed to 2 - 3 keV $20\,\mu A\,cm^{-2}$ $Ar^+$ during a molecular beam experiment. The detected $SiH_4$ product and the reflected $H_2$ and H signals by the mass spectrometer were monitored while the $Ar^+$ was turned off and on. There was no effect of the ion bombardment on the measured signals of $SiH_3^+$, $H_2^+$ and $H^+$.

The fact that ions did not have any effect on the surface reaction could be explained by the mechanism suggested by Winters et al.[53] which assumes an enhancement of dissociative adsorption of the reactant gas ($XeF_2$). In the present case, adsorption of the $H_2$ portion of the molecular beam is negligible compared to the H atoms so enhancement by the Winters' mechanism is absent. This explanation eliminates any simulation of a step which would be more likely to be affected by ion bombardment.

### 4.4. Molecular Hydrogen Effect

The reactant gas source contains a mixture of molecular and atomic hydrogen. Even though preliminary experiments indicated that Si does not react with pure molecular hydrogen, its effect on the reaction intermediates had not been established. In an experiment designed to ascertain the possibility of this effect, two beams were used: the modulated molecular beam source of $H_2$ and H; and undissociated and unmodulated beam of $D_2$. The latter was leaked through a doser close to the surface. The doser was attached to a flange on the target-holder. The inability

of $H_2$ to react with Si means it could not effectively stick to the surface or dissociate on Si. Thus one of the plausible products that will result from the reaction of $D_2$ with the reaction intermediates is $SiH_2D_2$. Based on the same cracking pattern of $SiH_4$ (section 4.2), $SiH_2D_2$ should have produced $Si^+$, $SiH^+$, $SiH_2^+$, $SiHD^+$, $SiD_2^+$, $SiH_2D^+$ and $SiD_2H^+$ with m/e ratios of 28, 29, 30, 31, 32, 32 and 33 respectively. Thus in addition to the original observed peaks when the modulated beam was operated alone, two peaks should have been observed at m/e ratios of 32 and 33 if any $SiH_2D_2$ were formed. The results of this experiment were negative; there was no effect of $D_2$ on the mass distribution of the silane reaction products.

### 4.5. Hydrogen Solubility in Silicon

The response of phase lag to temperature changes in the modulated molecular beam results is unusual and very sluggish at high temperatures. A plausible explanation of this increase in phase lag with increasing temperature is bulk solution-diffusion of surface-adsorbed H atoms.

To investigate bulk solution and diffusion of the surface-adsorbed H atoms as a possible step in the mechanism of the molecular beam interaction with Si(111), an experiment was designed to measure the solubility of hydrogen in crystalline silicon as a function of both pressure and temperature.

The details of the experimental apparatus is discussed elsewhere (Ref. 64) and will not be described here. Two sequential procedures were used: one was the infusion of hydrogen into silicon followed by an outgassing and detection of the dissolved hydrogen. The former was performed in an induction furnace (fig. 4.8) at high pressures. Samples housed in a molybdenum crucible were placed in an induction coil. The chamber was evacuated with diffusion and mechanical pumps to a background pressure of $\approx 10^{-5}$ torr. It was then filled to the desired pressure with

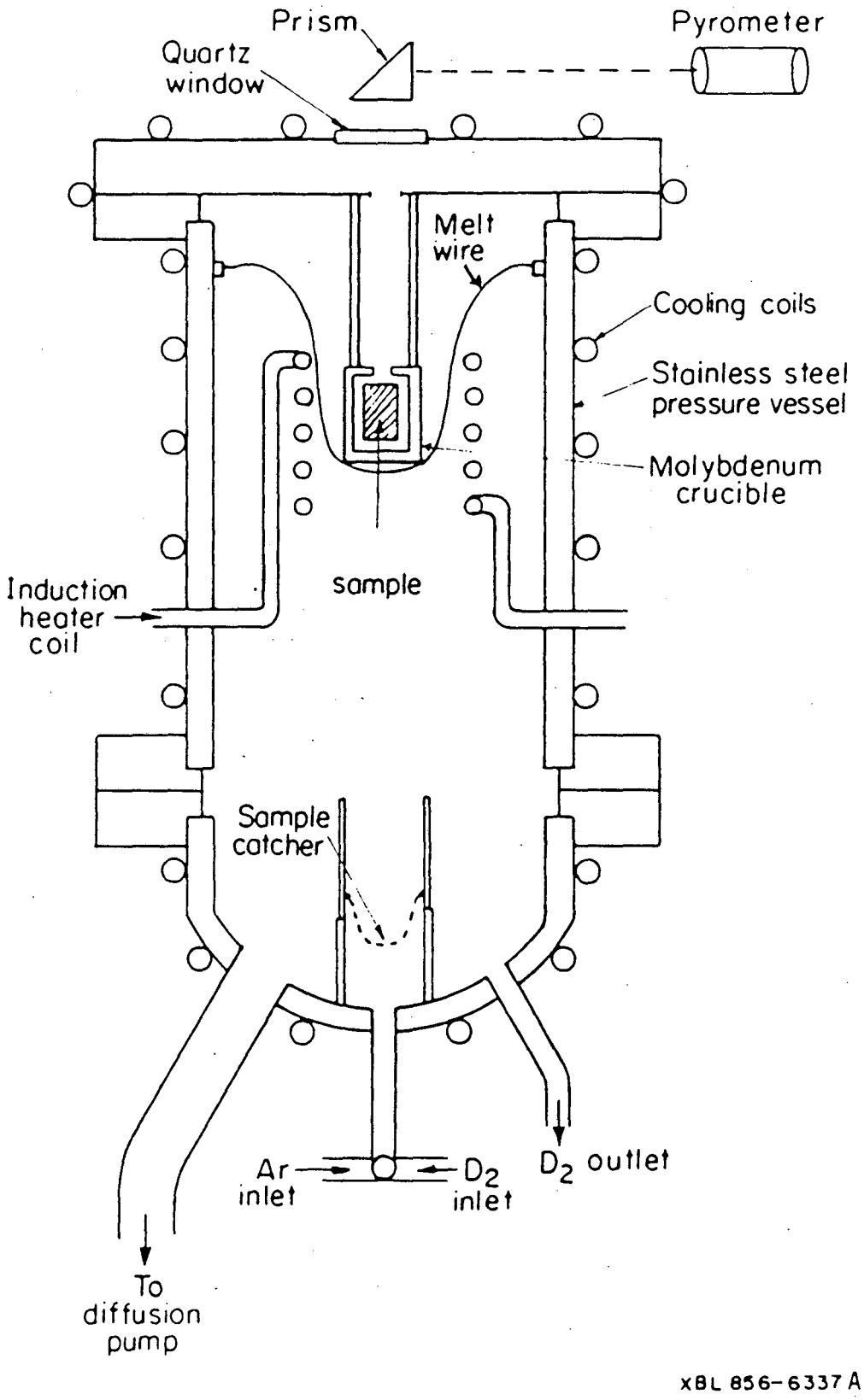


Fig. 4.8. Schematic of the induction furnace system.

high-purity deuterium and heated inductively to the required temperature for a period of one hour in order to establish thermodynamic equilibrium. The sample temperatures were measured through a simulated black hole by an optical pyrometer which was calibrated so that the effects of a glass window and a prism were corrected. The deuterium-saturated specimens were quenched by dropping them to the bottom of the chamber. After the infusion process, samples were removed from the induction system and taken to an outgassing system.

The outgassing system (fig. 4.9) is a high vacuum chamber pumped by mechanical and diffusion pumps. A background pressure of $\approx 10^{-6}$ torr is achieved under no load. The chamber contains a molybdenum crucible placed inside a resistively heated tungsten mesh, a quadrupole mass spectrometer and a mechanical chopper.

Prior to an outgassing test, helium gas was passed through the system for mass spectrometer calibration of m/e ratio = 4, as well as the calculation of deuterium release-rate from the samples. In the latter calibration, a reservoir of known helium pressure was leaked into the system for a period of time. The peak mass spectrometer signal in conjunction with the ideal gas equation was used to estimate the helium flow rate. This was corrected for mass spectrometer constants to obtain an expression (Eq. 4.2) that relates deuterium release-rate to the measured mass spectrometer signal.

$$\dot{N}_{D_2} = 0.2044\, S_{D_2^+}(\mu V)\ \ \mu g\ D_2/\min. \tag{4.2}$$

The helium beam and the outgassing hydrogen effusing through a stainless steel tube are modulated by the mechanical chopper (to improve the signal-to-noise ratio) and analyzed by the mass spectrometer using lock-in detection. The amplitude of the signal of the lock-in amplifier is converted to deuterium release-rate using Eq. 4.2.

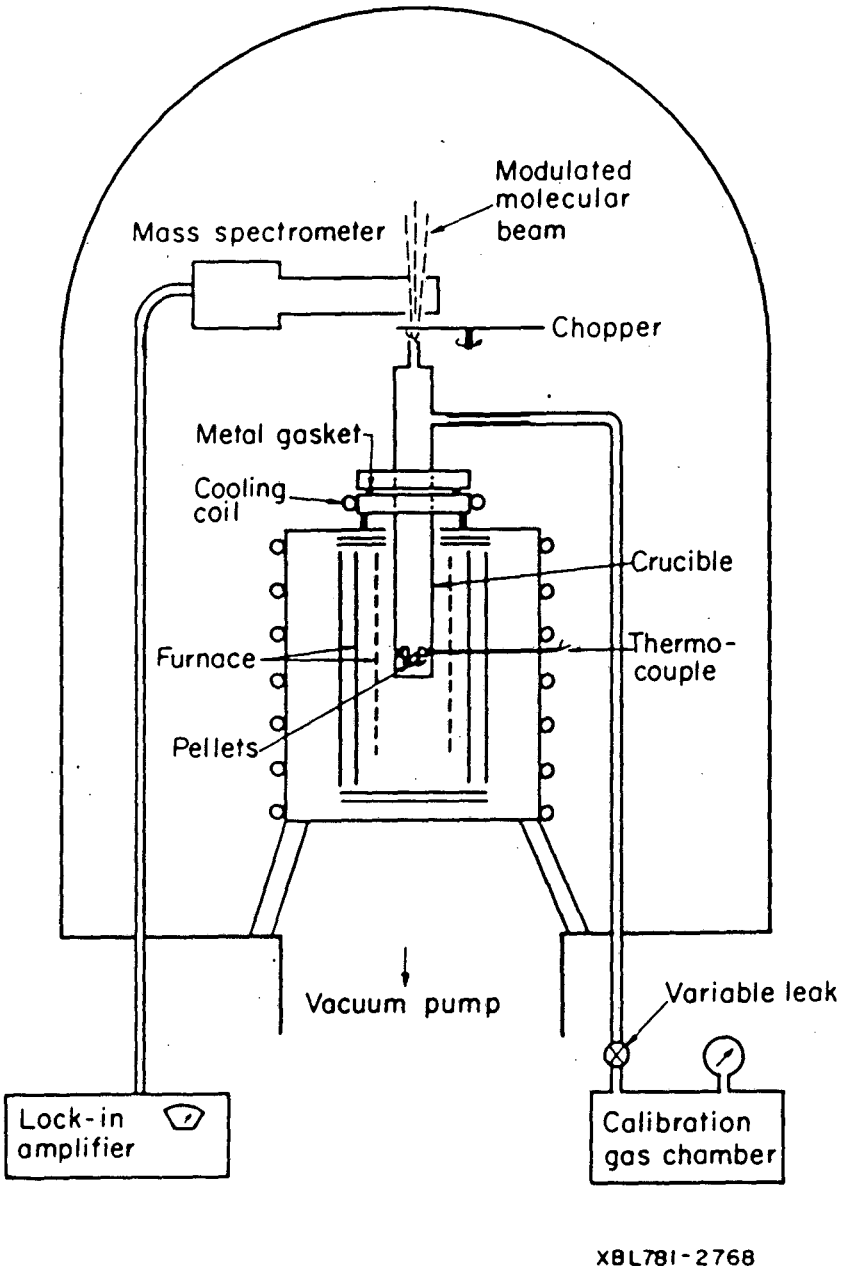


Fig. 4.9. Schematic of the outgassing system.

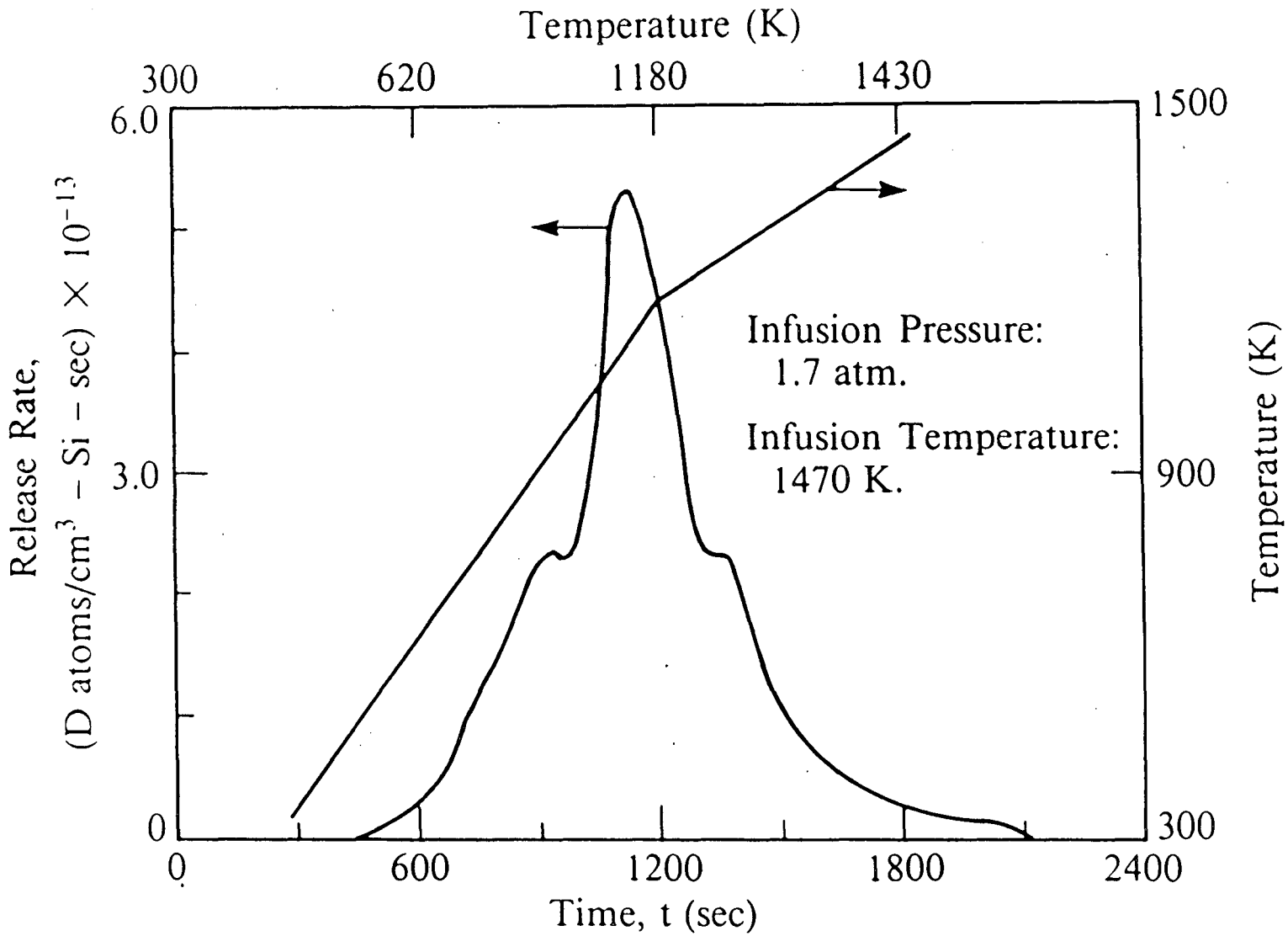


Fig. 4.10. A desorption spectrum of deuterium release-rate from crystalline silicon at heating rates of 0.93 K/sec for (300-1100 K) and 0.47 K/sec for (1100-1400 K). Infusion time is 1 hr. and sample weight is 0.4 gm.

Fig. 4.10 shows one of the temperature-increase release curves of deuterium from the silicon. The temperature ramp rate was measured by a thermocouple. To prevent melting of the silicon samples in the furnace, the power input to the heater could not be increased any further at temperatures above 1200 K. This effect made it difficult to achieve a continuous linear heating rate throughout a release process. Hence the temperature ramp curve is fitted with two linear heating rates, $\beta'_1$ and $\beta'_2$.

The areas under the release-rate curves give the solubilities of deuterium in single crystal silicon at the infusion temperature and pressure. Results are listed in Tables 4.4

| Pressure (atm.) | Solubility x $10^{-16}$ (atoms $cm^{-3}$) | $K_s$ x $10^{-16}$ (atoms $cm^{-3}$ $atm^{-1/2}$) |
|---|---|---|
| 1.7 | 2.40 | 1.84 |
| 3.0 | 2.39 | 1.39 |
| 3.7 | 3.02 | 1.57 |
| 3.7 | 3.72 | 1.93 |
| 4.4 | 2.70 | 1.29 |
| 9.2 | 5.52 | 1.81 |

Table 4.4. Pressure dependent solubility measurements at 1450 K. The infusion time was one hour. $K_s$ is calculated from Eq. (4.4).

A regression line fit (fig. 4.11) to the data in Table 4.4 gives a slope of 0.5. This is an indication that hydrogen dissolves in the Si lattice as atomic hydrogen. In this atomic form hydrogen could be located at any one of a number of sites:

(a) The extended Hückel theory (EHT) calculation discussed by Singh et al.[65]

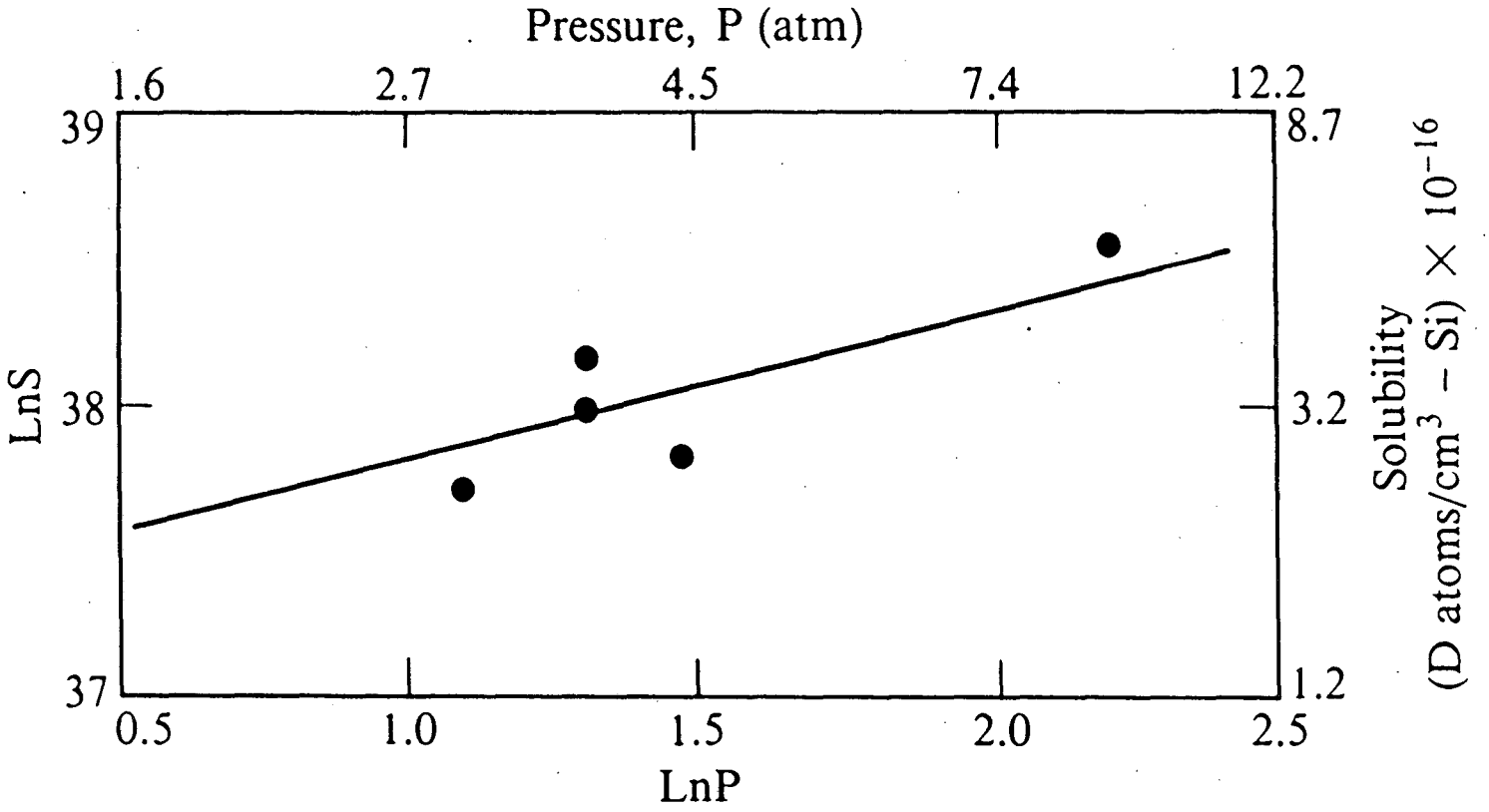


XBL 878-7896

Fig. 4.11. Variation of deuterium solubility in crystalline Si with pressure. The infusion period was one hour at 1450 K of temperature.

argued that the equilibrium position for atomic hydrogen in Si is the tetrahedral interstitial site ($T_d$).

(b) Picraux et al.[66] concluded from their channeling experiments that an implanted deuterium is located at a unique antibonding site, a position at a distance of $1.6 \times 10^{-4} \mu m$ from the Si atom along the [111] axis but opposite to the nearest-neighbor direction.

(c) Using the MNDO (modified neglect of diatomic overlap) method, Corbett et al.[67] found that the dangling bonds of Si atoms at defects sites act as a sink for atomic hydrogen forming Si-H bonds.

The pressure to the one-half power dependence of hydrogen solubility in silicon derived above was also discussed by Wieringen et al.[63] in connection with their permeation results. Thus Sievert's law is obeyed in the dissolution of deuterium in single crystal silicon:

$$\tfrac{1}{2}D_2 \underset{\rightarrow}{\overset{K_s}{}} D(sol'n) \tag{4.3}$$

where

$$K_s = S / \sqrt{P_{D_2}} = K_{so} e^{\left(-\frac{E_s}{RT}\right)}, \tag{4.4}$$

| Temp. (K) | $10^3 / T$ ($K^{-1}$) | $K_s \times 10^{-16}$ |
|---|---|---|
| 1360 | 0.735 | 0.45 |
| 1430 | 0.700 | 1.07 |
| 1450 | 0.690 | 0.93 |
| 1470 | 0.680 | 1.47 |

Table 4.5. Temperature dependent solubility measurements. $K_s$ is calculated from Eq. (4.4) and has units of atoms $cm^{-3}$ $atm^{-1/2}$.

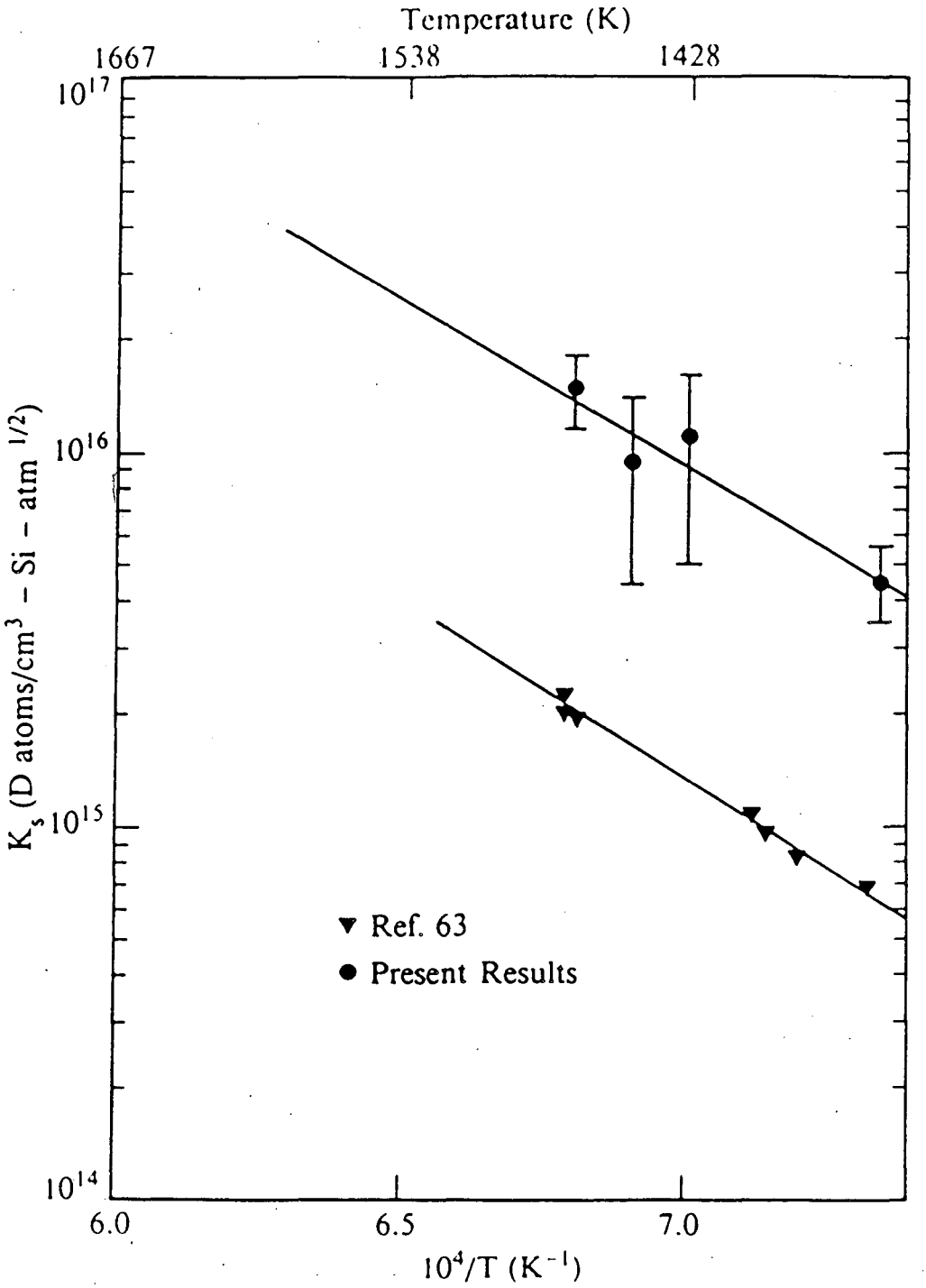


Fig. 4.12. Arrhenius plot of the Sievert's constant, $K_s$, for deuterium solubility in monocrystalline silicon. The present results (shaded circles) are plotted together with results of Ref. 63 (shaded triangles) and regression lines are drawn through the points.

$K_s$ is the equilibrium constant; P the pressure in atmospheres; $E_s$ the heat of solution; and R the gas constant. Sievert's constants ($K_s$) are given in the last column of Table 4.4.

Table 4.5 gives $K_s$ at various temperatures. Arrhenius plot of the data in this table is shown in fig. 4.12. Also plotted in this figure are the results of Wieringen and Warmoltz[63] for comparison. A regression line fit to the present results gives $E_s$ of 40 kcal mol$^{-1}$. This is in close agreement with what was calculated by Corbett et al.[67], 38 kcal mole$^{-1}$ and the experimental results of 43 kcal mole$^{-1}$ estimated by Wieringen and Warmoltz. Hydrogen solubility in crystalline silicon increases with increasing temperature, making silicon an endothermic absorber. The preexponential factor, $K_{so}$, obtained from fig. 4.12 is $1.21 \times 10^{22}$. Wieringen et al. calculated $K_{so}$ value of $2.4 \times 10^{21}$, which is a factor of 5 lower than the above value. This is expected given the differences in the methodology as well as sample characteristics (purity and lattice defect concentration) in the two measurements. It has been reported by Pankove et al.[111] and Johnson et al.[102] that substitutional doping of Si greatly influenced its hydrogen solubility. Since the samples used in this experiment and that of Wieringen's are completely different in their doping concentrations and structural defects the two solubilities are bound to differ. Furthermore, the solubility deduced from the permeation results is predicated on accurate measurement of the diffusion coefficient, D. Thus any uncertainty in the D measurement will be manifested in the solubility calculations.

The multiple peaks exhibited in the deuterium release-rate curves (Fig. 4.10) is indictive of trapping of deuterium at specific sites in the crystalline silicon. To ascertain the binding energies associated with each site the kinetics of the release of the dissolved deuterium are analyzed using the detrapping technique similar to what is used in thermal desorption spectroscopy experiments[68–71], assuming that

diffusion through the lattice after detrapping is fast. The latter assumption was proven by a preliminary analysis of a release model based solely on deuterium diffusion through the Si lattice. A diffusion coefficient (Eq. 4.15) measured by Wieringen et al.[63] was used in the model. The diffusion model generated a spectrum (shown as a dotted curve in Fig. 4.13) which predicts a temperature of maximum-release lower than the temperatures of maximum-release of the three peaks. This indicates a much faster release of deuterium from the Si by a diffusion process than by detrapping from binding sites. The detrapping rate from the various sites is given by the equation:

$$-\frac{dC}{dt} = \nu C^m e^{\left(-\frac{E_d}{RT}\right)} \tag{4.6}$$

where m is the reaction order; $\nu$ the frequency factor; C the bulk concentration at the site; and $E_d$ the activation energy associated with the site. For a linear heating rate ($\beta'$), the detrapping rate reaches a maximum value at a temperature, $T_M$, where

$$\frac{d^2C}{dt^2} = 0$$

Using this condition and Eq. 4.6 a correlation among $T_M$, $\beta'$ and $E_d$ has been derived as:

$$\ln\frac{T_M^2}{\beta'} = \frac{E_d}{RT_M} + \ln\frac{E_d}{m\nu RC_M^{m-1}} \tag{4.7}$$

where $C_M$ is the hydrogen atoms dissolved at $T_M$. For first order kinetics (m = 1) Eq. 4.7 reduces to;

$$\ln\frac{T_M^2}{\beta'} = \frac{E_d}{RT_M} + \ln\frac{E_d}{\nu R} \tag{4.8}$$

Each deuterium release-rate curve is analyzed by decomposing the spectrum into three separate peaks while conserving the total area (i.e. solubility). In the computation, $E_d$ is guessed for each peak and knowing $T_M$ and $\beta'$, $\nu$ is calculated using

Eq. 4.8. Equation 4.6 is numerically integrated for C(t) after substitution of the frequency, $\nu$, computed from Eq. (4.8) and replacing **dt** by $dT/\beta'$. The computation process is repeated several times for various $E_d$ until the theoretical C(t) is comparable to the corresponding experimental data, using least squares approximation technique. A curve of one of the computations is shown in fig. 4.13 and the values of $\nu$ and $E_d$ for the peaks are shown in table 4.6.

The $E_d$ values are the binding energies of H atoms at the three different sites depicted by the release curves. In comparison with the various sites reported in the literature and discussed earlier in this section, the first peak with a binding energy of $0.6 \pm 0.06$ eV agrees well with the M site (potential energy = 0.6 eV), concluded by Corbett et al.[67] to be the potentially minimum site for atomic hydrogen in Si. The most populated site represented by the second peak has a binding energy of

| Infusion | Infusion | Solubility | Pk1 | Pk2 | Pk3 |
|---|---|---|---|---|---|
| Press. | Temp. (K) | $x10^{-16}$ | $\nu$, $E_1$ | $\nu$, $E_2$ | $\nu$, $E_3$ |
| 1.7 | 1470 | 2.50 | 13.8, 12.0 | 524, 25.5 | 7.98E5, 46.6 |
| 3.7 | 1430 | 0.85 | 35.0, 14.0 | 733, 26.6 | 5.03E5, 42.4 |
| 3.0 | 1450 | 0.91 | 14.0, 13.3 | 8300, 31.3 | 1.20E6, 49.3 |
| 3.7 | 1430 | 0.61 | 11.0, 14.7 | 220, 28.1 | 3.00E5, 46.0 |
| 7.1 | 1470 | 3.40 | 15.0, 14.5 | 440, 26.4 | 9.00E5, 48.3 |
| 9.2 | 1360 | 1.30 | 13.6, 12.5 | 1660, 28.0 | 5.10E5, 45.2 |
| 9.2 | 1450 | 5.50 | 10.3, 16.3 | 470, 26.5 | 5.00E5, 45.2 |

Table 4.6. The calculated values of the binding energies at the three sites that corresponds to the three peaks and their pre-exponential factors. The energies are in kcal/mole and the units of the preexponentials and solubilities are $sec^{-1}$ and atoms $cm^{-3}$, respectively. The unit of pressure is atm.

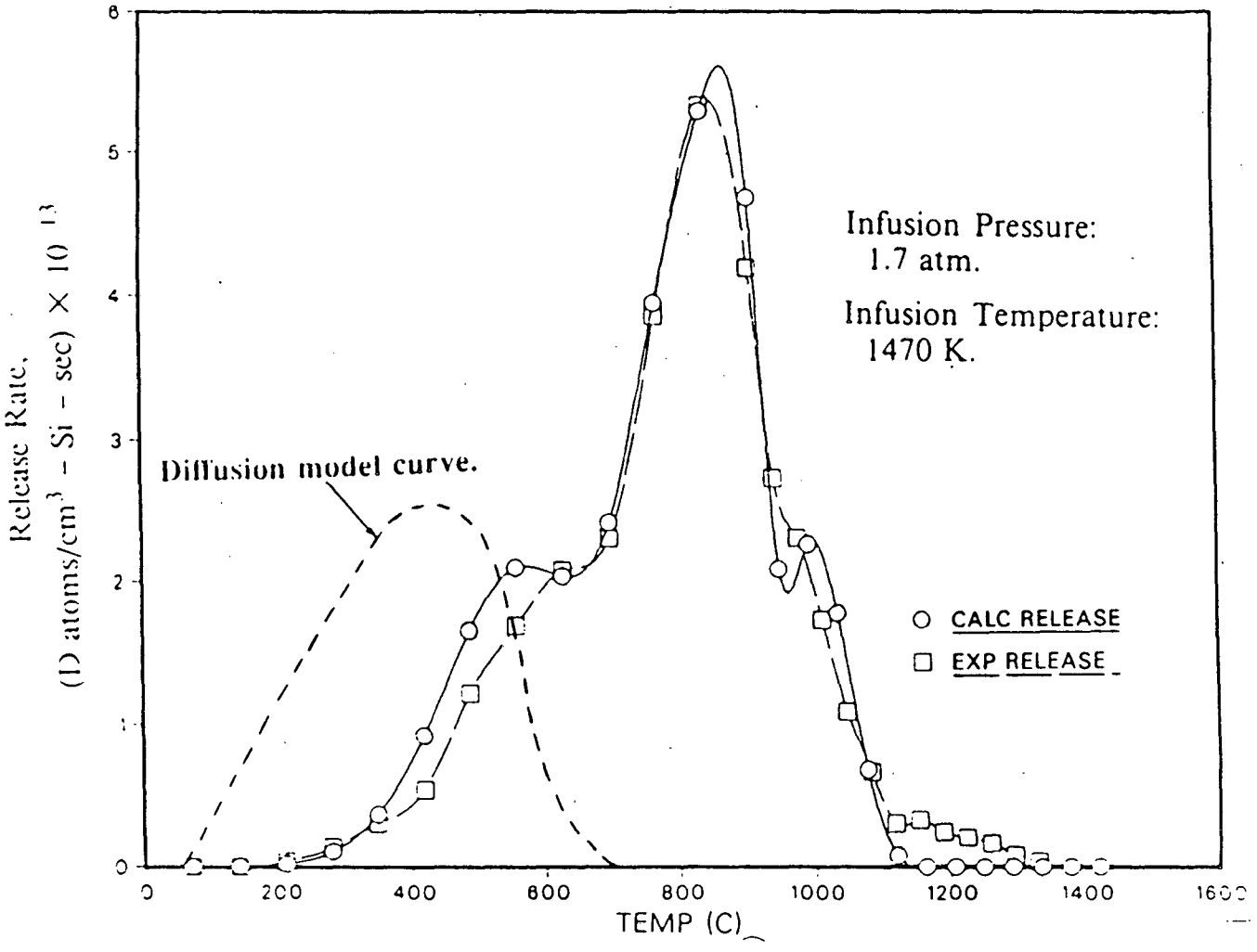


Fig. 4.13. Measured and calculated deuterium release rate curves. A first order kinetics is assumed for each peak in the analysis and two heating rates; $\beta'_1 = 0.93$ K/sec and $\beta'_2 = 0.47$ K/sec are substituted in the calculations as shown in fig. 4.10. The dashed curve is the release spectrum for a diffusion model.

$1.2 \pm 0.07$ eV. This peak could be either the tetrahedral interstitial site ($T_d$) discussed by Sing et al.[65] or the antibonding site of Picraux et al.[66] and Johnson et al.[102] who calculated a binding energy of $\approx 1$ eV for this site. The tightly bound H in the silicon lattice, represented by the third peak with a binding energy of $2.0 \pm 0.1$ eV is either the Si-H complex formed by the saturation of the dangling bonds of Si atoms at defects sites or more likely the stable $H_2$ in the interstitial position of the Si lattice reported by Mainwood and Stoneham[72] and discussed by Corbett et al.[67]. The calculated binding energy for $H_2$ in this site in Ref. 72 is $\approx 2$ eV which agrees well with the present estimate for the third peak. The rate constants of the outgassing kinetics for each peak are plotted in fig. 4.14. The above results then resolves the site problem for hydrogen in the Si lattice and clearly defines certain specific sites that have already been predicted by theoretical calculations. Molecular hydrogen in Si might be formed at the point defect sites where the dangling bonds act as recombination centers. However, this process apparently does not occur during the small time scale (ms) of the molecular beam experiments.

Other than the qualitative conclusion that part of the atomic hydrogen in the molecular beam experiment dissolves in the silicon substrate, the solubility measurements by themselves do not justify the inclusion of the bulk solution-diffusion step in the modulated molecular reaction model. This is because the energetics of atomic hydrogen dissolution from the atomic beam are different from that of direct solution starting with molecular hydrogen. The sticking probabilities of monatomic and molecular hydrogen are completely different, so solution of the $H_2$ portion of the incident flux is negligible in the molecular beam experiments. The sticking probability of H on Si is close to unity but that of $H_2$ is $\approx 10^{-5}$[73,74] However, the rate

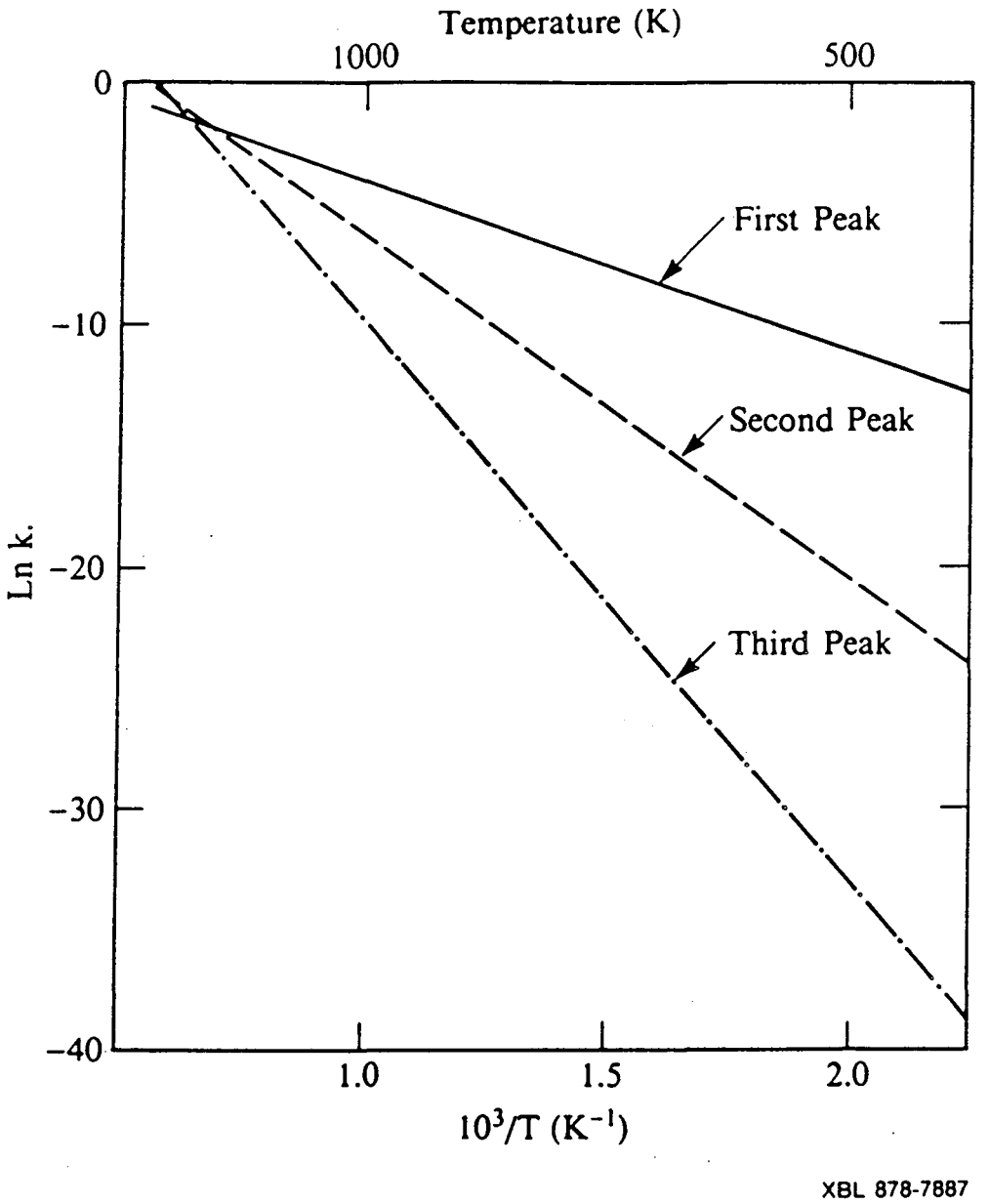


Fig. 4.14. The computed rate constants of the three peaks from the release kinetics analysis of the deuterium desorption spectra.

constant expression $\frac{1}{2}h^2D$, obtained from the modulated molecular beam analysis could be estimated independently using the solubility results and known value of the diffusion coefficient, D.

The reaction steps that lead to dissolution of $H_2$ in bulk silicon are:

$$\tfrac{1}{2}H_2 \xrightarrow{K_E} H(ads) \xrightarrow{h} H(sol'n) \tag{4.9}$$

From the above equation:

$$K_E = \frac{[H(ads)]}{\sqrt{P_{H_2}}} \tag{4.10}$$

$$h = \frac{[H(sol'n)]}{[H(ads)]} \tag{4.11}$$

so

$$K_s = \frac{[H(sol'n)]}{\sqrt{P_{H_2}}} = K_E h \tag{4.12}$$

where $K_E$ is the equilibrium constant for dissociative adsorption of hydrogen on silicon; **h** the solubility coefficient from the adsorbed state; and $K_s$ the Sievert's constant. A simplified potential energy diagram of Si/H system is shown in fig. 4.15. The binding energy, $E_a$, is the strength of the Si-H bond, or 75 kcal/mole; the heat of solution, $E_s$ = 40 kcal/mole; the heat of adsorption, $\Delta H_a = E_a - \frac{1}{2}B$ = 22 kcal/mole assuming no activation barrier to the surface adsorption; the dissociation energy of hydrogen, $\frac{1}{2}B$ = 53 kcal/mole; and the activation energy for diffusion, $E_D$ = 11 kcal/mole. Thus from the potential energy diagram $K_E$ has an activation energy of 22 kcal/mole and the preexponential is approximately equal to the product of the sticking probability of $H_2$, $\eta_2$, and the vibrational frequency, $\nu$, in the potential well, i.e.

$$K_E = \eta_2 \nu \exp\left(-\frac{22}{RT}\right) \tag{4.13}$$

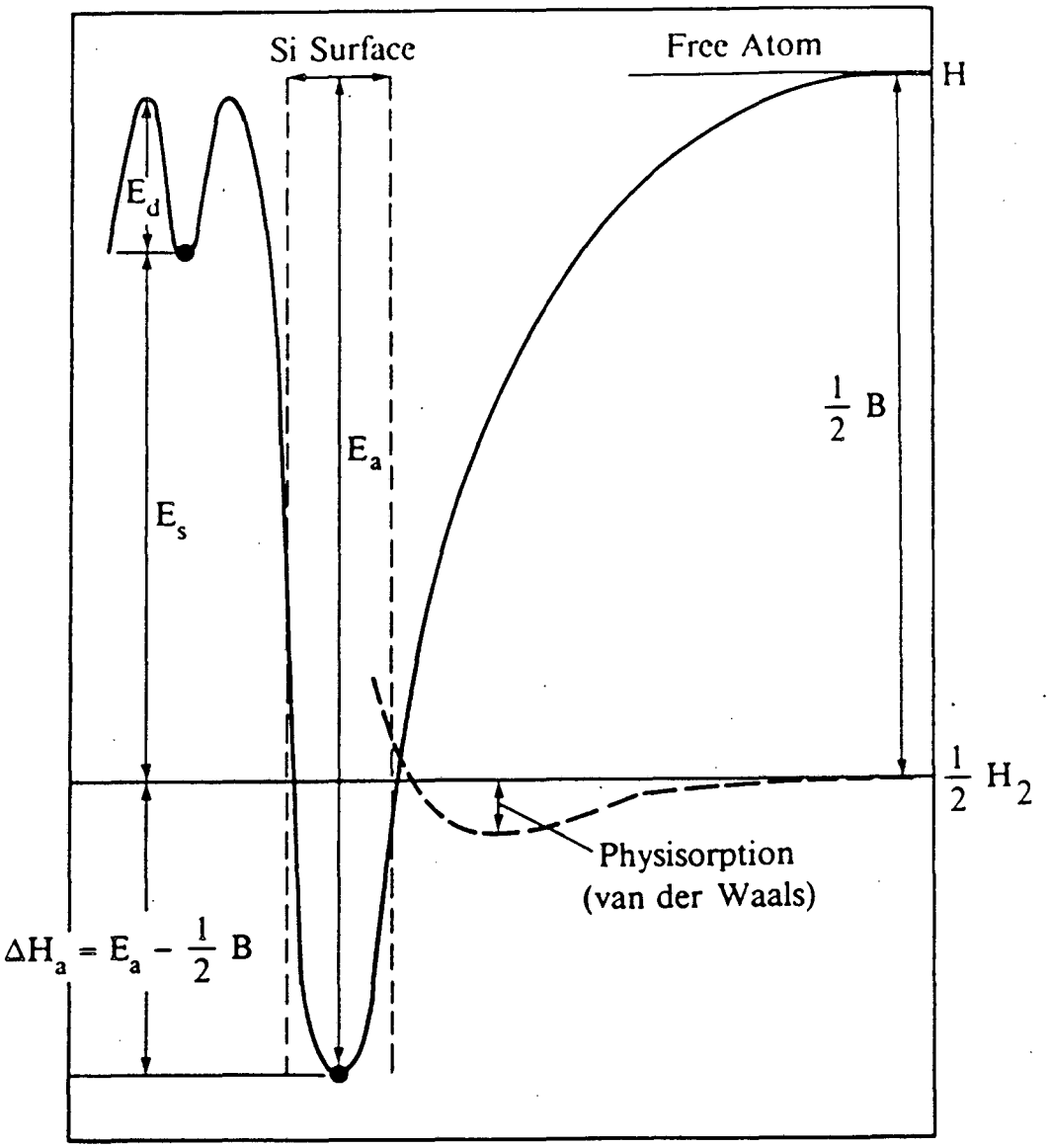


XBL 878-7891

Fig. 4.15. A potential energy diagram of Si/H system. The ordinate represents potential energy and the abscissa is the atomic spacing.

The sticking probability has been measured by Law and Francois[74] and Brzoska et al.[73] to be $\approx 10^{-5}$ and the vibration frequency of physisorbed $H_2$ is, $\nu \approx 10^{13}$. From Eq. 4.12, the estimated $K_E$ and the measured $K_s$, **h** is estimated as:

$$h = 1.2 \times 10^{14} \exp\left(-\frac{18}{RT}\right) \tag{4.14}$$

The diffusion coefficient, D, is given in Ref. 63 in the same temperature range as:

$$D = 9.5 \times 10^{-3} \exp\left(-\frac{11}{RT}\right) \tag{4.15}$$

Eqs. 4.14 & 4.15 gives;

$$\tfrac{1}{2}h^2D = 7.0 \times 10^{25} \exp\left(-\frac{47}{RT}\right) \tag{4.16}$$

Extrapolation of this rate constant to the low temperature range where the molecular beam data were measured gives $\tfrac{1}{2}h^2D$ values at 350 K, 400 K and 500 K of $3.1 \times 10^{-4}$ $sec^{-1}$, 1.5 $sec^{-1}$ and $2.0 \times 10^{5}$ $sec^{-1}$, respectively. These estimated values are large enough to justify the inclusion of bulk solution-diffusion step in the reaction model.

# 5. REACTION MECHANISM

## 5.1. General Features

The most notable features of the modulated molecular beam results at temperatures below that for surface structuring are the following;

### 5.1.1. Responses of $\varepsilon$ and $\Phi$ to Temperature Changes Below the Transition Temperature

The effect of increasing temperature on reaction probability (Figs. 4.4 & 4.5) is consistent with the results reported by Webb et al.[22] and Veprek et al.[23], who observed a decrease in the reaction of hydrogen plasma with Si(111) with increasing temperature in the temperature range of 283 K and 813 K. The challenge is to determine what could cause a decrease in $SiH_4$ production and at the same time increase the phase lag with increasing temperature. The most likely explanation is a mechanism containing processes competing with $SiH_4$ production, namely heterogeneous recombination and bulk solution diffusion of the surface adsorbed H atoms. These processes increase more rapidly with temperature than does the etching reaction, thereby reducing the rate of the latter as temperature increases.

### 5.1.2. Small Phase Lags

The small phase lags measured in this experiment, are an indication of a fast surface reaction. For example, at ambient temperature and a frequency of 46Hz, a $5^0$ phase lag was measured. This corresponds to overall reaction time of 0.3 ms. To complement this results, complete waveforms of the signal outputs were taken with a multi-channel analyzer. The waveforms at a modulation frequency of 20 Hz and 0.3 Torr $H_2$ source pressure are shown in figs. 5.1 - 5.3. Except for greater noise, the product waveform is almost identical in shape to that of the scattered H waveform. The frequency effect on the apparent reaction probability and phase lag

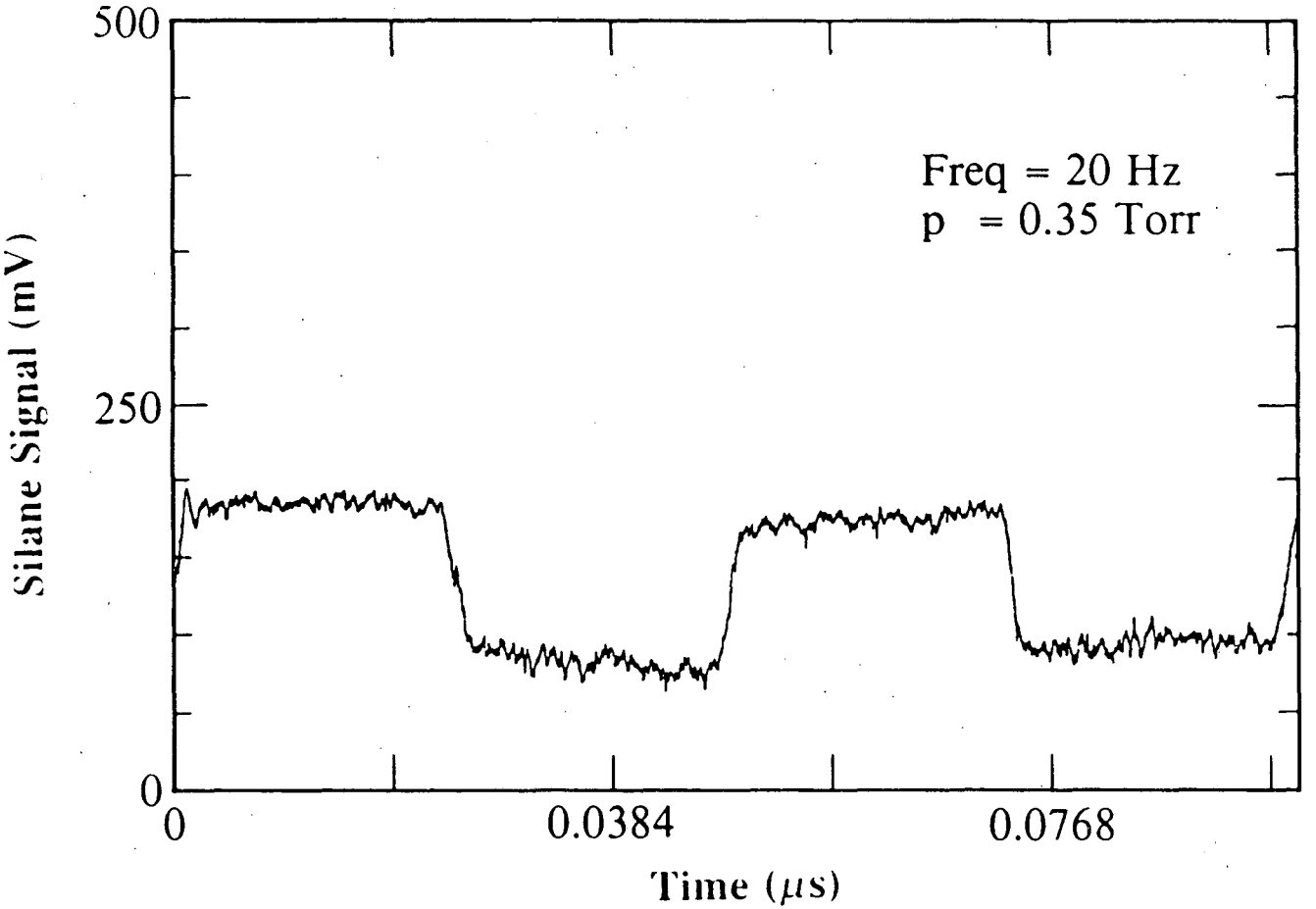


XBL 878-7894

Fig. 5.1. Silane product waveform

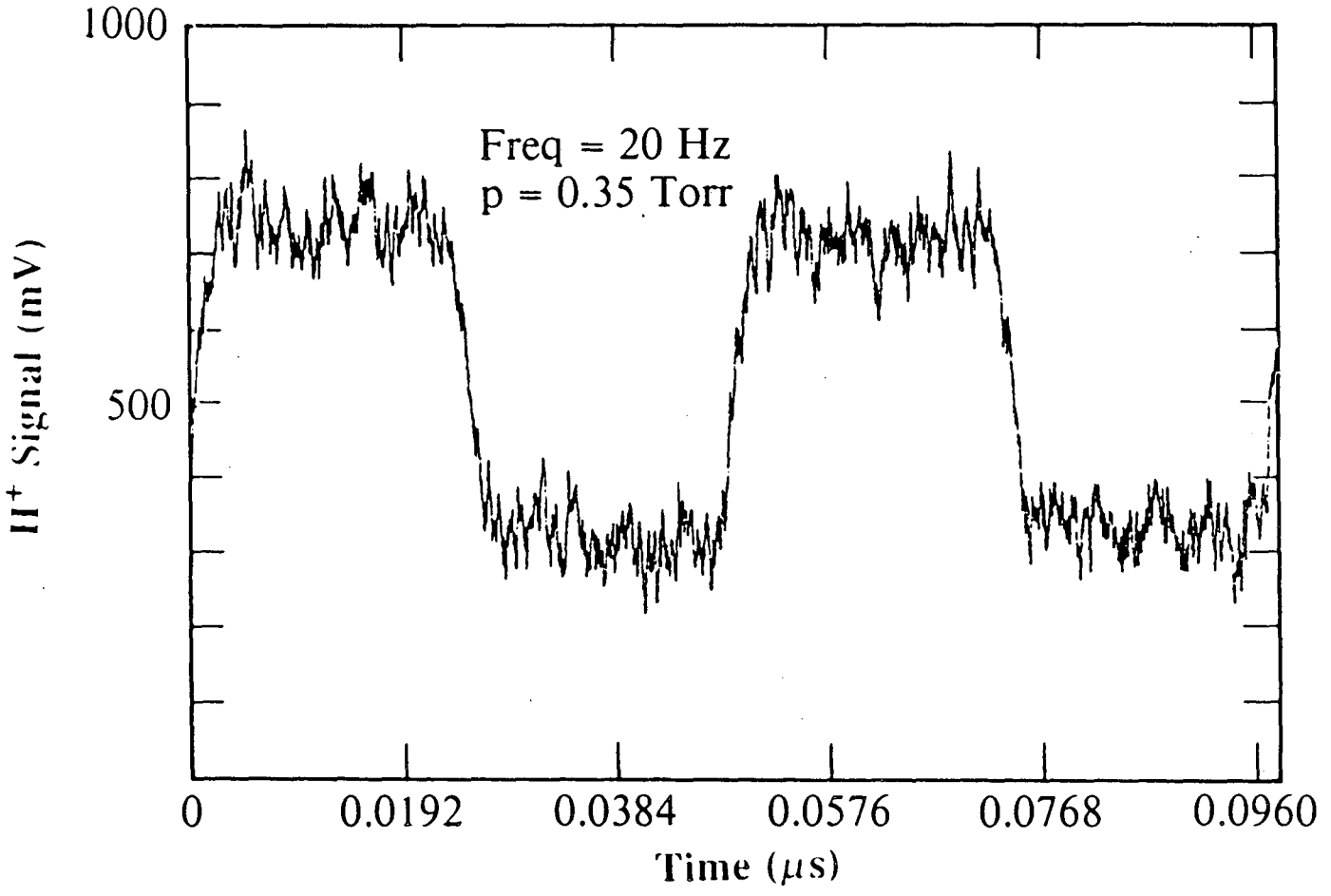


XBL 878-7892

Fig. 5.2. Scattered atomic hydrogen waveform

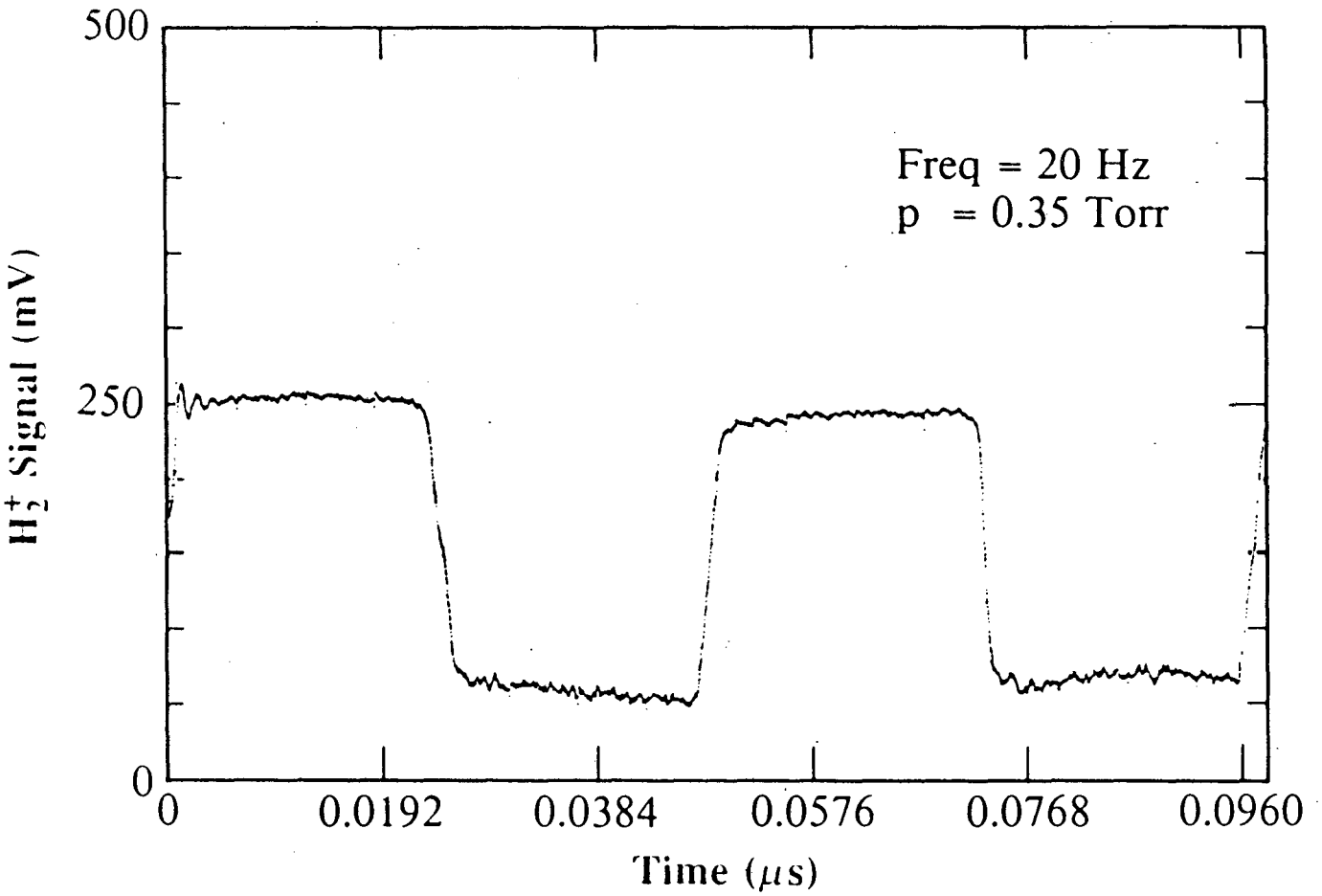


XBL 878-7893

Fig. 5.3. Scattered and recombined molecular hydrogen wavefom

(fig. 4.7) is minor, which is further proof of a fast surface reaction.

### 5.1.3. Reaction Order

Figures 4.11 and 4.12 show reaction probability and phase lag to be independent of atomic hydrogen beam intensity. The etch rate of Si(111) in a hydrogen plasma was also observed by Veprek and Sarrott[23] to be linearly dependent on the hydrogen pressure. This is indicative of first-order surface reaction, which eliminates any non-linearity in the reaction mechanism.

## 5.2. Reaction Model

The model that best fits the experimental data was developed from the concepts of thermal desorption spectroscopy (TDS)[91], an electron energy loss (EELS)[92], infra-red spectroscopy (IRS)[93,94] and the present molecular beam results.

### 5.2.1. Saturation of Dangling Bonds

Two distinct sites for binding of atomic hydrogen on Si(111)-7x7 have been described[91–94]. The primary sink is the dangling bonds of the uppermost layer of surface atoms, designated as $\beta_1$ state of surface hydrogen. Only when these are $\approx 50\%$ saturated can the second ($\beta_2$) state of hydrogen begin to be occupied[91]. These two states are quite stable and desorb as $H_2$ only at temperatures of $\approx 700\,K$ ($\beta_2$ state) and $\approx 825\,K$ ($\beta_1$ state)[91]. The TDS result of Ref. 91 is shown in fig. 5.4. Schulze and Henzler analyzed the $\beta_1$ state by a second order desorption kinetics for low coverages, but noticed that with increasing coverage ($\theta \approx 1$), the temperature of maximum desorption remained constant. Thus indicating a shift to first-order kinetics. So at higher coverages they fitted the $\beta_1$ state with both a first-order and a second order rate constants listed in Table 5.1. The $\beta_2$ state was fitted with a first-order kinetics which yielded a rate constant of activation energy of

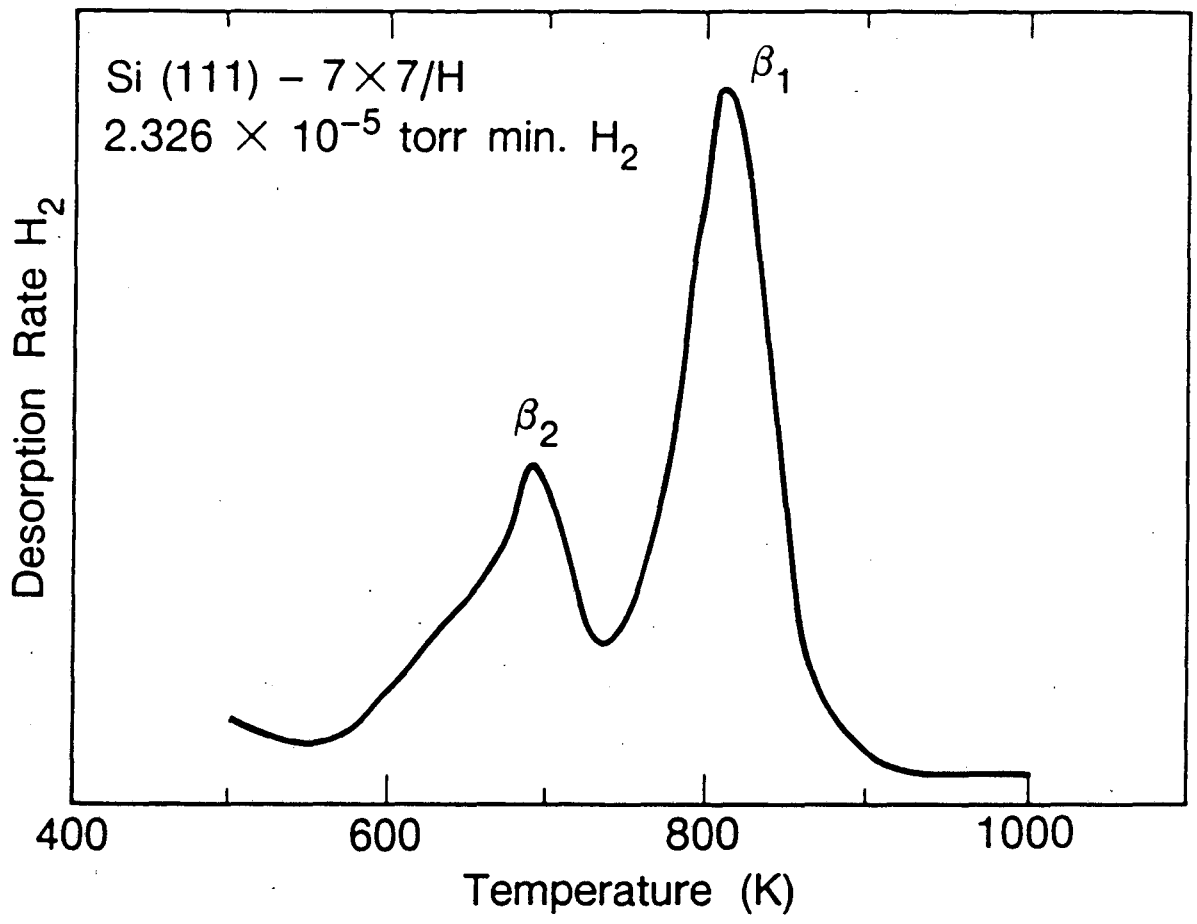


XBL 872-7587

Fig. 5.4. A thermal desorption curve from a saturated coverage of a cleaved annealed Si(111) at a heating rate of 6.6 K/sec after H exposure for a minute. Two binding states ($\beta_1$ and $\beta_2$) are indicated[91].

44 ± 7 kcal/mole.

| Reaction | Rate Constant |
|---|---|
| First-order kinetics | $k_d = 9.7 \times 10^{12} \exp(-48.3/RT)$ $sec^{-1}$ |
| Second-order kinetics | $k_d = 1 \times 10^{8} \exp(-80.5/RT)$ $cm^2 sec^{-1}$ |

Table 5.1. The rate constants of $\beta_1$ state from the TDS spectrum of Fig. 5.4.

As shown in section 6.1, these states are saturated during the molecular beam experiments at temperatures below 600 K, where substantial $SiH_4$ production is observed (fig. 4.4). Moreover, the very fact that TDS, EELS and IRS studies could be conducted after the supply of atomic hydrogen to the surface had been shut off shows that the bound states of hydrogen do not react with the substrate to form $SiH_4$ at low temperatures; a continuous supply of gas-phase H atoms is required to accomplish this. The most likely mechanism, however, involves the existence of a third type of surface hydrogen, weakly-bound and sustained only by virtue of the constant supply from the atomic H beam.

### 5.2.2. Bulk Solution-Diffusion

The sluggish response of the phase lag to temperature changes at high temperatures (fig. 4.5), is indicative of bulk diffusion, most probably of atomic hydrogen arising from the weakly-bound H atoms. Chabal et al.[94] suggested that small amounts of hydrogen diffuse below the outermost silicon layer and this process has been a subject under study in the silicon industry[95–104]. From the present hydrogen solubility measurements and the data of Ref. (63), silicon is an endothermic absorber (i.e. the solubility increases with increasing temperature). In modeling this effect, a lattice migration of H atoms with a diffusion coefficient D is used. An equilibrium is assumed between the weakly-bound adsorbed H atom state and the

hydrogen in the bulk just beneath the surface.

### 5.2.3. Surface Recombination

Recombination of the weakly-bound adlayer to form $H_2$ could occur by reaction of two of these species or by reaction of one with another H atom of the tightly bound layers. The absence of non-linearity in the experimental results suggests the latter to be the most likely recombination reaction, since the concentrations of the $\beta_1$ and $\beta_2$ sites are saturated and only the weakly-bound surface H concentration varies during a modulation cycle.

### 5.2.4. Silane Production

The low-temperature gasification of Si was initially considered to be via an Ely-Rideal step whereby an impinging H atom directly reacts with an $SiH_3$ complex to form volatile $SiH_4$:

$$SiH_3(ads) + H(g) \xrightarrow{\sigma} SiH_4(g)$$

Such a model could explain the fast surface reaction (small phase lags even at room temperature). This step is characterized by a reaction cross-section, $\sigma$ (a measure of the probability that an incident H-atom will strike an $SiH_3$ complex on the surface). An expected value of $\sigma$ is of the order of $\pi a_0^2$; where $a_0$ is the Si-Si atomic spacing, 3–5 A, or $\sigma \leq 10^{-14}\,cm^2$. However, the theoretical fitting curve to the experimental data gave a $\sigma \approx 10^{-10}\,cm^2$. This value of $\sigma$ is difficult to justify for a direct-collision surface process, so the mechanism was rejected. However, the weakly-bound surface hydrogen is mobile and can react with the $SiH_2$ complex to eventually produce $SiH_4$. The possibility of this process occurring was first suggested by Wagner et al.[92]. Cutting off the atomic hydrogen supply to the surface from the beam results in rapid depletion of the weakly-bound hydrogen (through either $H_2$ or $SiH_4$ formation), leaving behind the tightly-bound forms which are observed

in the TDS, EELS and IRS experiments.

The decrease in $SiH_4$ reaction probability with increasing temperature is ascribed to the decrease in concentration of $SiH_2$ complex on the Si surface. This is inferred from the EELS data reported by Wagner et al.[92] in which the ratio of the loss peak representing the Si-H stretching mode to that of the $SiH_2$ scissor mode increases with increasing temperature. This observation can be interpreted as the effect of temperature on the following equilibrium;

$$2SiH = SiH_2 + Si(s) \tag{5.1}$$

where SiH represents the strongly-bound surface hydrogen. For modeling purposes, no distinction is made between the $\beta_1$ and $\beta_2$ states. If $\Gamma$ denotes the fraction of the chemisorbed hydrogen present as $SiH_2$ complex, $1-\Gamma$ is the fraction present as SiH, because the surface remains saturated with hydrogen at the temperatures and hydrogen beam intensities of interest. The law of mass action for reaction (5.1) is:

$$\frac{\Gamma}{(1-\Gamma)^2} = K$$

If $\Gamma << 1$, this equation simplifies to:

$$\Gamma \approx K = \Gamma_0 \exp(-\Delta H/RT) \tag{5.2}$$

where $\Delta H$ is the enthalpy change of reaction (5.1) and $\Gamma_0$ is a constant. Since the EELS data show that $\Gamma$ decreases with increasing temperature, $\Delta H$ is negative, or the $SiH_2$ complex is energetically more stable than hydrogen bound individually to two silicon atoms as the SiH species. $\Delta H$ is estimated from the EELS results of Wagner et al.[92] (fig. 5.5) in the following way: The surface concentrations of SiH and $SiH_2$ are assumed to be proportional to the intensities at 630 $cm^{-1}$ (associated with bond-bending) for SiH and 900 $cm^{-1}$, the scissor mode, for $SiH_2$. The intensities of these two peaks at various temperatures from fig. 5.5 are listed in Table 5.2.

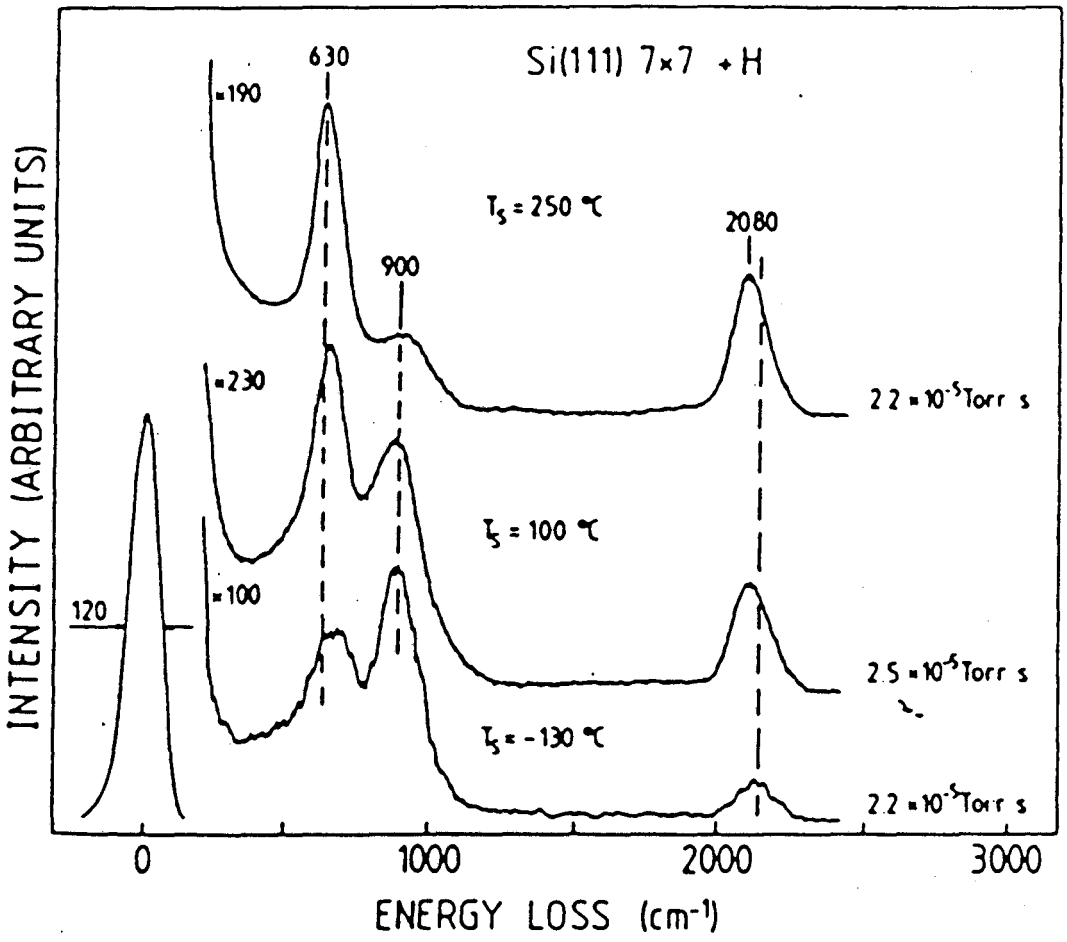


Fig. 5.5. High resolution electron energy loss spectra after hydrogen adsorption on Si(111)-7x7 surface at three different substrate temperatures[92].

The units of the intensities are arbitrary because the constants of proportionality between intensities and surface concentrations are probably different for each peak. An estimated $\Delta H$ for $\Gamma$ from the $SiH_2$ data in Table 5.2 is; $\Delta H \approx -0.4$ kcal/mole.

| Temp. (K) | SiH Intensity | $SiH_2$ Intensity |
|---|---|---|
| 143 | 15 | 24 |
| 373 | 29 | 22 |
| 523 | 26 | 6 |

Table 5.2. Intensities (arbitrary units) of EELS peaks of SiH and $SiH_2$ complexes on Si(111)-7x7 at various temperatures.

### 5.2.5. Model

a) Physisorption of weakly-bound H atoms to the surface which is saturated with strongly-bound hydrogen is expressed by:

$$H \xrightarrow{\eta} H(ads.) \tag{5.3}$$

where $\eta$ (sticking probability) is not dependent on temperature or coverage.

b) Surface-subsurface equilibrium of the H adlayer is expressed by the distribution:

$$H(ads) \underset{\rightarrow}{\overset{h}{\leftarrow}} H(sol'n, subsurface) \tag{5.4}$$

where h = the solubility coefficient.

Diffusion in the bulk is denoted by:

$$H(sol'n, subsurface) \underset{\rightarrow}{\overset{D}{\leftarrow}} H(bulk) \tag{5.5}$$

where D is the diffusivity of hydrogen in the Si lattice.

c) Surface recombination proceeds by reaction of a weakly-bound H atom with one in the chemisorbed layer:

$$H(ads) + SiH \xrightarrow{k_{d_2}} Si(s) + H_2(g) \tag{5.6}$$

d) $SiH_4$ production takes place by reaction of physisorbed H with the $SiH_2$ complex:

$$H(ads) + SiH_2 \xrightarrow{k_3} SiH_3 \tag{5.7}$$

followed by,

$$H(ads) + SiH_3 \xrightarrow{fast} SiH_4(g) \tag{5.8}$$

$k_{d_2}$ and $k_3$ are rate constants for the recombination and etching channels, respectively. Equation (5.7) is the rate-limiting step for silane production, but the solution-diffusion process (Eqs. 5.4 and 5.5) and surface recombination (Eq. 5.6) also influence the rate. Note that there is evidence of an $SiH_3$ surface species[114]. As silicon dangling bonds are exposed by surface recombination or by silane production, hydrogen from the beam or from the weakly-bound layer are assumed to immediately refill the vacant sites. In this way, the surface is kept saturated with chemisorbed hydrogen during reaction.

### 5.2.6. Analysis of the Reaction Model

Let n(t) denote the surface concentration of the weakly-bound hydrogen atoms and C(z,t) the bulk concentration of dissolved hydrogen. The bulk concentration of hydrogen just beneath the surface is assumed to be related to the concentration of the adlayer H atoms by the solubility coefficient, **h**. Thus;

$$C(0,t) = hn(t) \tag{5.9}$$

The silicon sample is modeled as semi-infinite medium for one-dimensional transient diffusion:

$$\frac{\partial C}{\partial t} = D \frac{\partial^2 C}{\partial z^2} \tag{5.10}$$

where $z$ is the penetration depth normal to the surface and t is time. The boundary

conditions far from the surface is:

$$C(t,\infty) = \text{finite} \tag{5.11}$$

At z = 0 the surface mass balance on H atoms (physisorbed and chemisorbed) is:

$$\frac{dn}{dt} = \eta\, I_0\, g(t) - 4\, k_3\, \Gamma N_s\, n - 2\, k_{d_2}(1 - \Gamma) N_s\, n + D \left| \frac{\partial C}{\partial z} \right|_{z=0} \tag{5.12}$$

where $I_0$ is the amplitude of the incident atomic hydrogen beam intensity; g(t) is the gating function of the square modulated beam and $N_s$ is the total number of hydrogen binding sites on the Si(111)-7x7 surface. Eq. (5.12) contains no time-derivative of the chemisorbed hydrogen, because this state is assumed to remain filled at all times. The first term on the right hand side of equation (5.12) represents the rate of physical adsorption rate of H atoms per unit area from the incident beam. The second term accounts for H atom loss from the surface by silane production; the third is the loss of H through surface recombination; and the last represents the bulk diffusion effect.

The exact solution of Eqs. 5.9 - 5.12, could be obtained by a numerical solution, but the approximate method discussed by Olander et al.[105] is used in the analysis of this model. Even though the technique is an approximation, the accuracy is well within the precision of the experimental data and thus offers a strong incentive for its use instead of the more laborious numerical procedure. By following the procedure outlined in Ref. 105, the beam gating function is expanded in abbreviated Fourier series:

$$g(t) = \frac{1}{2}\left(1 + g_1\, e^{i\omega t}\right) \tag{5.13}$$

where $\omega = 2\pi f$ is the modulation frequency in radians sec.$^{-1}$ and $g_1 = 4/\pi$ for the incident square-modulated wave. The bulk and surface concentrations are similarly expressed:

$$C(z,t) = C_0 + \bar{C}(z)\, e^{i\omega t} \tag{5.14}$$

and

$$n = n_0 + \bar{n}\, e^{i\omega t} \tag{5.15}$$

where $n_0$ and $C_0$ are the steady state components and $\bar{n}$ and $\bar{C}$ are the first Fourier components. Substituting Eq. 5.14 into Eq. 5.10 and solving the resulting ordinary differential equation gives:

$$D \left| \frac{\partial C}{\partial z} \right|_{z=0} = -(i\omega h^2 D)^{1/2} \bar{n} e^{i\omega t} \tag{5.16}$$

where the condition of Eq. 5.11 has been used. Equations 5.13, 5.15 and 5.16 are substituted into Eq. 5.12 to yield

$$i\omega \bar{n}\, e^{i\omega t} = \eta \frac{I_0}{2} \left(1 + g_1 e^{i\omega t}\right) - \left(4k'_3 + 2k'_{d_2}\right) \left(n_0 + \bar{n}\, e^{i\omega t}\right) - \sqrt{i\omega h^2 D}\, \bar{n} e^{i\omega t}. \tag{5.17}$$

where,

$$k'_3 = k_3 \Gamma N_s \tag{5.18}$$

$$k'_{d_2} = k_{d_2} (1 - \Gamma) N_s \approx k_{d_2} N_s \tag{5.19}$$

are modified rate constants with Arrhenius-type behavior:

$$k'_3 = k'_{30} \exp(-E'_3/RT) = k_{30} \Gamma_0 N_s \exp\left(-\frac{E_3 + \Delta H}{RT}\right) \tag{5.20}$$

$$k'_{d_2} = k'_{d_0} \exp(-E'_2/RT) \tag{5.21}$$

Equating the coefficients of the zeroth and first powers of $e^{i\omega t}$ in Eq. 5.17 gives the following solutions:

$$\bar{n} = \frac{\frac{1}{2}\eta\, I_0\, g_1}{A + iB} \tag{5.22}$$

where;

$$A = 4\, k'_3 + 2\, k'_{d_2} + \sqrt{\tfrac{1}{2}\omega\, h^2\, D} \tag{5.23}$$

$$B = \omega + \sqrt{\tfrac{1}{2}\omega\, h^2 D} \tag{5.24}$$

and,

$$n_0 = \frac{\eta\, I_0}{4k'_3 + 2k'_{d_2}} \tag{5.25}$$

The reaction product vector for silane production is defined as;

$$\varepsilon_4 e^{-i\Phi_4} = \frac{4\, k'_3\, \bar{n}}{\tfrac{1}{2} I_0\, g_1} \tag{5.26}$$

Similarly, the reaction product vector for the recombination of surface adsorbed H atoms is:

$$\varepsilon_2 e^{-i\Phi_2} = \frac{2\, k'_{d_2}\, \bar{n}}{\tfrac{1}{2} I_0\, g_1} \tag{5.27}$$

Equations 5.26 and 5.27 are solved for $\varepsilon_4$, $\varepsilon_2$, $\Phi_4$ and $\Phi_2$.

Substitution of Eq. 5.22 into Eqs 5.26 and 5.27 yields:

$$\varepsilon_4 = \frac{4\, k'_3\, \eta}{\sqrt{A^2 + B^2}} \tag{5.28}$$

$$\varepsilon_2 = \frac{2k'_{d_2}\eta}{\sqrt{A^2 + B^2}} \tag{5.29}$$

Since the recombination and silane production reactions are linearly dependent on the adlayer surface concentration, the theoretical analysis yields the same phase lag for the two processes;

$$\Phi_2 = \Phi_4 = \tan^{-1}\left(\frac{B}{A}\right) \tag{5.30}$$

These last three equations are used to predict $\varepsilon_4$, $\varepsilon_2$ and $\Phi_4$ as functions of the three experimental variables, T, $I_0$ and $\omega$, for comparison with the experimental data. Four explicit fitting parameters are contained in this model; $\eta$, $k'_3$, $k'_{d_2}$ and $h^2D$. The last three are made up of two constants (pre-exponential factor and activation energy) and thus seven constants are to be determined by the fitting technique. For-

tunately, the curve fitting could be done sequentially due to the large quantity of data that were taken. The first step was the determination of $\eta$ from the experimental data analysis. Using Eq. 4.1 and the signal ratios H to $H_2$ of the primary beam and the reflected beam, $\eta$ was estimated for each test as shown in the tables of section 4.2.2 which gives the best estimate of $\varepsilon_2$. The next step was the fitting of the ambient temperature data only. This reduces the system to four explicit parameters, namely $\eta$ and the 350 K values of $k'_3$, $k'_{d_2}$ and $h^2D$. The last step consisted of fitting the higher temperature data to obtain the activation energies and the corresponding pre-exponential factors.

| Reaction | Rate Constant |
|---|---|
| Sticking of H | $\eta = 0.7 \pm 0.1$ |
| Bulk Solution Diffusion | $\frac{1}{2}h^2D = 7.3 \times 10^{12} \exp(-14.3/RT)$ |
| Surface Recombination | $k'_{d_2} = 6.2 \times 10^6 \exp(-4.5/RT)$ |
| Silane Production | $k'_3 = 2.7 \times 10^3 \exp(-1.8/RT)$ |

Table 5.3. The rate constants in the proposed mechanism obtained from the curve fitting proceedure. The activation energies are in kcal/mole.

The data fitting was performed with the subroutine LMDIF from the MINPACK library which minimizes the sum of the squares of the deviations in $\Phi$ (in radians) and natural logarithm of $\varepsilon$. The numerical values of $\Phi$ in radians were a factor of 10 lower than the natural logarithm of $\varepsilon$ so the deviations in $\Phi$ were weighted by a factor of 10 in the computations in order to make the deviations in both parameters of the same magnitude. The parameters obtained from this minimization technique are shown in Table 5.3. Theoretical curves of $\varepsilon$ and $\Phi$ from these parameters are shown in figs. 5.6 - 5.9. Arrhenius plots of the rate constants are shown in fig. 5.10.

With the exception of the high temperature phase lag data, there is good agreement between the model and the experimental results. The discrepancy at high temperatures might be caused by two main effects:

(a) Small signals reduce the experimental accuracy of the measurements, where the small product signal was shrouded in the background noise at high temperatures.

(b) Thermal desorption from the strongly-bound H has the effect (not contained in the model) of reducing the SiH and $SiH_2$ concentrations and consequently the rate of $SiH_4$ production. This effect is illustrated in figs. 5.6, 5.7 & 5.9b, where model predicts too high reaction probabilities and too small phase lags at temperatures above 550 K.

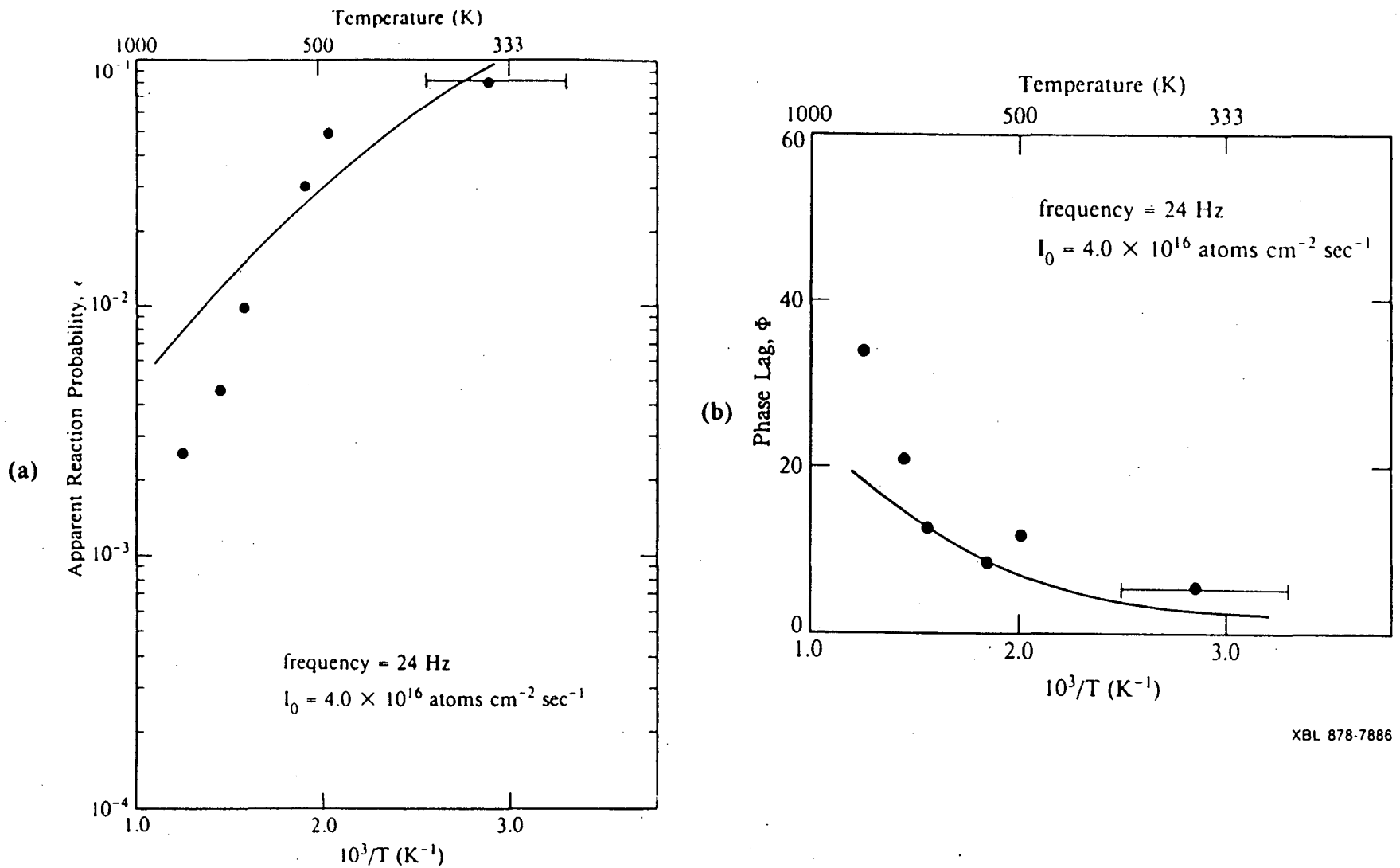


Fig. 5.6. The theoretical (line) and measured (points) apparent reaction probabilities (a), and phase lags (b) versus reciprocal temperature; f = 24 Hz, and $I_0 = 4.0 \times 10^{16}$ atoms cm$^{-2}$ sec$^{-1}$.

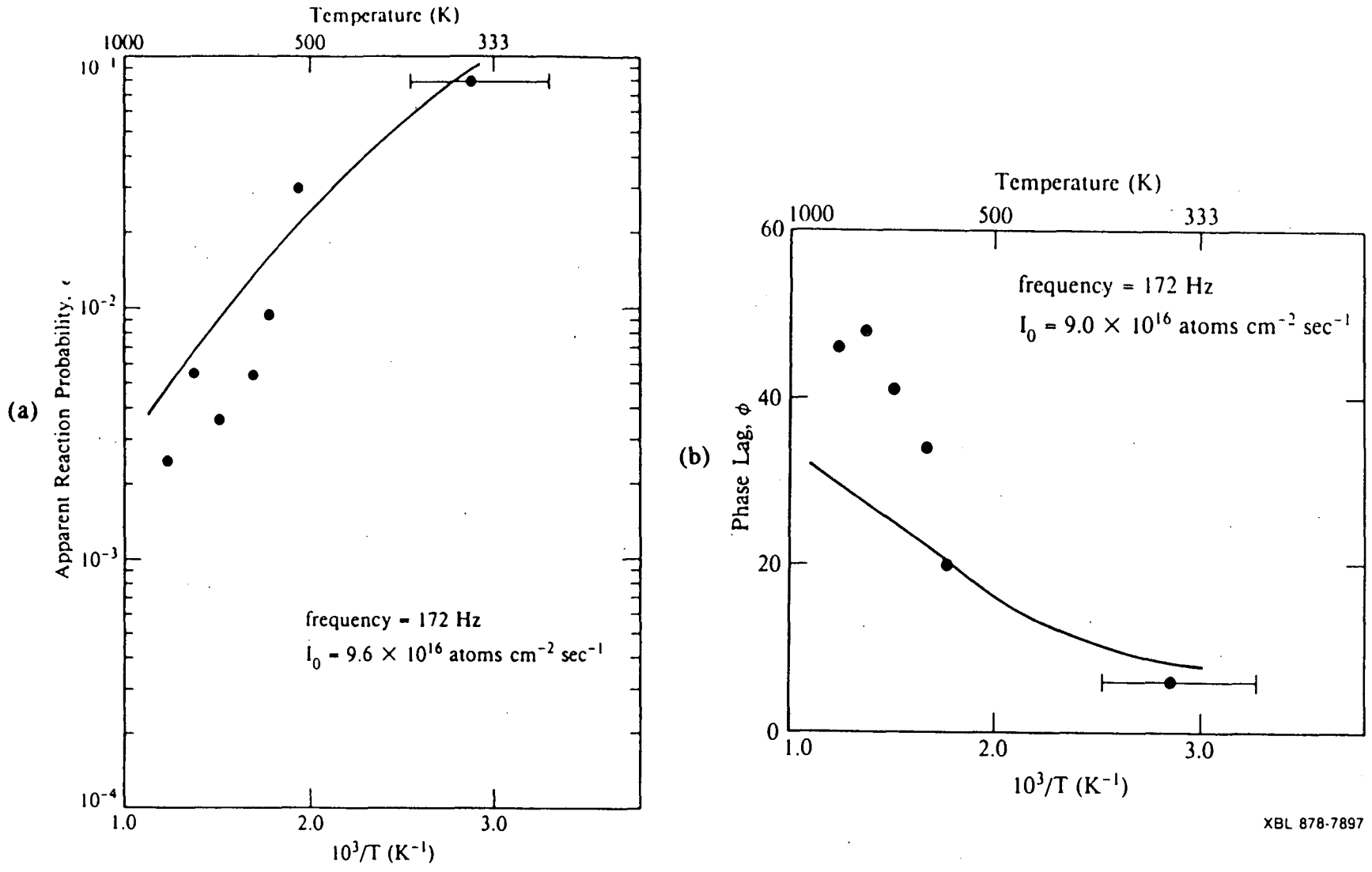


Fig. 5.7. The theoretical (line) and measured (points) apparent reaction probabilities (a), and phase lags (b) versus reciprocal temperature; f = 172 Hz, and $I_0 = 9.6 \times 10^{16}$ atoms $cm^{-2}$ $sec^{-1}$.

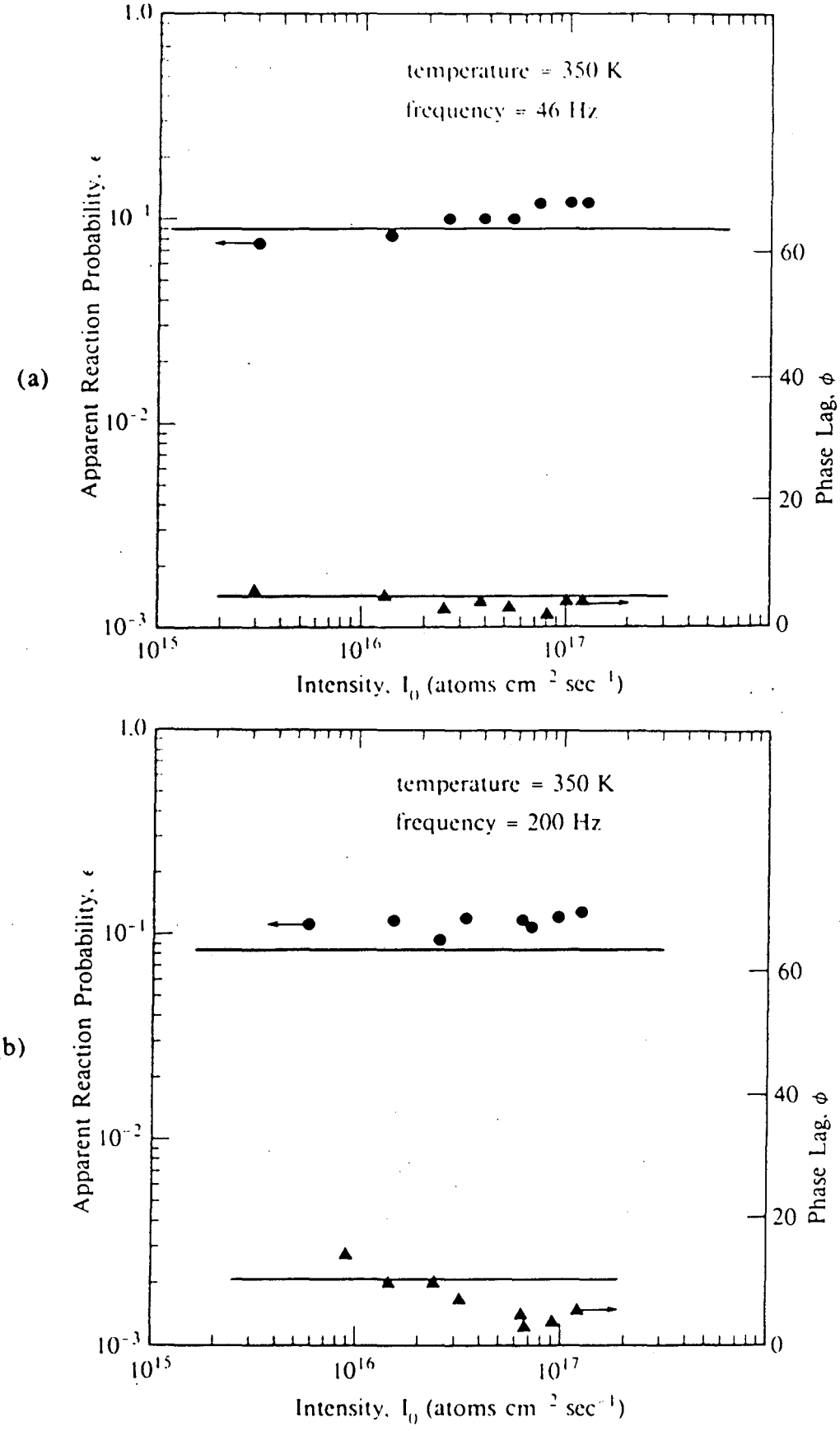


Fig. 5.8. The theoretical (line) and the measured apparent reaction probabilities and phase lags versus the beam intensity at a temperature of 350 K: (a) f = 46 Hz, (b) f = 200 Hz.

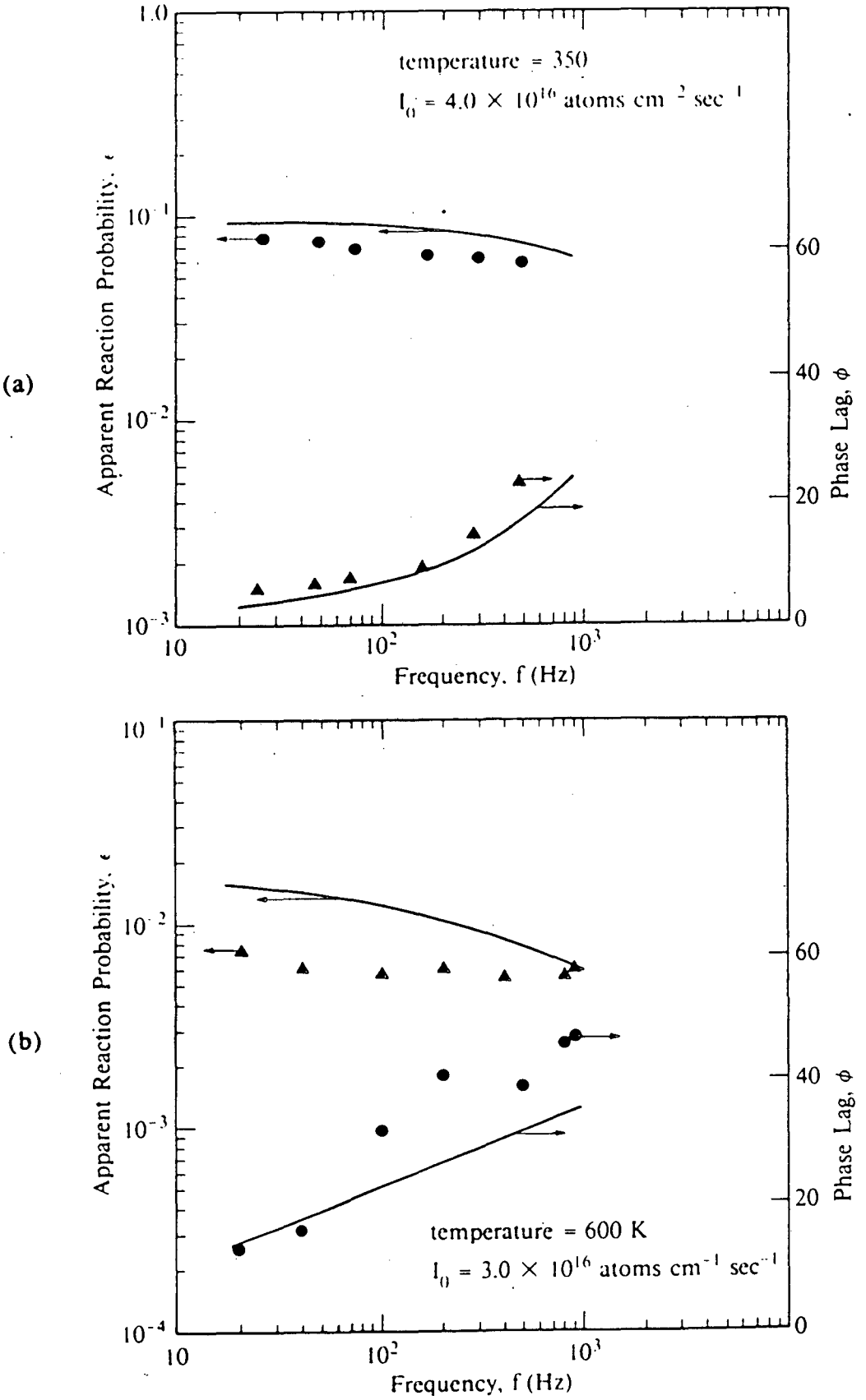


Fig. 5.9. Frequency dependence of theoretical (line) and measured (points) apparent reaction probabilities and phase lags: (a) T = 350 K and $I_0 = 4.0 \times 10^{16}$ atoms cm$^{-2}$ sec$^{-1}$, (b) T = 600 K and $I_0 = 3.0 \times 10^{16}$ atoms cm$^{-2}$ sec$^{-1}$.

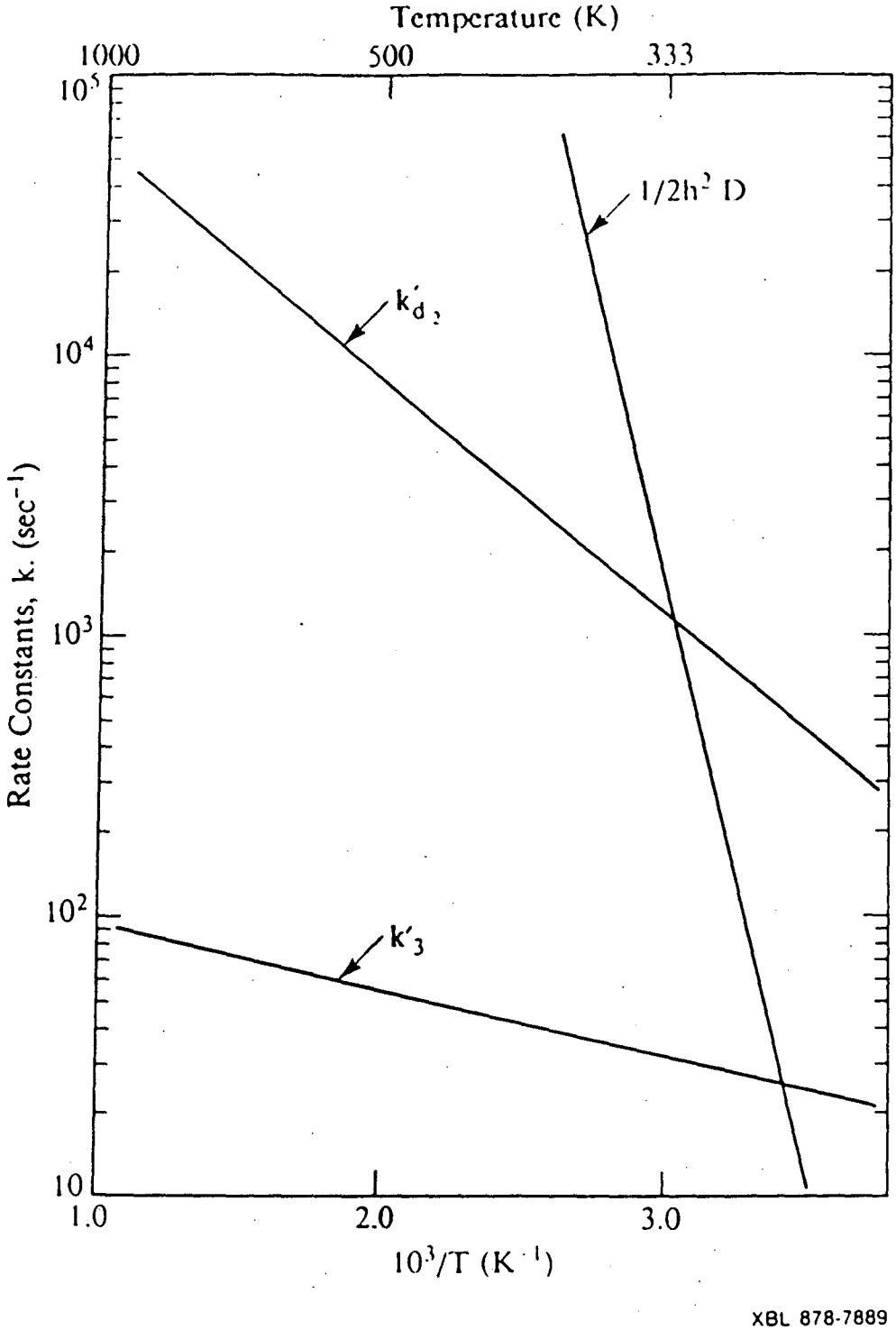


Fig. 5.10. Arrhenius plot of the rate constants from Table 5.3.

# 6. DISCUSSION

## 6.1. Saturation of Strongly-Bound Hydrogen

The proposed mechanism requires that the surface dangling bonds are always saturated. However, the TDS results (fig. 5.4) show that these strongly-bound H atoms start to desorb at 600 K by surface recombination processes;

$$2SiH \rightarrow 2Si(s) + H_2(g) \tag{6.1}$$

$$SiH_2 \rightarrow Si(s) + H_2(g) \tag{6.2}$$

The occurrence of these desorption reactions will introduce new reaction steps (Eqs. 6.1 and 6.2) to the mechanism. Such an addition of thermal desorption reactions will modify Eq. 5.12 to account for variations in the concentration of empty sites. The surface balance on the sites as a variable will introduce non-linearity into the reaction model. Since the experimental results (figs. 4.7 & 4.8) show a linear dependence on the atomic hydrogen beam intensity, non-linear processes are ruled out. On the other hand, the desorption from these strongly-bound H on the surface could occur but the Si sites exposed are quickly refilled by either the weakly-bound mobile H atoms or directly from the beam source to nullify the "empty site" effect on the overall mechanism. To verify this assumption *a posteriori*, a steady state mass balance of H atoms on the surface is analyzed. The analog of Eq. 5.12 for this situation involves supply of H atoms to the surface by a constant flux $I_{ss}$. Physisorbed hydrogen reacts with the chemisorbed layer to produce $SiH_4$ and recombined $H_2$ at rates which now depend upon the fraction of the surface binding sites which are occupied (i.e., on the coverage, $\theta$, of the chemisorbed hydrogen). In addition, the physisorbed hydrogen can spill over onto the empty chemisorption sites with a rate constant $k_{tr}$. Because steady state is assumed, the bulk solid is saturated with hydrogen so the diffusion term in Eq. 5.12 disappears. However, the loss term due to direct desorption of hydrogen from the chemisorbed layer appears in the balance equation. Because the strongly-bound layer is no longer completely

saturated, an additional hydrogen balance equation is needed.

For the chemisorbed layer, the balance equation is:

$$I_{ss}(1 - \theta) + k_{tr}n(1 - \theta) = k_R n\theta + 2k_d N_s \theta \tag{6.3}$$

where $k_d$ is the rate constant for the assumed first order desorption of the chemisorbed hydrogen, the rate of which is given by the last term. The terms on the left hand side of Eq. (6.3) represent direct filling of empty chemisorption sites from the beam and transfer of weakly bound hydrogen to the chemisorption layer, respectively. The first term on the right hand side gives the loss of chemisorbed hydrogen by the reaction to produce silane and recombination:

$$k_R = 4k'_3 + 2k'_{d_2}$$

The balance equation for physisorbed hydrogen is:

$$\eta I_{ss}\theta = k_R n\theta + k_{tr}n(1 - \theta) \tag{6.4}$$

Solving this equation for $k_R n$ yields:

$$k_R n = \frac{\eta I_{ss}\theta}{\theta + \gamma(1 - \theta)}$$

which, when substituted into Eq. (6.3) gives the following equation which must be solved for the coverage of the strongly-bound layer:

$$y + \eta\left(\frac{\gamma y - 1}{\gamma y + 1}\right) = G \tag{6.5}$$

where

$$\gamma = \frac{k_{tr}}{k_R}$$

and

$$y = \frac{1 - \theta}{\theta}$$

$$G = \frac{2k_d N_s}{I_{ss}}$$

Using $I_{ss} = 10^{16}$, $N_s = 8 \times 10^{14}$, Schulze and Henzlers's value for $k_d$ (first-order

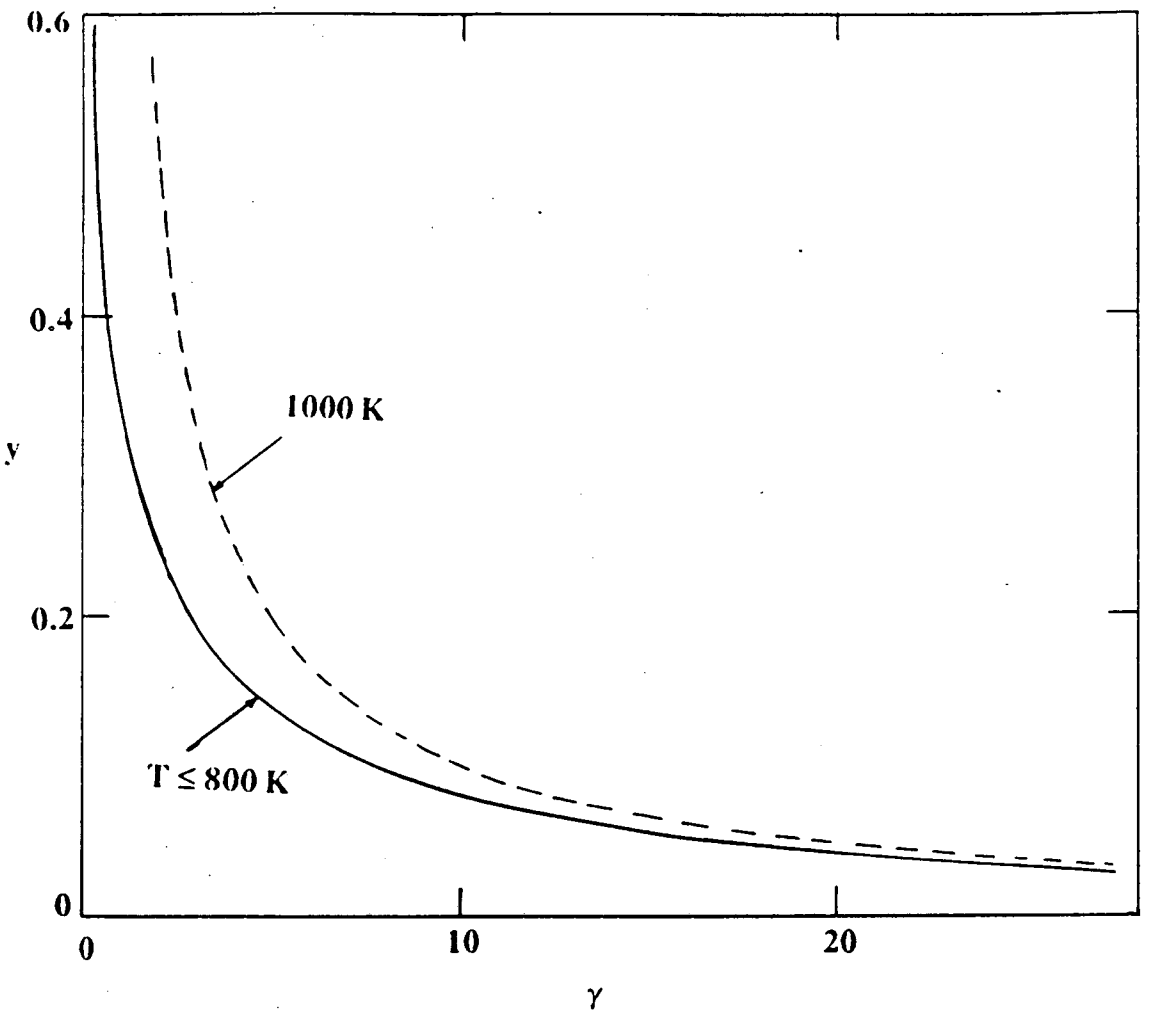


Fig. 6.1. A plot of coverage versus $\gamma$ at various temperatures.

rate constant) as a function of temperature (Table 5.1), and $\eta = 0.7$. For temperatures up to 800 K and the above determined constants Eq. 6.5 could be reduced to an explicit function of y in terms of $\gamma$:

$$y = \frac{\sqrt{(1 + 0.7\gamma)^2 + 2.8\gamma} - (1 + 0.7\gamma)}{2\gamma} \tag{6.6}$$

A plot of Eq. (6.6) and Eq. 6.5 for a temperature of 1000 K is shown in Fig. 6.1. The plot (Fig. 6.1) shows that for $\gamma > 20$, the Si surface stays covered with the strongly-bound H atoms up to 1000 K where most of the molecular beam data were taken. However, this being a steady-state analysis of a process (i.e. the molecular beam technique) which is time-dependent does not present an accurate picture of the surface behaviour. Nevertheless, the proceeding calculation shows that the assumption that the Si surface remains saturated with the strongly-bound hydrogen should be adequate in the low-temperature range. Any deviation from saturation should only affect the high-temperature results. In fact the model fits the low temperature data better than the high temperature data.

## 6.2. Rate Constants

The model entails successive addition of H atom to Si to produce silane and recombination of adsorbed H atoms to generate $H_2$ gas. These two processes are similar to the model considered by Veprek and Sarrott[23], who estimated an activation energy of $\approx 10$ kcal/mole for $SiH_4$ formation. The activation energy of the modified rate constant, $k'_3$ for the silane channel is 1.8 kcal/mole (Table 5.3). This activation energy, $E'_3 = E_3 + \Delta H$; where $E_3$ is the activation energy of $k_3$ (Eq. 5.7). Even though considerable uncertainty exists in the estimate of $\Delta H = -0.4$ kcal/mole (section 5.2.4), the results suggest that $\Gamma$ is not highly activated. It is therefore concluded from this estimate that the activation energies of the modified rate constants $k'_3$ and $k'_{d_2}$ (defined by Eqs. 5.18 and 5.19) are approximately equal to the activa-

tion energies of the $k_3$ and $k_{d_2}$, respectively. Since $E'_3 = 1.8$ kcal/mole $E_3 = E'_3 - \Delta H$, has a value of 2.2 kcal/mole. This $E_3$ value confirms Veprek and Sarrott's assertion that the activation energy for $SiH_4$ formation is low, which is to be expected for a reaction which takes place at room temperature. From Table 5.3 the activation energy for the heterogeneous recombination rate constant (Eq. 5.6) is 4.5 kcal/mole, which is a factor of two higher than the theoretical estimate of 2.3 kcal/mole by Veprek et al.[23]. Also in the gas phase hydrogen abstraction reaction,

$$H + SiH_4 \longrightarrow H_2 + SiH_3 \tag{6.7}$$

Choo et al.[106] measured an activation energy of 3.8 kcal/mole. Notwithstanding the fact that the above reaction is a homogeneous gas-phase reaction, it involves the following reaction steps: (a) breaking of an Si-H bond and (b) recombination of H atoms to form molecular hydrogen. Thus the mechanisms for this reaction and the heterogeneous recombination reaction (Eq. 5.6) are similar and therefore it is expected that the energetics would be comparable, as they are.

The pseudo first-order rate constants, $k'_3$ and $k'_{d_2}$ have preexponentials (Table 5.3) that compare with the recombination reaction analysis of hydrogen on platinum[107] and also fall within theoretical estimates[108].

If the measured diffusion coefficient, **D**, of hydrogen in crystalline silicon (Eq. 4.13) is extrapolated to the low-temperature range of the molecular beam measurements then the diffusion coefficient, **h**, could be calculated from the bulk solution-diffusion rate constant, $\frac{1}{2}h^2D$ (Table 5.3).

$$h = 2.8 \times 10^7 e^{\left(-\frac{1.7}{RT}\right)} \ \text{cm}^{-1} \tag{6.9}$$

With this known value of **h**, the subsurface concentration of H atoms in Si is estimated. For example at a temperature of 350 K, a frequency of 172 Hz and beam intensity of $9.0 \times 10^{16}$ Eq. (5.25) of the model gives a steady-state surface concentra-

tion of weakly-bound H atoms of $9.7 \times 10^{12}$, and using Eq. 5.9, a subsurface concentration of 454 ppm are obtained. From secondary ion mass spectroscopy (SIMS) profiles, Johnson[109,110] reported deuterium levels of 20--2000 ppm in Si by low-energy plasma exposure. Pankove et al.[111] have also reported values of 385 ppm in their hydrogenation of Si at 398 K by exposure to H atoms generated by an rf glow discharge in 0.2 torr of hydrogen gas for 156 hours. Even though the introduction process for H atoms into Si from these literature reports are different from the molecular beam process, their estimates of the near-surface H content in Si is in good agreement with the present results.

Direct comparison of the bulk solution-diffusion rate constant, $\frac{1}{2}h^2D$ obtained from the molecular beam model and that estimated from the solubility measurements in conjunction with the potential energy diagram is inappropriate given the differences in both processes. Whereas the solubility mechanism involves dissociation-adsorption of $H_2$ followed by H atom diffusion into the bulk, the molecular beam process which starts with atomic hydrogen, is highly influenced by $SiH_4$ formation and the heterogeneous recombination of the surface adsorbed H atoms. Another significant difference is that the two experiments were conducted at different temperature ranges. Caution has to be taken in extrapolating the high temperature values of D measured by Wieringen and Warmoltz (Eq. 4.15) and the estimated h from the solubility measurement. Nonetheless, the model predicts a subsurface concentration which is several orders of magnitude higher than either the extrapolation of fig. 4.12, the doping concentration or the point defect densities of the silicon target. This is because the number of available sites for hydrogen bonding determines the amount of hydrogen that can be incorporated in the Si lattice rather than solution of random interstitials, which is the characteristic of hydrogen in pure metals.

Despite the difficulty in exact comparison of $\frac{1}{2}h^2D$ from the model and the estimate from the solubility measurements, the latter method gives an estimate of solubility coefficient, **h**, which increases with increasing temperature. The calculation of **h** from the model (Eq. 6.9) confirms this increase with increasing temperature. More importantly, the prior estimate of $\frac{1}{2}h^2D$ justified the inclusion of the bulk solution-diffusion step in the model.

The high sticking probability, $\eta$, of $0.7 \pm 0.1$ predicted by the model confirms the assumption[91–93] that the atomic hydrogen sticking on Si is close to unity. Of this high sticking of H atoms on the Si surface only a small fraction ($\approx 3\%$) reacts to produce $SiH_4$; most of it is catalytically recombined to give $H_2$ gas.

### 6.3. Structural Sensitivity

The high-temperature results above the surface transition clearly show a different mechanism. Pandey et al.[114] reported from photoemission spectra analysis that a trihydride phase ($SiH_3$), is present on artificially stablized Si(111)-1x1 surface structure instead of the monohydride, SiH seen on the Si(111)-7x7. In fact the $SiH_3$ complex is stable up to 973K. Since reaction intermediates determine the ultimate surface kinetics and mechanism, it is highly probable that a different theoretical model would be needed to fit the data above the transition temperature. However, when the sample was replaced by Si(100) (Fig. 5.6) the temperature response of $\varepsilon$ and $\Phi$ below the transition region did not show any difference compared to Si(111) (Fig. 5.7) behavior. No experiment was conducted on the Si(100) specimen beyond the transformation temperature. Thus the unusual response of apparent reaction probability and phase lag to temperature changes up to 1000 K is most likely caused by the heterogeneous recombination reaction (Eq. 5.6) and bulk solution-diffusion (Eq. 5.4) of the surface adsorbed H atoms. Nevertheless, the surface structure might still influence the formation of silane through the distribution of

SiH and $SiH_2$ complexes with temperatures changes. The surface structure determines the characteristics of the surface, like defects, kinks and corrugations which constitute active sites on the surface.

### 6.4. Etching Rate

The apparent reaction probability of $\approx 3\%$ translates to Si etching rate of $\approx 8 \times 10^{-3}$ $\mu$m/m at an atomic hydrogen pressure of $2 \times 10^{-4}$ torr. Even though extrapolation of this low-pressure etching rate to higher pressures for comparison with other literature values involves some uncertainties, due to the influence of surface coverage on the sticking probability and the possibility of a different reaction mechanism at high pressure, it is the only way feasible. Another factor of uncertainty in this comparison with the reported literature values[14,22] (section 1.4) is the difficulty in precisely determining the atomic hydrogen pressures in those experiments. However, a linear extrapolation of the measured etching rate gives Si removal rate of about 0.4 $\mu$m/m at 0.01 torr of atomic hydrogen pressure.

The etching rate of silicon by atomic hydrogen is higher than carbon reaction with H gas[5], but lower than silicon reactions with the halogens. However, the atomic hydrogen reaction with silicon is well suited for removal of a few layers of Si without any distortion of the lattice which is inherent to sputtering processes. Additionally, the surface remains relatively smooth with H atoms reaction compared to severe roughening caused by halogens (F and Cl) reactions[121] and the hydrogen-etched-surface can be restored to the original state[23] by annealing at low temperatures (< 700 K).

## 7. CONCLUSIONS

The etching of Si(111) by atomic hydrogen gas using the modulated molecular beam method produced $SiH_4$ as the sole product. The $SiH_4$ exhibits a $\approx 3\%$ reaction probability at room temperature and decreases with increasing temperature within the temperature range 300 K – 1000 K.

The surface reaction is structure-sensitive, showing a discontinuity at the temperature range where the surface structure of Si(111)-7x7 is known to undergo a second-order transformation to Si(111)-1x1. However, below 1000 K, the reaction probability of Si(111) and Si(100) surfacs are the same.

Molecular hydrogen does not react directly with the silicon or with the reaction intermediates on the surface supplied by an auxillary hydrogen beam.

Ion bombardment has no effect on the surface reaction.

The mechanistic interpretation of the modulated molecular beam data (T < 1000 K), coupled with TDS, EELS and IRS concepts is predicated on saturation of the surface dangling bonds by H-atoms forming SiH and $SiH_2$ complexes. The complexes occupy two different sites ($\beta_1$ & $\beta_2$) on the surface and their concentrations are temperature dependent. In addition there is a third, weakly-bound H adlayer which is mobile. The mobile H-atoms interacts with SiH complex to form recombined $H_2$ gas; with the $SiH_2$ complex to form $SiH_4$; and also dissolves and diffuses into the bulk of the silicon.

The solubility of hydrogen in silicon measured by the infusion-outgassing method shows a one-half power pressure dependence and a positive heat of solution (endothermic absorption).

The outgassing thermal desorption spectrum indicates three distinct binding sites of hydrogen in silicon. The binding energies of these states are in good agreement with prior theoretical predictions.

## 8. ACKNOWLEDGEMENT

My sincere thanks to Professor Donald R. Olander of Nuclear Engineering Department, University of California for providing such a challenging problem, and for his support and guidance throughout the entire work.

A special thanks to Dr. Mehdi Balooch for his assistance in running the experiment and other consultations in producing this thesis.

I would also like to thank Dan Winterbauer and his co-worker, and Jack Harrell for their assistance in keeping the equipment running.

Last but not the least, I would like to extend my thanks to the Ghana Atomic Energy Commission for giving me the opportunity to study in this country as well as all my friends whose various contribution made this work come to a fruitful conclusion.

# APPENDIX I

## 9. THEORETICAL BEAM ANALYSIS

### 9.1. Pressure Drop Calculation

For the pressure range at which the molecular beam is operated (0.1 - 6.0 torr), gas flow through the tubing is in the transition flow range, in which the flow is a mixture of viscous and free molecular flow. The conductance of a cylindrical tube for such a flow has been deduced empirically by Knudsen[115], and is given by

$$C = C_v + ZC_t \tag{I.1}$$

where $C_v$, $C_t$ are the "slip-free" viscous and the free molecular flow conductances, respectively:

$$C_v = \frac{\pi a^4}{8\eta l} P_a \tag{I.2}$$

$$C_t = \frac{2\pi a^3}{3l} v_a \tag{I.3}$$

$P_a$ is the arithmetic mean pressure of the two points at the extremities of the tube, and $v_a$ is the mean velocity. The parameter Z is:

$$Z = \frac{1 + 2.507(a/\lambda_a)}{1 + 3.095(a/\lambda_a)} \tag{I.4}$$

where a is the tube radius, $l$ its length and $\lambda$ is the mean free path calculated at $P_a$. The gas viscosity is $\eta$.

The mean free path, $\lambda$ is the distance a particle will travel on the average before undergoing a collision with another molecule. It is inversely proportional to the particle density and diameter. The theoretical analysis by Knudsen[116] gives,

$$\lambda = \frac{1}{\sqrt{2}\pi n \xi^2} = \frac{kT}{\sqrt{2}\pi \xi^2 P} \tag{I.5}$$

where **n** is is the gas density, and $\xi$ the molecular diameter.

For a binary gas,

$$\lambda_1 = \frac{1}{\sqrt{2}\pi n_1 \xi_1^2 + \pi n_2 \xi_3^2 \left(1 + \frac{M_1}{M_2}\right)^{1/2}} \tag{I.6}$$

where the subscripts 1 represents atomic hydrogen, 2 for molecular hydrogen and 3 represents the average value for the two species. M is the molecular weight.

$$\lambda_2 = \frac{1}{\sqrt{2}\pi n_2 \xi_2^2 + \pi n_1 \xi_3^2 \left(1 + \frac{M_2}{M_1}\right)^{1/2}} \tag{I.7}$$

And the average mean free path, $\lambda_3 = \dfrac{\lambda_1 P_1 + \lambda_2 P_2}{P}$.

$P_1$ and $P_2$ are the partial pressures of atomic and molecular hydrogen, respectively. P is the total pressure. The flow geometry is shown schematically in figs. 3.2 and 3.3. The exact total pressure of the beam, P in the oven is required in order to determine the leak rate into the vacuum. The flow through the conduit is given by:

$$Q = C\Delta P = \frac{\dot{m}_0 kT}{M} \tag{I.8}$$

Eq. I.8 gives:

$$\dot{m}_0 = \frac{MC\Delta P}{kT} \tag{I.9}$$

where $\dot{m}_0$ is mass flow rate through the conduit. C is capacitant of the flow path.

### 9.2. Flow Through the Orifice

The molecular hydrogen is thermally dissociated in the tungsten oven at 2500 K. The partial pressures of each of the species, molecular and atomic hydrogen is dependent on the total hydrogen pressure, P, in the oven. Thermodynamic

equilibrium is assumed in calculating the partial pressures. The equilibrium equation for hydrogen dissociation is:

$$\tfrac{1}{2}\,H_2 \xrightarrow{K_{eq}} H \tag{I.10}$$

The law of mass action gives the following relation between the equilibrium constant and the partial pressures:

$$K_{eq} = \frac{P_1}{\sqrt{P_2}} \tag{I.11}$$

and

$$P = P_1 + P_2 \tag{I.12}$$

The partial pressures of atomic and molecular hydrogen is calculated from equations I.11 & I.12:

$$P_1 = \tfrac{1}{2}\left(-K_{eq}^2 + \sqrt{K_{eq}^4 + 4K_{eq}^2 P}\right) \tag{I.13}$$

and

$$P_2 = P - P_1 \tag{I.14}$$

where

$$K_{eq} = \exp(-18.33/RT)$$

The activation energy from Ref. 117 and 118 is in kcal/mole. The type of flow through the oven orifice is total-pressure dependent. It is either one of the three types of flow; (1) Free molecular flow, (2) Hydrodynamic flow, or (3) Transition flow.

### 9.2.1. Free Molecular Flow through the Orifice

At pressures where the mean free path is greater than the orifice diameter (1 mm), the flow is limited by collisions of molecules with the walls instead of molecular collisions. The number of particles which impinge on a unit surface area of the

wall is given by[119],

$$v = \frac{1}{4} n v_a = 3.513 \times 10^{22} \frac{P(\text{torr})}{\sqrt{MT}} \quad \text{cm}^{-2}\text{sec}^{-1} \tag{I.15}$$

For a cross-sectional area $A = \pi a_0^2$, the total leak rate, $l$, through the orifice for a free molecular flow is given by:

$$l = vA = 1.1036 \times 10^{23} a_0^2 \frac{P(\text{torr})}{\sqrt{MT}} \quad \text{sec}^{-1} \tag{I.16}$$

Thus the respective leak rates of atomic hydrogen and molecular hydrogen at 2500 K are:

$$l_1 = 1.5608 \times 10^{21} a_0^2 P_1(\text{torr}) \tag{I.17}$$

$$l_2 = 1.1036 \times 10^{21} a_0^2 P_2(\text{torr}) \tag{I.18}$$

The total mass flow rate through the orifice for a free molecular flow is calculated by substituting Eqs. I.17 & I.18 into the following:

$$\dot{m}_0^f = m_1 l_1 + m_2 l_2 = (2l_1 + 4l_2)/N \tag{I.19}$$

The superscript f denotes free molecular flow; $m_1$ and $m_2$ are the atomic and molecular weights of H and $H_2$, respectively; and N is the Avogadro's number. The pressure drop through the conduit for a free molecular flow through the orifice is computed by equating Eqs. I.19 and I.9.

### 9.2.2. Hydrodynamic Flow through the Orifice

At oven total pressures where the mean free path is much less than the orifice diameter, the critical flow through the orifice occurs:

$$\dot{m}_0^h = \pi a_0^2 P C_0 \left\{ \frac{\gamma M}{RT} \left( \frac{2}{\gamma + 1} \right)^{\frac{\gamma+1}{\gamma-1}} \right\}^{1/2} \quad \text{g/s} \tag{I.20}$$

where $C_0$ is the discharge coefficient = 0.85; $\gamma$ is the average $C_p/C_v$ for the two species,

$$\gamma = \frac{\gamma_1 P_1 + \gamma_2 P_2}{P} \tag{I.21}$$

The superscript h denotes hydrodynamic flow; and M is the weighted average molecular weight.

$$M = \frac{M_1 P_1 + M_2 P_2}{P} \tag{I.22}$$

The pressure drop for a hydrodynamic flow through the orifice is then calculated by equating Eq. I.20 to Eq. I.9. The mass flow rate for atomic and molecular hydrogen and their respective leak rates are given by the following equations:

$$\dot{m}_1^h = \frac{\dot{m}_0^h P_1/P_2}{2 + P_1/P_2} \tag{I.23a}$$

$$l_1^h = \frac{\dot{m}_1^h N}{M_1} \tag{I.23b}$$

$$\dot{m}_2^h = \dot{m}_0^h - \dot{m}_1^h ; \qquad l_2^h = \frac{\dot{m}_2^h N}{M_2} \tag{I.24a,b}$$

Note that in the computations for the pressure drop, an initial value of P (oven total pressure) is assumed in order to estimate the values of the parameters in Eq. I.20. And from the estimate of the pressure drops for each P, the upstream pressure is calculated. This also applies to the other two types of flow (free molecular and transition) discussed.

### 9.2.3. Transition Flow through the Orifice

A Liepmann criterion is used to determine the boundaries for the three types of flow through the orifice.

$$Kn > 16.6 \quad \text{hydrodynamic flow}$$

$$Kn < 1.6 \quad \text{free molecular flow}$$

$$16.6 > Kn > 1.6 \quad \text{transition flow.}$$

Kn is the modified Knudsen number and is defined as:

$$Kn^{-1} = 2.512\frac{a_0}{\lambda_0}$$

The flow in the transition region is a mixture of hydrodynamic and free molecular flows. The fraction, $\delta$, which is hydrodynamic is defined as:

$$\delta = \frac{Kn - 1.6}{16.6 - 1.6} \tag{I.25}$$

For a transition flow through the orifice, the mass flow rates of atomic and molecular hydrogen are calculated using the equations in sections 9.2.1 and 9.2.2 for free molecular flow fraction and the hydrodynamic flow fraction, respectively. The H mass flow rate and the $H_2$ for this mixed flow are calculated by the following equations:

$$\dot{m}_1^t = (1 - \delta)\dot{m}_1^f + \delta\dot{m}_1^h \tag{I.26a}$$

$$\dot{m}_2^t = (1 - \delta)\dot{m}_2^f + \delta\dot{m}_2^h \tag{I.26b}$$

where the superscript t denotes transition flow. The total mass flow rate is the sum of the above two equations:

$$\dot{m}_0^t = \dot{m}_1^t + \dot{m}_2^t \tag{I.27}$$

The pressure drop for a transition flow through the orifice is determined by equating Eqs. I.9 and I.27.

# APPENDIX II

## Analysis of Experimental Data for Si/H Reaction by The Modulated Molecular Beam Mass Spectrometry

### Nomenclature

$a^x_{y^+}$ = fraction of neutral x ionized to $y^+$

$S_{y^+}$ = signal of $y^+$

$\bar{v}_x$ = mean velocity of x

$I_1$, $I_2$ = flux of H or $H_2$ incident on the surface

$F_x$ = flux of x from the Si surface

$t_{y^+}$ = transmission efficiency of $y^+$

$\gamma_{y^+}$ = secondary electron coefficient of electron multiplier.

e = electronic charge

$\sigma_x$ = ionization cross-section of neutral species x

$f_x$ = relative angular distribution factor

Subscripts 1 = H; 2 = $H_2$; 3 = $SiH_3$; 4 = $SiH_4$ and tr = transit

Superscripts s = scattering; p = product; and RE = recombined.

In a modulated molecular beam analysis where only a small fraction of the incident beam reacts with the target, an apparent reaction probability, $\varepsilon$, is simply defined as the ratio of the product signal to the reflected reactant signal. Because a large fraction of the incident atomic hydrogen beam recombined (Eq. 5.6) on the Si surface in this work, such a simple definition was not applicable. In order to obtain the experimental variables $\varepsilon$ and $\Phi$ from the signal measurements, an elaborate calculations that involves a analysis of the first Fourier component of the square

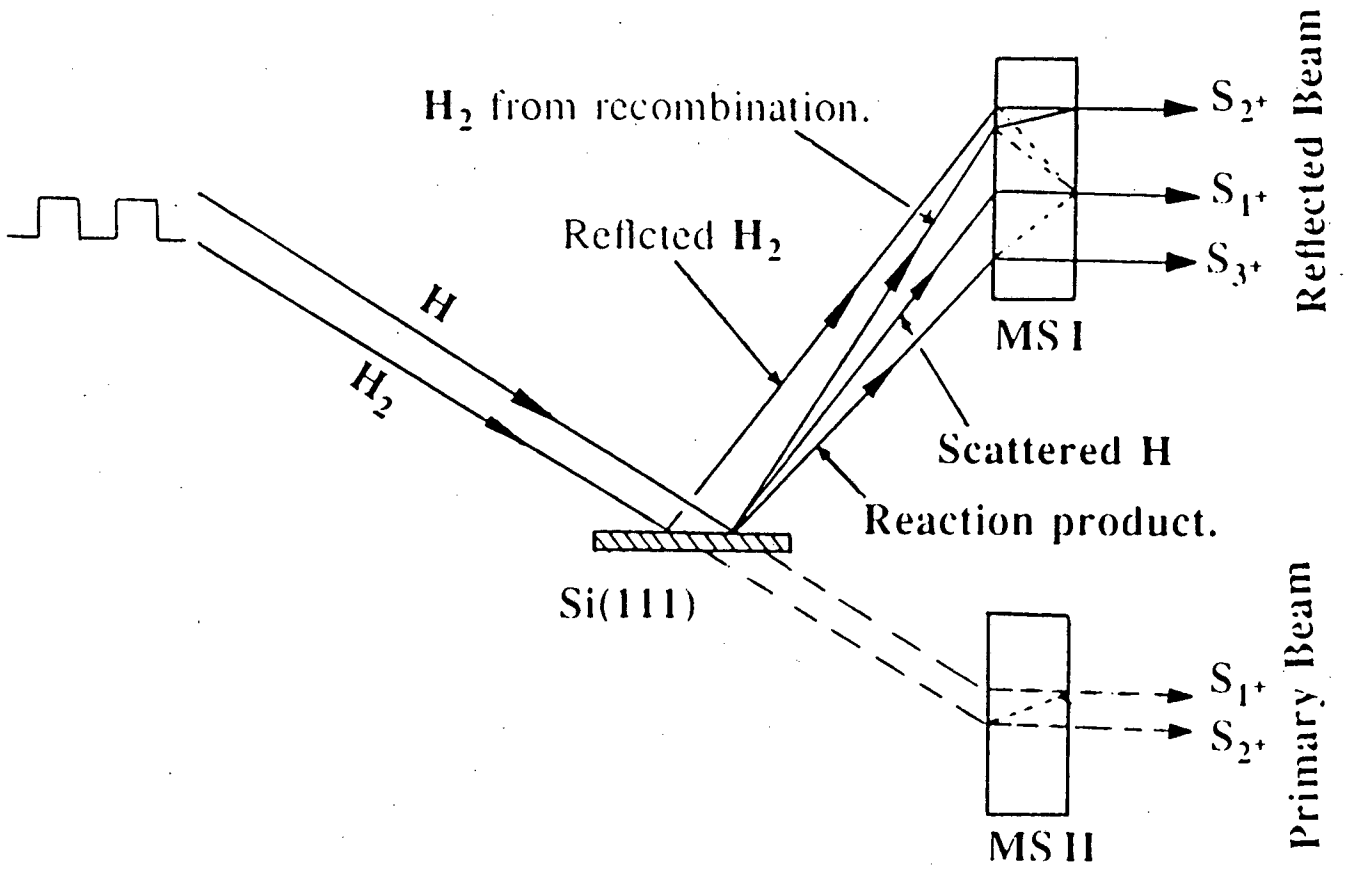


Fig. I.1. Schematic of the paths of the incident and scattered beams of modulated molecular beam apparatus.

modulated signal, surface mass balances and determination of beam intensities from direct beam (MSII) and leak rate measurements was utilized. In the calculations the fluxes of the species are converted to mass spectrometer signals. Fig. II.1 shows the paths of the incident species (H and $H_2$) as they strike the Si surface; the reflected species (H and $H_2$) and the desorbed products (recombined $H_2$ and $SiH_4$) as they travel through the mass spectrometer ionizer.

### Scattered Beam Analysis

The first Fourier component for the instantaneous scattering of an incident square modualted beam is:

$$F_2^s = \frac{2}{\pi} I_2 \quad \text{for } H_2 \tag{II.1}$$

and

$$F_1^s = \frac{2}{\pi} (1 - \eta) I_1 \quad \text{for H} \tag{II.2}$$

The relation between the product flux, $F_4^p$ and $I_1$ is model-dependent

$$F_4^p = F_{40}^p e^{-i\Phi_{R4}} \tag{II.3}$$

where $\Phi_{R4}$ = reaction phase lag of $SiH_4$.

The apparent reaction probability is defined as:

$$\varepsilon_4 = \frac{4F_{40}^p}{\frac{2}{\pi} I_1} \tag{II.4}$$

Similary for the recombination reaction

$$F_2^{RE} = F_{20}^{RE} e^{-\Phi_{RE}} \tag{II.5}$$

$$\varepsilon_2 = \frac{2F_{20}^{RE}}{\frac{2}{\pi} I_1} \tag{II.6}$$

Relating the first Fourier component of the product flux ($F_4^p$) flux to the signal

($S_{3^+}$, for $SiH_3^+$) measured by the lock-in amplifier gives:

$$S_{3^+} = S_{30}\, e^{-i\Phi_3} = K_{ig}\, \alpha_4^p\, \Psi_{tr,4}\, F_{40}^p\, e^{-i\Phi_{R4}} \tag{II.7}$$

where

$S_{30}$ = amplitude; and $\Phi_3$ = phase of $SiH_3^+$.

$\Psi_{tr,4}$ = the transit amplitude factor.

$K_{ig}$ = instrument and geometric constant

$\Phi_{R4} = \phi_{R4} + \phi_{tr,4}$

$\phi_{R4}$ = reaction phase lag

$\phi_{tr,4}$ = transit phase lag

$$\alpha_4^p = \frac{a_{3^+}^4\, \sigma_4\, t_{3^+}\, \gamma_{3^+}\, f_p^4\, \sqrt{M_4}}{\sqrt{T_4}} \tag{II.8}$$

Similarly, for the signal of mass 2:

$$S_{2^+} = S_{20}\, e^{-i\Phi_2} = K_{ig}\left\{\alpha_2^p\, \Psi_{tr,4}\, F_{40}^p\, e^{-i\phi_{R4}} + \alpha_2^{2s}\, F_2^s + \alpha_2^{2RE}\, F_{20}^{RE}\, e^{-i\phi_{R2}}\right\} \tag{II.9}$$

where,

$$\alpha_2^p = \frac{a_{2^+}^4\, \sigma_4\, t_{2^+}\, \gamma_{2^+}\, f_4^p\, \sqrt{M_4}}{\sqrt{T_4^p}} \tag{II.10}$$

$$\alpha_2^{2s} = \frac{a_{2^+}^4\, \sigma_2\, t_{2^+}\, \gamma_{2^+}\, f_2^s\, \sqrt{M_2}}{\sqrt{T_2^s}} \tag{II.11}$$

$$\alpha_2^{2RE} = \frac{a_{2^+}^{RE}\, \sigma_2\, t_{2^+}\, \gamma_{2^+}\, f_2^{RE}\, \sqrt{M_2}}{\sqrt{T_2^{RE}}} \tag{II.12}$$

Finally, for the mass-one signal:

$$S_{1^+} = S_{10}\, e^{-i\Phi_1} = K_{ig}\left\{\alpha_1^s\, F_1^s + \alpha_1^{2s}\, F_2^s + \alpha_1^{RE}\, e^{-i\Phi_{R2}} + \alpha_1^p\, \Psi_{tr,4}\, F_{40}^p\, e^{-i\Phi_{R4}}\right\} \tag{II.13}$$

where

$$\alpha_1^s = \frac{a_{1^+}^1 \, \sigma_1 \, t_{1^+} \, \gamma_{1^+} \, f_1^s \sqrt{M_1}}{\sqrt{T_1^s}} \tag{II.14}$$

$$\alpha_1^{2RE} = \frac{a_{1^+}^{RE} \, \sigma_2 \, t_{1^+} \, \gamma_{1^+} \, f_2^{RE} \sqrt{M_2}}{\sqrt{T_2^{RE}}} \tag{II.15}$$

$$\alpha_1^{2s} = \frac{a_{1^+}^{2s} \, \sigma_2 \, t_{1^+} \, \gamma_{1^+} \, f_2^s \sqrt{M_2}}{\sqrt{T_2^s}} \tag{II.16}$$

$$\alpha_1^p = \frac{a_{1^+}^4 \, \sigma_4 \, t_{1^+} \, \gamma_{1^+} \, f_4^p \sqrt{M_4}}{\sqrt{T_4^p}} \tag{II.17}$$

From Eqns. II.4 & II.7

$$S_{30} \, e^{-i\Phi_3} = K_{ig} \left\{ \alpha_4^p \, \Psi_{tr,4} \frac{\varepsilon_4}{2\pi} \, I_1 \, e^{-i\Phi_{R4}} \right\} \tag{II.18}$$

$$S_{20} e^{-i\Phi_2} = K_{ig} \left\{ \alpha_2^p \Psi_{Tr,4} \frac{\varepsilon_{R4}}{2\pi} \, I_1 e^{-i\Phi_{R4}} + \alpha_2^{2s} \frac{2}{\pi} I_2 + \alpha_2^{RE} \frac{\varepsilon_2}{\pi} I_1 \, e^{-i\Phi_{R2}} \right\} \tag{II.19}$$

$$S_{10} \, e^{-i\Phi_1} = K_{ig} \left\{ \alpha_1^s \, \frac{2}{\pi} \left(1 - \eta\right) \, I_1 + \alpha_1^{2RE} \, \frac{\varepsilon}{\pi} \, I_1 \, e^{-i\Phi_{R2}} + \right.$$

$$\left. + \, \alpha_1^p \, \Psi_{tr,4} \, \frac{\varepsilon_4}{2\pi} \, I_1 \, e^{-i\Phi_{R4}} \right\} \tag{II.20}$$

**Assumptions**

i) The contribution of recombined $H_2$ to H is negligible.

ii) The signal of $H_2$ due to cracking of $SiH_4$ is small.

iii) Signal added to H due to $SiH_4$ cracking is small.

From Eqns. (II.19) & (II.20);

$$S_{20} \, e^{-i\Phi_2} = K_{ig} \left\{ \alpha_2^{2s} \, \frac{2}{\pi} \, I_2 + \alpha_2^{RE} \, \frac{\varepsilon_2}{\pi} \, I_1 \, e^{-i\Phi_{R2}} \right\} \tag{II.21}$$

$$S_{10}\, e^{-i\Phi_1} = K_{ig}\left\{\alpha_1^s\, \frac{2}{\pi}\, \left(1 - \eta\right)\right\} \tag{II.22}$$

**$SiH_4$ Channel**

From Eqns. (II.18) and (II.22)

$$\frac{\varepsilon_4}{1 - \eta} = \frac{4\, \alpha_1^s\, S_{30}}{\alpha_4^p\, S_{10}} \tag{II.23}$$

$$\frac{\alpha_1^s}{\alpha_4^p} = \frac{a_{1^+}^1\, \sigma_1\, t_1\, \gamma_1\, f_p^1\, \sqrt{M_1 T_4}}{a_{3^+}\, \sigma_4\, t_3\, \gamma_3\, f_4^p\, \sqrt{M_4 T_1}} \tag{II.24}$$

where values of some of the various constants are:

$a_{1^+}^1 = 1$; $\dfrac{f_1^p}{f_4^p} \approx 1$; $T_1^s \approx T_{beam} = 2500\,K$; $T_4^p = T_s$ = target surface temperature.

$$\frac{\sigma_1\, t_1\, \gamma_1}{\sigma_4\, t_3\, \gamma_3} = 0.237 \tag{II.25}$$

$$\sigma_1 = 6.80 \times 10^{-17}\ cm^2$$

$$\sigma_2 = 9.71 \times 10^{-17}\ cm^2$$

$$\frac{\sigma_2 \gamma_2 t_2}{\sigma_4 \gamma_4 t_4} = 0.45^{(41)}$$

$$\gamma_1\,,\ \gamma_2 = 0.82\,,\ 1.02^{(42)}$$

**Cracking Pattern of $SiH_4$**

The measured cracking pattern of $SiH_4$ at 52 eV ignoring the $H_2^+$ and $H^+$ components are:

$Si^+$ = 8.8% $SiH^+$ = 13% $SiH_2^+$ = 45.5% $SiH_3^+$ = 30.5% $SiH_4^+$ = 2.2%

The measured values compares well with what has been reported by Chatham et al.[120]. Substitution of the above data into Eqs. II.24 and II.23 gives the following

relation between $\varepsilon_4$, the Si surface temperature, $\eta$ and the measured $SiH_3^+$ to $H^+$ signal ratio or $SiH_2^+$ to $H^+$ signal ratio:

$$\frac{\alpha_1^s}{\alpha_4^p} = 3.66 \times 10^{-3} \sqrt{T_s}$$

$$\frac{\varepsilon_4}{1-\eta} = 1.46 \times 10^{-2} \sqrt{T_s} \left(\frac{f_1^p}{f_4^p}\right) \left(\frac{S_{30}}{S_{10}}\right) \tag{II.26}$$

Or

$$\frac{\varepsilon_4}{1-\eta} = 9.82 \times 10^{-3} \sqrt{T_s} \left(\frac{f_1^p}{f_4^p}\right) \left(\frac{S_{20}^p}{S_{10}}\right) \tag{II.27}$$

where $S_{20}^p$ is the measured signal of $SiH_2^+$ signal. Either Eq. II.26 or II.27 is used to calculate the experimental data points plotted in section 4 and 5. Note these points represents the ratio of $\varepsilon_4$ to $1-\eta$.

**$H_2$ Channel (Recombination)**

An explicit expression for $\varepsilon_2$ is obtained using Eqs. (II.21) & (II.22)

$$\frac{\varepsilon_2}{1-\eta} = \frac{2\,\alpha_1^s\,S_{20}}{\alpha_2^{RE}\,S_{10}} - \frac{2\,\alpha_2^{2s}\,I_2}{\alpha_2^{RE}(1-\eta)\,I_1} \tag{II.28}$$

**Direct beam measurement**

The first Fourier component of a square modulated beam is:

$$F_2^d = \frac{2}{\pi} I_2 \quad \text{for } H_2 \tag{II.29}$$

$$F_1^d = \frac{2}{\pi} I_1 \quad \text{for } H \tag{II.30}$$

The relation between the mass spectrometer signals of H and $H_2$ and their fluxes at ionizer are:

$$S_1^d = K_{jg}\, \alpha_1^d\, F_1^d \tag{II.31}$$

$$S_2^d = K_{jg}\, \alpha_2^d\, F_2^d \tag{II.32}$$

where $K_{jg}$ is the geometric and instrument constant for the second mass spectrometer. Algebraic manipulation of Eqs. II.29 - II.32 yields:

$$\frac{I_2}{I_1} = \frac{\alpha_1^d\, S_2^d}{\alpha_2^d\, S_1^d} \tag{II.33}$$

Substitution of (II.33) into (II.28) gives an explicit expression for $\varepsilon_2$ as a function of experimentally measured signals, the surface temperature and $\eta$:

$$\frac{\varepsilon_2}{1-\eta} = 0.0149\sqrt{T_s}\left\{\frac{S_{2,0}}{S_{1,0}} - \frac{S_2^d}{(1-\eta)\, S_1^d}\right\} \tag{II.34}$$

This equation is used to estimate a theoretical value of $\eta$ by substitution of measured quantities and estimating a value of $\varepsilon_2$ with the requirement that; $0 \le \varepsilon_2 \le 1$.

# 11 REFERENCES


1. L. H. Rovner, and G. R. Hopkins, Nucl. Technol. 29, 274 (1976).
2. B. L. Doyle, W. R. Wampler, D. K. Brice, and S. T. Picraux, J. Nucl. Mat. 93, 551 (1980).
3. D. M. Meade, Nucl. Fusion 14, 289 (1974).
4. R. K. Gould, J. Chem. Phys. 63, 1825 (1975).
5. M. Balooch, and D. R. Olander, J. Chem. Phys. 63, 4772 (1975).
6. M. Coulon, and L. Bonnetain, J. Chem. Phys. 71, 711, 725 (1974).
7. J. N. Smith, Jr., C. H. Meyer, Jr., and J. K. Layton. J. Nucl. Mater. 67, 234 (1977).
8. B. J. Wood, and H. Wise, J. Phys. Chem. 73, 1348 (1969).
9. J. Bohdansky, J. Roth, and M. K. Sinha, Fusion Technol., Proc 9th Symp., Comm. European Commun. pg. 541, (Pergamon Press, London, 1976).
10. J. Roth, J. Bohdansky, W. Poschentieder, and M. K. Sinha, J. Nucl. Mater. 63, 222 (1976).
11. B. Feinberg, and R. S. Post, J. Vac. Sci. Technol. 13, 443 (1976).
12. N. P. Busharov, E. A. Gorbatov, V. M. Gusev, M. I. Guseva, and Yu V. Martynenko, J. Nucl. Mater. 63, 230 (1976).
13. K. Sone, H. Ohtsuka, T. Abe, R. Yamada, K. Obara, O Tsukakoshi, T. Narusawa, T. Satake, M. Mizuno, and S. Komiya, JEARI (Japan) Memo 6786 (1976).
14. R. P. H. Chang, C. C. Chang, and S. Darack, J. Vac. Sci. Technol. 20, 45 (1982).
15. S. Veprek, and V. Marecek, Solid State Electron. 11, 683 (1968)

16. A. Stock, and C. Somieski, Ber 49, 144 (1916).

17. Finholt, Bond, and Schlesinger, J. Am. Chem. Soc. 69, 1199 (1947).

18. Finholt, Bond, Wilzback, and Schlesinger, J. Am. Chem. Soc. 69. 2692 (1947).

19. S. P. Khase, and B. L. Moiseiwitsch, Proc. Phys. Soc. 88, 605 (1966)

20. C. C. Goodyear, and A. von Engel, Proc. Phys. Soc. 79, 732 (1962).

21. A. T. Bell, Ind. Eng. Fundam. 11, 209 (1972).

22. A. P. Webb, and S. Veprek, Chem. Phys. Lett. 62, 173 (1979).

23. S. Veprek, and F. A. Sarrott, Plasma Chemistry and Plasma Processing 2, 233 (1982).

24. S. N. Foner, and R. L. Hudson, J. Chem. Phys. 21, 1374 (1953).

25. 16. J. N. Smith, and W. L. Fite, J. Chem. Phys. 37, 898 (1962).

26. J. N. Smith, and W. L. Fite, "Proc. 3rd Inter. Symp. Rarefied Gas Dynamics" 1, 430 (1963).

27. C. T. Foxon, M. R. Boudry, and B. A. Joyce, Surface Sci. 44, 69 (1974).

28. J. A. Schwarz, and R. J. Madix, Surface Sci. 46, 317 (1974).

29. M. P. D'Evelyn, and R. J. Madix, Surf. Sci. Rep. 3, 413, (1984).

30. R. L. Palmer, and J. N. Smith Jr., Catal. Rev. 12, 279 (1975).

31. W. H. Weinberg, Adv. in Colloid and Interface Sci., 4, 301 (1975).

32. G. A. Somorjai, J. Colloid and Interface Sci. 58, 150 (1977).

33. S. T. Ceyer, and G. A. Somorjai, Ann. Rev. of Phys. Chem. 28, 477 (1977).

34. M. J. Cardillo, Ann. Rev. Phys. Chem., 32, 331 (1981).

35. R. H. Jones, "Kinetics of the Reaction of Pyrolytic Graphite with Molecular Oxygen", Ph.D. Thesis, LBL - 104, (1971).

36. R.H. Jones, D. R. Olander, W. J. Siekhaus, and J. A. Schwarz, J. Vac. Sci. Technol. 9, 1429 (1972).

37. H. W. Liepmann, J. Fluid Mech. 10, 65 (1961).

38. W. J. Siekhaus, R. H. Jones, and D. R. Olander, J. Appl. Phys. 41, 4392 (1970).

39. F. G. Allen, J. Appl. Phys. 28, 1510 (1957).

40. Handbook of Chemistry and Physics 63rd Ed. (1982-83) pg. E387.

41. M. K. Farnaam, "The Surface Chemistry of Epitaxial Silicon Deposition by Thermal Cracking of Silane", Ph.D. Thesis, LBL - 15448, (1983).

42. M. Asano, H. Kimura, and K Kubo, Mass Spectroscopy 27, 157 (1979).

43. M. K. Farnaam, and D. R. Olander, Surf. Sci. 145, 390 (1984).

44. R. J. Madix, and J. A. Schwartz, Surf. Sci. 24, 264 (1971).

45. J. J. Lander, Surf. Sci. 1, 125 (1964)

46. J. V. Florio, and W. D. Robertson, Surf. Sci. 22, 173 (1970).

47. P. A. Bennett, and M. W. Webb, Surf. Sci. 104, 74 (1981).

48. J. W. Coburn, and H. F. Winters, J. Appl. Phys. 50, 3189 (1979).

49. Y. Y. Tu, T. J. Chuang, and H. F. Winters, Phys. Rev. B23, 823 (1981).

50. U. Gerlach-Mayer, J. W. Coburn, and E. Kay, Surf. Sci. 103, 427 (1982).

51. R. A. Haring, A. Haring, F. W. Saris, and A. E. de Vries Appl. Phys. Lett. 41, 174 (1982).

52. E. A. Knabbe, J. W. Coburn, and E. Kay, Surf. Sci. 123, 427 (1982).

53. H. F. Winters, and F. A. Houle, J. Appl. Phys. 54, 1218 (1983).

54. M. Balooch, D. R. Olander, and W. J. Siekhaus, Mat. Res. Soc. Symp. Proc. 38, 171 (1985).

55. J. L. Benton, C. J. Doherty, S. D. Ferris, D. L. Flamm, L. C. Kimerling, and H. J. Leamy, Appl. Phys. Lett. 6, 670 (1980).

56. S. J. Pearton, and A. J. Tavendale, Phys. Rev. B26, 1105 (1982).

57. A. J. Tavendale, and S. J. Pearton, J. Phys. C16, 1665 (1983).

58. S. J. Pearton, and E. E. Haller, J. Appl. Phys. 54, 36 (1983).

59. J. I. Pankove, and M. L. Tarng, Appl. Phys. Lett. 32, 439 (1978).

60. J. I. Pankove, and M. L. Tarng, Appl. Phys. Lett. 34, 156 ( 1979).

61. T. I. Kamins, and Marcoux, IEEE Electron Device Lett. EDL-1 159 (1980).

62. N. M. Johnson, D. K. Bielgelsen, and M. D. Moyer, "Grain Boundaries in Semiconductors", Ed. by C. H. Seager, G. E. Pike and H. J. Leamy (Elsevier, N. Y. 1982).

63. A. van Wieringen, and N. Warmoltz, Physica XXII, 849 (1956).

64. D. Sherman, "Hydrogen Retention and Release from Uranium Dioxide", Ph.D. Thesis, Nucl. Engr. Dept., UC Berkeley (1987).

65. V. A. Singh, C. Weigel, J. W. Corbett, and L. M. Roth. Phys. Stat. Sol. 81B, 637 (1977).

66. S. T. Picraux, and F. L. Vook, Phys. Rev. B18, 2066 (1978).

67. J. W. Corbett, S. N. Sahu, T. S. Shi, and L. C. Snyder, Phys. Lett. 93A, 303 (1983).

68. Y. Amenomiya, and R. J. Cvetanovic, J. Phys. Chem. 67, 144 (1963).

69. J. L. Stakebake, J. Phys. Chem. 77, 581 (1973).

70. M. Iwamoto, Y. Yoda, M. Egashira, and T. Seiyama, J. Phys. Chem. 80, 1989 (1976).

71. T. Hirabayashi, M. Saeki, and E. Tachikawa, J. Nucl. Mat. 126, 38 (1984).

72. A. Mainwood, and A. M. Stoneham, J. Phys. C 17, 2513 (1984).

73. K. D. Brzoska, and Ch. Klient, Thin Solid Films, 39, 131 (1976).

74. J. T. Law, and E. E. Francois, J. Phys. Chem. 60, 353 (1956).

75. J. J. Lander, and J. Morrison, J. Appl. Phys. 34, 1403 (1963).

76. W. A. Harrison, Surf. Sci. 55, 1 (1976).

77. J. D. Lavine, S. H. McFarlane, and P. Mark, Phys. Rev. B16, 5415 (1977).

78. D. J. Miller, and D. Haneman, Surf. Sci. 104, 1237 (1981).

79. W. Monch, Surf. Sci. 86, 672 (1972).

80. D. J. Chadi, Phys. Rev. Lett. 43, 43 (1979).

81. G. Binning, H. Rohrer, Ch. Gerber, and E. Weibel, Phys. Rev. Lett. 50, 120 (1983).

82. P. A. Bennet, L. C. Feldman, Y. Kuk, E. G. McRae, and J. E. Rowe, Phys. Rev. B28, 3656 (1983).

83. R. J. Culbertson, L. C. Feldman, and P. J. Silverman, Phys. Rev. Lett. 45, 2043 (1980).

84. R. M. Tromp, E. J. van Leonen, M. Iwami, and F. W. Saris, Solid State Commun. 44, 253 (1984).

85. L. C. Snyder, Z. Wasserman, and J. W. Moskowitz, J. Vac. Sci. Technol. 16, 1266 (1979).

86. L. C. Snyder, Surf. Sci. 140, 101 (1984).

87. M. J. Cardillo, Phys. Rev. B23, 4279 (1981).

88. F. J. Himpsel, and I. P. Batra, J. Vac. Sci. Technol. A2, 952 (1984).

89. T. Yamaguchi, Phys. Rev. B30, 1992 (1984).

90. K. Takayanagi, Y. Tanishiro, S. Takahashi, and M. Takahashi, Surf. Sci. 164, 367 (1985).

91. G. Schulze, and M. Henzler, Surf. Sci. 124, 336 (1983).

92. H. Wagner, R. Butz, U. Backes, and D. Bruchmann, Solid State Comm. 38, 1155 (1981).

93. J. A. Schaefer, F. Stucki, D. J. Frankel, W. Gopel, and G. J. Lapeyre, J. Vac. Sci. Technol. B2, 359 (1984).

94. Y. J. Chabal, G. S. Higashi, and S. B. Christman, Phys. Rev. B28, 4472 (1983).

95. J. I. Pankove, M. A. Lampert, and M. L. Tarng, Appl. Phys. Lett. 32, 439 (1978).

96. S. T. Picraux, and F. L. Vook, Phys. Rev. B18, 2066 (1978).

97. C. H. Seager, and D. S. Girley, Appl. Phys. Lett. 34, 337 (1979).

98. N. M. Johnson, D. K. Biegelsen, and M. D. Moyer, Appl. Phys. Lett. 40, 882 (1982).

99. W. S. Verwoerd, Surf. Sci. 125, 575 (1983).

100. W. L. Hansen, S. J. Pearton, and E. E. Haller, Appl. Phys. Lett. 44, 606 (1984).

101. M. L. W. Thewalt, E. C. Lightowers, and J. I. Pankove, Appl. Phys. Lett. 46, 689 (1985).

102. N. M. Johnson, C. Herring, and D. J. Chadi, Phys. Rev. Lett. 56, 769 (1986).

103. X. C. Mu, S. J. Fonash, and R. Singh, Appl. Phys. Lett. 49, 67 (1986).

104. 73. C. H. Seager, R. A. Anderson, and J. K. G. Panitz, J. Mater. Res. 2, 96 (1987).

105. D. R. Olander, and A. Ullman, Inter. J. Chem. Kinetics 8, 625 (1976).

106. K. Y. Choo, P. P. Gasper, and A. P. Wolf, J. Phys. Chem. 79, 1752 (1975).

107. S. L. Bernasek, and G. A. Somorjai, J. Chem. Phys. 62, 3149 (1975).

108. R. C. Baetzold, and G. A. Somorjai, J. Catal. 45, 94 (1976).

109. N. M. Johnson, Phys. Rev. B31, 5525 (1985).

110. N. M. Johnson, Appl. Phys. Lett. 47, 874 (1986).

111. J. I. Pankove, P. J. Zanzucchi, C. W. Magee, and G Lucovsky, Appl. Phys. Lett. 46, 421 (1985).

112. S. J. Pearton, "Proceedings of the 13th Inter. Conf. on Defects in Semiconductor", Coronado, California, August 1984, edited by L. C. Kimerling and J. M. Parcey, Jr. (AIME, New York, 1985) p. 737.

113. A. E. Jaworowski, L. S. Wielunski, and T. W. Listerman, Mater. Res. Soc. Symp. Proc. 46, 561 (1985).

114. K. C. Pandey, T. Sakurai, and H. D. Hagstrum, Phys. Rev. Lett. 35, 1728 (1975).

115. S. Dushman, "Scientific Foundation of Vacuum Technique", John Wiley.

116. M. Knudsen, Ann. Physik 28, 999 (1909)

117. JANAF Thermochemical Tables

118. O. Kubaschewski, Thermochemical Properties of Inorganic Substances Springer-Verlag (1973)

119. B. B. Dayton, 1959 Vacuum Symposium Transactions, Pergamon Press, London, 1960 pg. 101.

120. H. Chatham, D. Hils, R. Robertson, and A. Gallagher, J. Chem. Phys. 81, 1770 (1984).

121. Private communication with M. Balooch.

*LAWRENCE BERKELEY LABORATORY*
*TECHNICAL INFORMATION DEPARTMENT*
*UNIVERSITY OF CALIFORNIA*
*BERKELEY, CALIFORNIA 94720*